Optimal Waveform Design for Array Imaging

Liliana Borcea[*]   George Papanicolaou[†]   Chrysoula Tsogka[‡]

September 7, 2007

Abstract

We introduce and analyze several algorithms for optimal illumination in array imaging. We consider time reversal and Kirchhoff migration imaging in homogeneous media, in regimes where the signal-to-noise ratio is high (infinite). Extensions to coherent interferometric imaging in clutter are described briefly. We show with numerical simulations that the optimal illumination algorithms image selectively closely spaced point scatterers and extended scatterers with considerably better resolution than without the optimization. We analyze the imaging algorithms in the Fraunhofer diffraction regime for small and extended scatterers. Using the prolate spheroidal wave functions we also derive analytic expressions of optimal illuminations for imaging strips.

1   Introduction

In optimal waveform design for array imaging, we look for probing pulses and illumination patterns that enhance the resolution of the image of scatterers in a medium. In this paper we assume that the medium is known and homogeneous and we study theoretically and with numerical simulations optimal waveform design for time reversal and Kirchhoff migration imaging.

Time reversal is a physical process [23, 24, 22] that consists of two steps: First, we illuminate the scatterers from the sources in the array and record over a time window the echoes that come back. Second, we time-reverse the recorded echoes and re-emit them into the medium, where they propagate back to the scatterers and focus on them. The focusing occurs because of the time reversibility of the wave equation, which holds when the waves propagate through the same medium in both steps of the time reversal process. In general, the imaging process is different than time reversal, because it back propagates fictitiously the time reversed echoes to points where the image is formed. By fictitious we mean that the back propagation is done numerically or analytically in a surrogate medium that can differ from the true one, which may not be known in detail [12, 13]. However, in this paper we consider homogeneous and known media and we refer to the resulting

---

[*]Computational and Applied Mathematics, MS 134, Rice University, 6100 Main Street, Houston, TX 77005-1892.(`borcea@caam.rice.edu`)

[†]Department of Mathematics, Stanford University, Stanford, CA 94305. (`papanico@math.stanford.edu`)

[‡]Department of Mathematics, University of Chicago, Chicago, IL 60637. (`tsogka@math.uchicago.edu`)

1

imaging function as time reversal since it is mathematically equivalent to that of physical time reversal.

In time reversal all the sources can work at once to focus energy (beamform) selectively on the scatterers. In Kirchhoff migration [5, 27] the illumination is done with one source at a time, so there is no actual beamforming. The Kirchhoff migration function is given by the superposition of the echoes recorded for each source and back propagated fictitiously to the point where we form the image. This can be interpreted mathematically as beamforming onto the imaging point, which varies over a search domain where we look for the scatterers.

The optimal waveform design for time reversal looks for array illuminations that focus selectively on various features of the scatterers. For example, for a cluster of small scatterers we wish to focus on one scatterer at a time. For imaging the support of extended scatterers we wish to focus on their edges or corners. In Kirchhoff migration the aquisition of the array response matrix is done before the imaging process. The question is then how to process the data in order to enhance the resolution of the images.

In this paper we study waveform design in a regime where the signal-to-noise ratio (SNR) is high (infinite). Low SNR can arise because of clutter in the medium and instrument noise at the receivers. Clutter is more challenging to deal with because it creates echoes with considerable delay spread (coda), which cannot be treated as additive and uncorrelated noise. The optimal illumination algorithms introduced in this paper have been extended to imaging in clutter in [11]. The key difference is that the images are formed with the statistically stable adaptive coherent interferometic (CINT) method, which was introduced in [9, 8]. A preliminary study of optimal waveform design in low SNR regimes due to instrument noise is given in [9]. A more detailed analysis of noise effects is left for future studies.

Optimal illumination is typically studied in connection with array detection of scatterers [15, 24, 22]. This is different from optimal illumination for resolution enhancement because it seeks to maximize the energy of the echoes received at the array, instead of improving the resolution of the image. The optimal illumination for detection can be obtained from the singular value decomposition (SVD) of the Fourier transform of the array response matrix. The illuminating waveform is the right singular vector corresponding to the leading singular value at its peak frequency [15, 22]. This is a narrow band illumination that has poor range resolution and cannot detect the edges of an extended scatterer. If we use successively time reversal with one singular vector at a time, over the whole frequency band, then we focus selectively on successively weaker scatterers, provided that they are small and well separated. This is the DORT (Decomposition de l'Operateur de Retournement Temporel) method of selective illumination and imaging in homogeneous media, introduced in [23, 22]. Extensions of this SVD approach to imaging well separated small scatterers in random media are given in [12, 13], using matched field functionals combined with arrival time estimation.

In this paper we show that optimal illumination can be used to enhance the resolution of images of small scatterers that are not well separated, as well as of extended scatterers. We introduce variational principles for obtaining optimal illuminations, based on minimizing the spatial support of the image. Using numerical simulations we show that for Kirchhoff migration imaging the variational algorithms tend to favor illuminations from the edges of the array, and from the higher end of the frequency band. These results are supported by the analysis, which we carry out in the Fraunhofer diffraction regime for general extended scatterers. We also analyze linearized least squares imaging and compare it with Kirchhoff migration with optimal illumination. Kirchhoff migration is an approximation of least squares imaging when the normal operator is replaced by the identity. This is a valid approximation for large arrays and large bandwidths [5, 4, 27]. For moderate size arrays and bandwidths, Kirchhoff migration imaging improves considerably when we use optimal illumination.

We also introduce in this paper variational principles for optimal illumination with selective focusing, using the SVD of the response matrix in the frequency domain. We illustrate with numerical simulations how these algorithms image selectively small scatterers that are not well separated. We complement the numerical results with an analysis in the Fraunhofer diffraction regime. We obtain analytical forms of the SVD of the response matrix and of the imaging functions, for general extended scatterers. For strip-like scatterers, the SVD has an explicit form in terms of the prolate spheroidal wave functions [26, 21, 25]. At any frequency in the bandwidth the number of non-zero singular values is approximately $\frac{b}{\lambda L/a}$, where b is the width of the strip, λ is the wavelength, L is the range, a is the aperture of the array, and $\lambda L/a$ is the time reversal spot size. This relation is expected on physical grounds, as pointed out in [29, 28, 19]. Here we derive it analytically. We also show that, at high SNR, the optimal illuminations are from the edges of the array and that the resulting images are sharply peaked at the edges of the strip. The focusing of DORT images on the edges of extended scatterers was observed numerically and experimentally in [20]. Here we derive it analytically.

This paper is organized as follows. In section 2 we formulate the array imaging problem using time reversal, Kirchhoff migration, and linearized least squares. In section 3 we first review optimal illumination for detection and selective illumination with DORT. Then, we introduce variational principles for imaging with optimal illumination. In section 4 we present numerical simulations with the optimal illumination algorithms. We begin the analysis in section 5 by introducing the Fraunhofer diffraction regime and deriving a simplified form of the SVD of the response matrix in the frequency domain. In section 6 we obtain an analytical form of the variational principles for optimal illumination associated with time reversal and Kirchhoff migration, respectively. We calculate explicitly the optimal illumination for a point scatterer. In section 7 we consider the special case of imaging strip-like objects, where the SVD has an explicit form in terms of the

prolate spheroidal wave functions. We analyze there selective imaging and show that optimal illuminations for time reversal imaging favor the edges of the array. The resulting images are sharply peaked at the edges of strips. In section 8 we use the prolate spheroidal wave functions to analyze optimal illuminations for strips with Kirchhoff migration. We show that edge illumination is favored again, in agreement with the more general results of section 6. In section 9 we analyze linearized least squares imaging of strips with prolate spheroidal wave functions and compare with Kirchhoff migration imaging. We end with a summary in section 10.

2   Array imaging

We consider time reversal and Kirchhoff migration imaging of reflectors in a medium, given time traces of the echoes received at an actively probing array. The array has N_s sources and N_r receivers distributed over a domain $\mathcal{A}$. We consider both two dimensional arrays in three dimensions (3-D) and one dimensional arrays in two dimensions (2-D). We take for simplicity $\mathcal{A}$ to be a square with side a in 3-D, and an interval of length a in 2-D. The sources and receiver locations are denoted by $\vec{\mathbf{x}}_s$ and $\vec{\mathbf{x}}_r$, for $s = 1, \dots, N_s$ and $r = 1, \dots, N_r$. We suppose for convenience that the sources and receivers are co-located and that $N_s = N_r = N$. We also assume that they are closely spaced, so that the array behaves like an aperture.

In this paper we consider only wave propagation in a homogeneous medium with wave speed c_o. This means that scattering occurs only at the reflectors that we wish to image. The reflectors are at range L from the array and they have a reflectivity function $\rho(\vec{\mathbf{y}})$. We study two array imaging methods: time reversal and Kirchhoff migration. They are described in the next section.

2.1   Time reversal imaging and migration

We denote by $\widehat{\Pi}(\omega)$ the $N \times N$ Fourier transform of the array impulse response matrix. Its entries $\widehat{\Pi}(\vec{\mathbf{x}}_r, \vec{\mathbf{x}}_s, \omega)$ are the Fourier transform of the time traces received at $\vec{\mathbf{x}}_r$, at frequency ω, when a δ function pulse is sent from $\vec{\mathbf{x}}_s$. Note that by reciprocity and due to our assumption of co-located sources and receivers, $\widehat{\Pi}(\omega)$ is complex symmetric but not Hermitian.

We typically send from the array pulses that are band limited and may vary with $\vec{\mathbf{x}}_s$. We let $[\omega_o - B/2, \omega_o + B/2]$ be our frequency band, with central frequency ω_o and bandwidth B. The echoes received at the array are given by the time convolution of the emitted pulses with the response matrix. Depending on the imaging method used, the array may illuminate the reflector sequentially, with one source at a time, or by using all the sources at once.

In time reversal [18], the sources emit simultaneously waveforms $\widehat{g}(\vec{\mathbf{x}}_s, \omega)$ and the receivers

record the echoes $P(\vec{\mathbf{x}}_r, t)$ whose Fourier transform is

$$\widehat{P}(\vec{\mathbf{x}}_r, \omega) = \sum_{s=1}^{N} \widehat{\Pi}(\vec{\mathbf{x}}_r, \vec{\mathbf{x}}_s, \omega)\widehat{g}(\vec{\mathbf{x}}_s, \omega). \tag{2.1}$$

The recordings $P(\vec{\mathbf{x}}_r, t)$ are then time reversed and re-emitted in the medium, where they propagate back to the reflector and refocus. The wave field observed at search point $\vec{\mathbf{y}}^S$ is

$$\mathcal{I}^{\mathrm{TR}}(\vec{\mathbf{y}}^S; \widehat{g}) = \int_{|\omega-\omega_o|\leq B/2} d\omega \sum_{r=1}^{N} \widehat{G}_o(\vec{\mathbf{x}}_r, \vec{\mathbf{y}}^S, \omega) \sum_{s=1}^{N} \overline{\widehat{\Pi}(\vec{\mathbf{x}}_r, \vec{\mathbf{x}}_s, \omega)\widehat{g}(\vec{\mathbf{x}}_s, \omega)}, \tag{2.2}$$

where the bar stands for complex conjugation.

While time reversal is a physical process, we can use (2.2) as an imaging function because we have a known, homogeneous medium. This allows us to compute $\mathcal{I}^{\mathrm{TR}}(\vec{\mathbf{y}}^S; \widehat{g})$ analytically, for any search point $\vec{\mathbf{y}}^S$, using the outgoing Green's function $\widehat{G}_o$ of the Helmholtz equation in the homogeneous medium. The Green's function is given by

$$\widehat{G}_o(\vec{\mathbf{x}}, \vec{\mathbf{y}}, \omega) = \frac{e^{ik|\vec{\mathbf{y}}-\vec{\mathbf{x}}|}}{4\pi|\vec{\mathbf{y}} - \vec{\mathbf{x}}|} \tag{2.3}$$

in 3-D and by

$$\widehat{G}_o(\vec{\mathbf{x}}, \vec{\mathbf{y}}, \omega) = \frac{i}{4}H_0(k|\vec{\mathbf{y}} - \vec{\mathbf{x}}|) \tag{2.4}$$

in 2-D. Here H_0 is the zero-th order Hankel function of the first kind. The phase of the Green's function is $k|\vec{\mathbf{y}} - \vec{\mathbf{x}}| = \omega\tau(\vec{\mathbf{y}}, \vec{\mathbf{x}})$, where $\tau(\vec{\mathbf{y}}, \vec{\mathbf{x}})$ is the travel time from $\vec{\mathbf{x}}$ to $\vec{\mathbf{y}}$ and $k = \omega/c_o$ is the wave number.

The Kirchhoff migration imaging functional has the form [16, 5]

$$\mathcal{I}^{\mathrm{KM}}(\vec{\mathbf{y}}^S; \widehat{f}) = \int_{|\omega-\omega_o|\leq B/2} d\omega \sum_{r=1}^{N} \overline{\widehat{G}_o(\vec{\mathbf{x}}_r, \vec{\mathbf{y}}^S, \omega)} \sum_{s=1}^{N} \widehat{\Pi}(\vec{\mathbf{x}}_r, \vec{\mathbf{x}}_s, \omega)\widehat{f}(\vec{\mathbf{x}}_s, \omega)\overline{\widehat{G}_o(\vec{\mathbf{x}}_s, \vec{\mathbf{y}}^S, \omega)}, \tag{2.5}$$

and it is related to the least squares method described in the next section. It is called Kirchhoff migration because for smoothly varying backgrounds the exact Green's function is approximated by its high frequency expression involving travel times. This approximation is not needed here because the medium is homogeneous.

The Kirchhoff migration function is similar to (2.2) but it does not correspond to any physical time reversal. The main difference between the two imaging functionals (2.5) and (2.2) is the illumination. In time reversal, the waveform $\widehat{g}(\vec{\mathbf{x}}_s, \omega)$ is sent from all the sources in the array and it carries phase information which allows beamforming to the scatterer. For example, $\widehat{g}(\vec{\mathbf{x}}_s, \omega)$ can be chosen as the leading right singular vector of the response matrix in order to focus energy on the most reflective part of the scatterer and therefore obtain strong echoes back at the array [23, 22]. In Kirchhoff migration the illumination is done with one source at a time, so there is no

real beamforming to the scatterers. However, comparing the imaging functions (2.5) and (2.2), we note that $\widehat{f}(\vec{\mathbf{x}}_s, \omega)\overline{\widehat{G}_o(\vec{\mathbf{x}}_s, \vec{\mathbf{y}}^S, \omega)}$ can be interpreted as an illumination which beamforms to the point $\vec{\mathbf{y}}^S$ where we form the image. The function $\widehat{f}(\vec{\mathbf{x}}_s, \omega)$ is the intensity of this illumination (see section 2.2) and the beam steering is done mathematically through the phases of the Green's function.

In this paper we study how $\widehat{g}(\vec{\mathbf{x}}_s, \omega)$ and $\widehat{f}(\vec{\mathbf{x}}_s, \omega)$ affect the resolution of the images produced with time reversal and Kirchhoff migration in homogeneous media, in high SNR regimes.

2.2 Linearized least squares imaging and Kirchhoff migration

In this section we relate the Kirchhoff migration imaging function (2.5) to an approximation of the linearized least squares solution of the array inverse scattering problem [27, 5]. We also explain why the $\widehat{f}(\vec{\mathbf{x}}_s, \omega)$ appearing in (2.5) should be viewed as intensities of the illumination from the sources at $\vec{\mathbf{x}}_s \in \mathcal{A}$.

Assume that the source at $\vec{\mathbf{x}}_s \in \mathcal{A}$ emits a signal $\phi(\vec{\mathbf{x}}_s, t)$ with complex valued Fourier coefficients

$$\widehat{\phi}(\vec{\mathbf{x}}_s, \omega) = \int dt\, e^{i\omega t}\phi(\vec{\mathbf{x}}_s, t), \tag{2.6}$$

supported in the frequency interval $[\omega_o - B/2, \omega_o + B/2]$. The symmetric negative frequency interval should be included for real signals $\phi(\vec{\mathbf{x}}_s, t)$, but we omit it here for simplicity. The Fourier coefficients of the echoes recorded at receiver locations $\vec{\mathbf{x}}_r \in \mathcal{A}$ are

$$\widehat{P}(\vec{\mathbf{x}}_r, \omega; \vec{\mathbf{x}}_s) = \widehat{\phi}(\vec{\mathbf{x}}_s, \omega)\widehat{\Pi}(\vec{\mathbf{x}}_r, \vec{\mathbf{x}}_s, \omega). \tag{2.7}$$

In linearized inversion we model the array response matrix with the single scattering, Born approximation [14]

$$\widehat{\Pi}(\vec{\mathbf{x}}_r, \vec{\mathbf{x}}_s, \omega) \approx k^2 \int d\vec{\mathbf{y}}\rho(\vec{\mathbf{y}})\widehat{G}_o(\vec{\mathbf{x}}_r, \vec{\mathbf{y}}, \omega)\widehat{G}_o(\vec{\mathbf{x}}_s, \vec{\mathbf{y}}, \omega). \tag{2.8}$$

The forward operator with fixed illumination ϕ is then a linear map acting on the reflectivity ρ

$$[\mathcal{M}_\phi \rho](\vec{\mathbf{x}}_r, \omega; \vec{\mathbf{x}}_s) = k^2\widehat{\phi}(\vec{\mathbf{x}}_s, \omega)\int d\vec{\mathbf{y}}\rho(\vec{\mathbf{y}})\widehat{G}_o(\vec{\mathbf{x}}_r, \vec{\mathbf{y}}, \omega)\widehat{G}_o(\vec{\mathbf{x}}_s, \vec{\mathbf{y}}, \omega), \tag{2.9}$$

and the linearized least squares formulation is: Find a reflectivity function ρ that minimizes the mean square misfit

$$\mathcal{J}(\rho) = \int_{|\omega-\omega_o|\leq B/2} d\omega \sum_{r=1}^{N}\sum_{s=1}^{N}\left|[\mathcal{M}_\phi \rho](\vec{\mathbf{x}}_r, \omega; \vec{\mathbf{x}}_s) - \widehat{P}(\vec{\mathbf{x}}_r, \omega; \vec{\mathbf{x}}_s)\right|^2. \tag{2.10}$$

The linearized least squares solution satisfies normal equations

$$[\mathcal{M}_\phi^\star \mathcal{M}_\phi \rho](\vec{\mathbf{y}}^S) = [\mathcal{M}_\phi^\star \widehat{P}](\vec{\mathbf{y}}^S), \tag{2.11}$$

where $\mathcal{M}_\phi^\star$ is the adjoint of the forward operator. Given the illumination ϕ, the adjoint operator maps the array data in the frequency domain to reflectivities. To determine the form of this adjoint

6

operator we introduce two inner products. The first one is in the space of the array data in the frequency domain and it has the form

$$\left\langle \widehat{W}, \widehat{P} \right\rangle = \int_{|\omega - \omega_o| \leq B/2} d\omega \sum_{s=1}^{N} \sum_{r=1}^{N} \widehat{W}(\vec{\mathbf{x}}_r, \omega; \vec{\mathbf{x}}_s) \overline{\widehat{P}(\vec{\mathbf{x}}_r, \omega; \vec{\mathbf{x}}_s)}, \tag{2.12}$$

for two different array data sets $\widehat{W}$ and $\widehat{P}$. The second inner product is in the space of reflectivity functions and has the form

$$(\gamma, \rho) = \int d\vec{\mathbf{y}} \, \gamma(\vec{\mathbf{y}}) \overline{\rho(\vec{\mathbf{y}})}, \tag{2.13}$$

for two arbitrary reflectivity functions γ and ρ. The adjoint operator $\mathcal{M}_\phi^\star$ is defined formally by

$$
\begin{aligned}
\left\langle \mathcal{M}_\phi \gamma, \widehat{P} \right\rangle &= \int_{|\omega - \omega_o| \leq B/2} d\omega \sum_{s=1}^{N} \sum_{r=1}^{N} k^2 \widehat{\phi}(\vec{\mathbf{x}}_s, \omega) \int d\vec{\mathbf{y}} \, \gamma(\vec{\mathbf{y}}) \widehat{G}_o(\vec{\mathbf{x}}_r, \vec{\mathbf{y}}, \omega) \widehat{G}_o(\vec{\mathbf{x}}_s, \vec{\mathbf{y}}, \omega) \overline{\widehat{P}(\vec{\mathbf{x}}_r, \omega; \vec{\mathbf{x}}_s)} \\
&= \int d\vec{\mathbf{y}} \, \gamma(\vec{\mathbf{y}}) \left[\int_{|\omega - \omega_o| \leq B/2} d\omega \sum_{s=1}^{N} \sum_{r=1}^{N} k^2 \widehat{\phi}(\vec{\mathbf{x}}_s, \omega) \widehat{G}_o(\vec{\mathbf{x}}_r, \vec{\mathbf{y}}, \omega) \widehat{G}_o(\vec{\mathbf{x}}_s, \vec{\mathbf{y}}, \omega) \overline{\widehat{P}(\vec{\mathbf{x}}_r, \omega; \vec{\mathbf{x}}_s)} \right] \\
&= \left(\gamma, \mathcal{M}_\phi^\star \widehat{P} \right),
\end{aligned}
$$

and it has the expression

$$\left[\mathcal{M}_\phi^\star \widehat{P} \right] (\vec{\mathbf{y}}^S) = \int_{|\omega - \omega_o| \leq B/2} d\omega \sum_{s=1}^{N} \sum_{r=1}^{N} k^2 \overline{\widehat{\phi}(\vec{\mathbf{x}}_s, \omega) \widehat{G}_o(\vec{\mathbf{x}}_r, \vec{\mathbf{y}}^S, \omega) \widehat{G}_o(\vec{\mathbf{x}}_s, \vec{\mathbf{y}}^S, \omega)} \widehat{P}(\vec{\mathbf{x}}_r, \omega; \vec{\mathbf{x}}_s). \tag{2.14}$$

Now recall (2.7) and note that (2.14) is the Kirchhoff migration function

$$
\begin{aligned}
\left[\mathcal{M}_\phi^\star \widehat{P} \right] (\vec{\mathbf{y}}^S) &= \int_{|\omega - \omega_o| \leq B/2} d\omega \sum_{r=1}^{N} \overline{\widehat{G}_o(\vec{\mathbf{x}}_r, \vec{\mathbf{y}}^S, \omega)} \sum_{s=1}^{N} \widehat{\Pi}(\vec{\mathbf{x}}_r, \vec{\mathbf{x}}_s, \omega) k^2 |\widehat{\phi}(\vec{\mathbf{x}}_s, \omega)|^2 \overline{\widehat{G}_o(\vec{\mathbf{x}}_s, \vec{\mathbf{y}}^S, \omega)} \\
&= \mathcal{I}^{\mathrm{KM}}(\vec{\mathbf{y}}^S; \widehat{f}),
\end{aligned} \tag{2.15}
$$

for illumination intensities

$$\widehat{f}(\vec{\mathbf{x}}_s, \omega) = k^2 |\widehat{\phi}(\vec{\mathbf{x}}_s, \omega)|^2, \quad s = 1, \ldots, N, \quad |\omega - \omega_o| \leq \frac{B}{2}. \tag{2.16}$$

The normal operator $\mathcal{M}_\phi^\star \mathcal{M}_\phi$ is studied in detail in [27]. It is explained there that even though $\mathcal{M}_\phi^\star \mathcal{M}_\phi$ may not be invertible in the usual sense, it acts as an approximate identity on the discontinuities of the reflectivity function ρ. In fact, when the aperture of the array and the bandwidth tend to infinity this becomes an exact result [4]. Thus, we can estimate the support of the reflectivity ρ with the right hand side in (2.11) or, equivalently, with $\mathcal{I}^{\mathrm{KM}}(\vec{\mathbf{y}}^S; \widehat{f})$. We return to this in section 9, where we quantify the accuracy of the estimation for strip-like reflectors and a Fraunhofer diffraction regime. We note here that since $\mathcal{I}^{\mathrm{KM}}(\vec{\mathbf{y}}^S; \widehat{f})$ comes from least squares imaging of the reflectivity, the illuminations $\widehat{f}(\vec{\mathbf{x}}_s, \omega)$ are non negative, as seen from (2.16).

3 Optimal illumination for detection and imaging

We discuss two optimization strategies for selecting the array illumination: (1) Maximize the power of the echoes received at the array, for optimal detection of the strong scatterers in the medium. (2) Seek the array illumination with an optimality criterion that measures the quality of the image that it produces. The first choice for array waveform design is well understood [24, 15, 22]. We review it briefly in section 3.2. The second approach to waveform design is the focus of this paper and it is new.

The singular value decomposition of the array response matrix $\widehat{\Pi}(\omega)$ is a very useful tool for studying array waveform design for both detection and imaging. We assume throughout the paper that we know $\widehat{\Pi}(\omega)$ over the frequency band $[\omega_o - B/2, \omega_o + B/2]$. The question is then how to process this data for enhancement of the resolution of the images?

3.1 The singular value decomposition of the response matrix

The singular value decomposition of $\widehat{\Pi}(\omega)$ at a given frequency ω is

$$\widehat{\Pi}(\omega) = \sum_{j=1}^{N} \sigma_j(\omega) \widehat{\mathbf{u}}_j(\omega) \widehat{\mathbf{v}}_j^\star(\omega), \quad |\omega - \omega_o| \leq \frac{B}{2}. \tag{3.1}$$

Here the star denotes conjugate and transpose $\widehat{\mathbf{v}}_j^\star(\omega) = \overline{\widehat{\mathbf{v}}_j^T(\omega)}$, the singular values $\sigma_j(\omega) \geq 0$ are in decreasing order and $\widehat{\mathbf{u}}_j(\omega)$ and $\widehat{\mathbf{v}}_j(\omega)$ are the orthonormal left and right singular vectors.

Because of our assumption of collocated sources and receivers, $\widehat{\Pi}(\omega)$ is a complex symmetric (not Hermitian) matrix in $\mathbb{C}^{N \times N}$. This means in theory that we can write a form of the SVD with the left singular vectors given by the complex conjugates of the right ones. However, this is true only when the correct phases are assigned to the singular vectors. When computing the SVD of $\widehat{\Pi}(\omega)$ with any public software we obtain

$$\widehat{\mathbf{u}}_j(\omega) = e^{i\varphi_j(\omega)} \overline{\widehat{\mathbf{v}}_j(\omega)}, \quad j = 1, \ldots, N, \tag{3.2}$$

with an ambiguous phase $\varphi_j(\omega)$ that may be difficult to unwrap in a consistent manner accross the bandwidth. Nevertheless, the projection matrices

$$\mathbb{P}_j(\omega) = \widehat{\mathbf{u}}_j(\omega) \widehat{\mathbf{u}}_j^\star(\omega) = \overline{\widehat{\mathbf{v}}_j(\omega)} \widehat{\mathbf{v}}_j^T(\omega) \tag{3.3}$$

have no phase ambiguities, because of the complex conjugation. This means that we can compute the projected matrix

$$\mathbb{P}_j(\omega)\widehat{\Pi}(\omega) = \sigma_j(\omega) \widehat{\mathbf{u}}_j(\omega) \widehat{\mathbf{u}}_j^T(\omega) = \sigma_j(\omega) \overline{\widehat{\mathbf{v}}_j(\omega)} \widehat{\mathbf{v}}_j^\star(\omega), \quad j = 1, \ldots, N, \tag{3.4}$$

and obtain consistent phases in the right hand side, over the bandwidth. We use this phase consistent form of the SVD of $\widehat{\Pi}(\omega)$ in our optimal waveform design algorithms.

3.2 Optimal illumination for detection

When trying to detect reflectors in a medium, we seek illuminations that create strong echoes at the array, so that in low SNR regimes we can distinguish them from the noise. The optimal illumination waveform for detection maximizes the power of the echoes received at the array

$$\mathcal{P}(\widehat{g}) = \int_{|\omega-\omega_o|\leq B/2} d\omega \sum_{r=1}^{N} \left| \sum_{s=1}^{N} \widehat{\Pi}(\vec{\mathbf{x}}_r, \vec{\mathbf{x}}_s, \omega) \widehat{g}(\vec{\mathbf{x}}_s, \omega) \right|^2, \tag{3.5}$$

subject to the normalization

$$\int_{|\omega-\omega_o|\leq B/2} d\omega \sum_{s=1}^{N} |\widehat{g}(\vec{\mathbf{x}}_s, \omega)|^2 = 1 \tag{3.6}$$

of the power emitted from the sources. We denote the maximum power by

$$\mathcal{P}_{\max} = \mathcal{P}(\widehat{g}_{\max}) = \max_{\widehat{g}} \mathcal{P}(\widehat{g}), \tag{3.7}$$

and the optimal illumination for detection by $\widehat{g}_{\max}(\vec{\mathbf{x}}_s, \omega)$. This can be found easily from the singular value decomposition of $\widehat{\Pi}(\omega)$, as explained in [24, 22, 15].

Denote by $v_1(\vec{\mathbf{x}}_s, \omega)$ the s-th component of $\widehat{\mathbf{v}}_1(\omega)$, which is the right singular vector corresponding to the largest singular value $\sigma_1(\omega)$. The illumination

$$\widehat{g}_1(\vec{\mathbf{x}}_s, \omega) = \frac{\widehat{v}_1(\vec{\mathbf{x}}_s, \omega)}{\sqrt{B}} \tag{3.8}$$

maximizes the single frequency power over $\widehat{g}$, subject to the normalization (3.6),

$$\mathcal{P}(\omega, \widehat{g}_1) = \max_{\widehat{g}} \mathcal{P}(\omega, \widehat{g}) = \frac{\sigma_1^2(\omega)}{B}, \qquad \mathcal{P}(\omega, \widehat{g}) = \sum_{r=1}^{N} \left| \sum_{s=1}^{N} \widehat{\Pi}(\vec{\mathbf{x}}_r, \vec{\mathbf{x}}_s, \omega) \widehat{g}(\vec{\mathbf{x}}_s, \omega) \right|^2. \tag{3.9}$$

The images produced with $\mathcal{I}^{\mathrm{TR}}(\vec{\mathbf{y}}^S, \widehat{g}_1)$, defined by (2.2), are peaked near the strongest reflector [23], as is seen in the numerical simulations of section 4. The received power is

$$\frac{1}{B} \int_{|\omega-\omega_o|\leq B/2} \sigma_1^2(\omega) \, d\omega \leq \mathcal{P}_{\max}. \tag{3.10}$$

The optimal illumination for detection $\widehat{g}_{\max}(\vec{\mathbf{x}}_s, \omega)$ maximizes the power by selecting the singular vectors at the resonant frequencies, where $\sigma_1(\omega)$ attains its global maximum. If we assume for simplicity that there is a unique resonant frequency $\omega_{\max} \in (\omega_o - B/2, \omega_o + B/2)$ and define

$$\widehat{g}_{\max}^{\delta}(\vec{\mathbf{x}}_s, \omega) = \begin{cases} \frac{\widehat{v}_1(\vec{\mathbf{x}}_s, \omega)}{\sqrt{\delta}}, & |\omega - \omega_{\max}| \leq \delta/2, \\ 0, & \text{otherwise,} \end{cases} \tag{3.11}$$

for a positive and small δ, then the optimal illumination for detection is obtained with $\widehat{g}_{\max}^{\delta}(\vec{\mathbf{x}}_s, \omega)$ in the limit $\delta \to 0$. This narrow-band optimal illumination for detection can be realized with iterative time reversal [24, 22]. It gives the strongest echoes but the lack of bandwidth is bad for imaging, as we see in section 4.

9

3.3 Selective imaging for well separated point reflectors (DORT)

Time reversal imaging with right singular vector illuminations has the form

$$
\begin{aligned}
\mathcal{I}^{\mathrm{TR}}(\vec{\mathbf{y}}^S; \widehat{v}_j) \ &= \int_{|\omega-\omega_o|\leq B/2} d\omega \sum_{r=1}^{N} \widehat{G}_o(\vec{\mathbf{x}}_r, \vec{\mathbf{y}}^S, \omega) \sum_{s=1}^{N} \overline{\widehat{\Pi}(\vec{\mathbf{x}}_r, \vec{\mathbf{x}}_s, \omega) \widehat{v}_j(\vec{\mathbf{x}}_s, \omega)} \\
&= \int_{|\omega-\omega_o|\leq B/2} d\omega \sum_{r=1}^{N} \widehat{G}_o(\vec{\mathbf{x}}_r, \vec{\mathbf{y}}^S, \omega) \sigma_j(\omega) \widehat{v}_j(\vec{\mathbf{x}}_r, \omega).
\end{aligned}
\tag{3.12}
$$

This is the DORT method [23] that images selectively well separated small scatterers, as we now describe.

When there are M point reflectors at well separated locations $\vec{\mathbf{y}}^{(j)}$ and with reflectivity $\rho^{(j)}$, for $j = 1, \ldots, M$, the response matrix has the form,

$$
\widehat{\Pi}(\omega) \approx k^2 \sum_{j=1}^{M} \rho^{(j)} \widehat{\mathbf{G}}_o^{(j)}(\omega) \left(\widehat{\mathbf{G}}_o^{(j)}(\omega) \right)^T,
\tag{3.13}
$$

where $\widehat{\mathbf{G}}_o^{(j)}(\omega)$ is the vector of Green's functions

$$
\widehat{\mathbf{G}}_o^{(j)}(\omega) = \left(\widehat{G}_o(\vec{\mathbf{x}}_1, \vec{\mathbf{y}}^{(j)}, \omega), \widehat{G}_o(\vec{\mathbf{x}}_2, \vec{\mathbf{y}}^{(j)}, \omega), \ldots, \widehat{G}_o(\vec{\mathbf{x}}_N, \vec{\mathbf{y}}^{(j)}, \omega) \right)^T.
\tag{3.14}
$$

The inner product

$$
\left(\widehat{\mathbf{G}}_o^{(j)}(\omega) \right)^{\star} \widehat{\mathbf{G}}_o^{(l)}(\omega) = \sum_{r=1}^{N} \overline{\widehat{G}_o(\vec{\mathbf{x}}_r, \vec{\mathbf{y}}^{(j)}, \omega)} \widehat{G}_o(\vec{\mathbf{x}}_r, \vec{\mathbf{y}}^{(l)}, \omega)
\tag{3.15}
$$

is the time reversal point spread function evaluated at $\vec{\mathbf{y}}^{(l)}$, for a source at $\vec{\mathbf{y}}^{(j)}$, at frequency ω [7]. For well separated reflectors with cross-range offsets greater than the support of the point spread function, or spot size $\lambda L/a$, the vectors $\widehat{\mathbf{G}}_o^{(j)}(\omega)$ and $\widehat{\mathbf{G}}_o^{(l)}(\omega)$ are orthogonal. If this holds for all $j, l = 1, \ldots, M$, then the point scatterers are well separated and $\widehat{\Pi}(\omega)$ has M positive singular values

$$
\sigma_j = k^2 |\rho^{(j)}| \|\widehat{\mathbf{G}}_o^{(j)}\|^2,
\tag{3.16}
$$

with right singular vectors

$$
\widehat{\mathbf{v}}_j(\omega) = \frac{\overline{\widehat{\mathbf{G}}_o^{(j)}(\omega)}}{\|\widehat{\mathbf{G}}_o^{(j)}\|}, \quad j = 1, 2 \ldots, M.
\tag{3.17}
$$

Assuming that $N > M$, the remaining $N - M$ singular values are zero.

If we define the normalized illuminations by

$$
\widehat{g}_j(\vec{\mathbf{x}}_s, \omega) = \frac{\widehat{v}_j(\vec{\mathbf{x}}_s, \omega)}{\sqrt{B}} = \frac{\overline{\widehat{G}_o(\vec{\mathbf{x}}_s, \vec{\mathbf{y}}^{(j)}, \omega)}}{\sqrt{B} \|\widehat{\mathbf{G}}_o^{(j)}\|},
\tag{3.18}
$$

then

$$
\begin{aligned}
\mathcal{I}^{\mathrm{TR}}(\vec{\mathbf{y}}^S; \widehat{g}_j) \;&=\; \int_{|\omega-\omega_o|\le B/2} d\omega \sum_{r=1}^N \widehat{G}_o(\vec{\mathbf{x}}_r,\vec{\mathbf{y}}^S,\omega) \sum_{s=1}^N \overline{\widehat{\Pi}(\vec{\mathbf{x}}_r,\vec{\mathbf{x}}_s,\omega)} \frac{\widehat{G}_o(\vec{\mathbf{x}}_s,\vec{\mathbf{y}}^{(j)},\omega)}{\sqrt{B}\,\|\widehat{\mathbf{G}}_o^{(j)}\|} \\
&=\; \frac{\|\widehat{\mathbf{G}}_o^{(j)}\|}{\sqrt{B}} \int_{|\omega-\omega_o|\le B/2} d\omega\, k^2 |\rho^{(j)}| \sum_{r=1}^N \widehat{G}_o(\vec{\mathbf{x}}_r,\vec{\mathbf{y}}^S,\omega)\overline{\widehat{G}_o(\vec{\mathbf{x}}_r,\vec{\mathbf{y}}^{(j)},\omega)}
\end{aligned}
\tag{3.19}
$$

is the DORT imaging function. We note its similarity to the Kirchhoff migration imaging function (2.5), except for one thing. In (3.19) the singular vector illumination beamforms to the scatterer at $\vec{\mathbf{y}}^{(j)}$ whereas in (2.5) the illumination beamforms to the search point $\vec{\mathbf{y}}^S$, where we also image.

The imaging functional (3.19) is the broadband time reversal point spread function for a point source at $\vec{\mathbf{y}}^{(j)}$. It is focused at $\vec{\mathbf{y}}^{(j)}$ with range resolution c_o/B and cross-range resolution $\lambda_0 a/B$ [8, 14]. We shall see next how to use the singular value decomposition in general, when we are not dealing with well separated point scatterers.

Remark: The time reversal function (3.12) with the singular vector illumination $\widehat{v}_j(\vec{\mathbf{x}}_s,\omega)$ requires that this be computed with consistent phases over the whole bandwidth. As explained in section 3.1, this is not given automatically by any public software SVD decomposition. In the simple case of well separated scatterers, where the singular values remain distinct over the frequency band, as it is assumed in DORT, the phases of the singular values can be unwraped consistently over the bandwidth, in a simple manner. However, in more complicated situations where the singular values cross each other over the frequency band, the consistent determination of the phases is a difficult problem. We use instead the projections (3.3) which are not affected by the phase ambiguity of the singular vectors.

Consider the projected response matrix

$$
\mathbb{P}_j(\omega)\widehat{\Pi}(\omega) = \sigma_j(\omega)\overline{\widehat{\mathbf{v}}_j(\omega)}\widehat{\mathbf{v}}_j^\star(\omega)
$$

and denote its $s-$th column by $\widehat{\mathbf{Q}}_j(\omega;\vec{\mathbf{x}}_s) = \sigma_j(\omega)\overline{\widehat{v}_j(\vec{\mathbf{x}}_s,\omega)}\widehat{\mathbf{v}}_j(\omega)$. Then the vector

$$
\widehat{\mathbf{V}}_j(\omega;\vec{\mathbf{x}}_s) = \frac{\overline{\widehat{\mathbf{Q}}_j(\omega;\vec{\mathbf{x}}_s)}}{\sigma_j(\omega)|\widehat{v}_j(\vec{\mathbf{x}}_s,\omega)|} = \frac{\widehat{v}_j(\vec{\mathbf{x}}_s,\omega)}{|\widehat{v}_j(\vec{\mathbf{x}}_s,\omega)|}\widehat{\mathbf{v}}_j(\omega)
$$

is almost the desired right singular vector $\widehat{\mathbf{v}}_j(\omega)$, except for the extra phase carried by $\widehat{v}_j(\vec{\mathbf{x}}_s,\omega)$. This is similar to what we get in echo-mode iterative time reversal, when $\widehat{\mathbf{v}}_j(\omega)$ corresponds to the strongest scatterer and when we illuminate at the first step from a single source at $\vec{\mathbf{x}}_s$.

The time reversal function with illumination $\widehat{\mathbf{V}}_j(\omega;\vec{\mathbf{x}}_s)$ is

$$
\begin{aligned}
\tilde{\mathcal{I}}^{TR}\left(\vec{\mathbf{y}}^S; \widehat{\mathbf{V}}_j(\cdot;\vec{\mathbf{x}}_s)\right) &= \int_{|\omega-\omega_o|\le B/2} d\omega\, e^{-i\omega\tau(\vec{\mathbf{x}}_s,\vec{\mathbf{y}}^S)} \sum_{r=1}^N G_o(\vec{\mathbf{x}}_r,\vec{\mathbf{y}}^S,\omega)\overline{\left[\widehat{\Pi}(\omega)\widehat{\mathbf{V}}_j(\omega;\vec{\mathbf{x}}_s)\right]}(\vec{\mathbf{x}}_r) \\
&\sim \int_{|\omega-\omega_o|\le B/2} d\omega\,\sigma_j(\omega)\overline{\left[\widehat{v}_j(\vec{\mathbf{x}}_s,\omega)\widehat{G}_o(\vec{\mathbf{x}}_s,\vec{\mathbf{y}}^S,\omega)\right]} \sum_{r=1}^N \left[\widehat{v}_j(\vec{\mathbf{x}}_r,\omega)\widehat{G}_o(\vec{\mathbf{x}}_r,\vec{\mathbf{y}}^S,\omega)\right], \quad (3.20)
\end{aligned}
$$

where we compensate[1] the extra phase in $\widehat{\mathbf{V}}_j(\omega; \vec{\mathbf{x}}_s)$ with the travel time $\tau(\vec{\mathbf{x}}_s, \vec{\mathbf{y}}^S)$. This amounts to observing at time $\tau(\vec{\mathbf{x}}_s, \vec{\mathbf{y}}^S)$ the time reversed and backpropagated field to $\vec{\mathbf{y}}^S$. The symbol $\sim$ in (3.20) stands for approximate, up to a multiplicative constant.

Note that if we superposed the images $\tilde{\mathcal{I}}^{TR}\left(\vec{\mathbf{y}}^S; \widehat{\mathbf{V}}_j(\cdot; \vec{\mathbf{x}}_s)\right)$ over all the sources in the array, we would obtain

$$
\sum_{s=1}^{N} \tilde{\mathcal{I}}^{TR}\left(\vec{\mathbf{y}}^S; \widehat{\mathbf{V}}_j(\cdot; \vec{\mathbf{x}}_s)\right) \quad \sim \quad \int_{|\omega - \omega_o| \leq B/2} d\omega \sigma_j(\omega) \left| \sum_{r=1}^{N} \left[\widehat{v}_j(\vec{\mathbf{x}}_r, \omega) \widehat{G}_o(\vec{\mathbf{x}}_r, \vec{\mathbf{y}}^S, \omega) \right] \right|^2
$$

$$
= \quad \int_{|\omega - \omega_o| \leq B/2} d\omega \sum_{s=1}^{N} \sum_{r=1}^{N} \overline{\left[\mathbb{P}_j(\omega) \widehat{\Pi} \right](\vec{\mathbf{x}}_s, \vec{\mathbf{x}}_r, \omega)} \widehat{G}_o(\vec{\mathbf{x}}_s, \vec{\mathbf{y}}^S, \omega) \widehat{G}_o(\vec{\mathbf{x}}_r, \vec{\mathbf{y}}^S, \omega).
$$

This is like the Kirchhoff migration imaging function (2.5), with $\widehat{\Pi}(\omega)$ replaced by the projected matrix $\mathbb{P}_j(\omega) \widehat{\Pi}(\omega)$.

3.4 Optimal illumination and selective imaging of clusters of small scatterers

When the M scatterers are clustered together, we do not have a one-to-one correspondence between a singular value and a single scatterer uniformly in the bandwidth, and DORT fails to image selectively. We introduce here a new algorithm for optimal illumination and selective imaging of clusters of small scatterers. The case of extended scatterers is studied theoretically in the second half of this paper. Numerical results for such scatterers will be presented in a future paper.

There are two key steps in our algorithm: First, the selective imaging is achieved with an optimal filtering of the data, as explained in section 3.4.1. The second step is described in section 3.4.2 and it seeks optimal source weights and pulses in order to improve the selective image of each scatterer. The algorithm is based on variational principles that minimize the spatial support of the image, as it is being formed with the filtered data and the source illumination. The algorithm is flexible with respect to the imaging function. Because we consider here imaging in homogeneous media, we form the image with Kirchhoff migration. In clutter, this can be replaced by the coherent interferometric imaging function [8, 9], as we explain briefly in section 3.5.

3.4.1 Selective imaging

Assuming that we have a large number N of array elements, we can write

$$
\sigma_j(\omega) \approx 0 \quad \text{for } n^{\star}(\omega) < j \leq N. \tag{3.21}
$$

Here $n^{\star}(\omega)$ is the rank of the array response matrix $\widehat{\Pi}(\omega)$ and it varies in general with the frequency, especially in the case of extended scatterers (see section 7). However, for clusters of small $M < N$

---

[1]Such phase compensation does not work in clutter, where it is difficult to get good refocusing with time reversal in echo mode. It is the time reversal in direct mode (i.e., with the illumination coming from the point that we wish to refocus in the medium) that is stable and has super-resolution of focusing in clutter [18, 6].

scatterers, we can set

$$n^\star(\omega) \approx n^\star(\omega_o) \approx M. \tag{3.22}$$

• **Data filtering:** Using the threshold $n^\star(\omega_o)$, we now define a set of filtering operators that we wish to apply to the measured array response matrix $\widehat{\Pi}(\omega)$.

Definition 1 *Let Δ be the set of non-negative subspace weights*

$$\Delta = \left\{ \widehat{d}_j(\omega) \geq 0, \quad j = 1, \ldots, n^\star(\omega_o), \quad |\omega - \omega_o| \leq \frac{B}{2}; \quad \sum_{j=1}^{n^\star(\omega_o)} \int_{|\omega - \omega_o| \leq \frac{B}{2}} \widehat{d}_j(\omega) \, d\omega = 1 \right\}.$$

We define the filtering operators $D(\omega, \cdot) : \Delta \to \mathbb{C}^{N \times N}$ which take coefficients $\widehat{d} \in \Delta$ and return a linear combination of the projection matrices (3.3)

$$D(\omega, \widehat{d}) = \sum_{j=1}^{n^\star(\omega_o)} \widehat{d}_j(\omega) \mathbb{P}_j(\omega), \tag{3.23}$$

for each frequency ω in the bandwidth.

When we apply the filters $D(\omega, \cdot)$ to the response matrix, we get according to (3.4)

$$D(\omega, \widehat{d})\widehat{\Pi}(\omega) = \sum_{j=1}^{n^\star(\omega_o)} \widehat{d}_j(\omega) \mathbb{P}_j(\omega)\widehat{\Pi}(\omega) = \sum_{j=1}^{n^\star(\omega_o)} \widehat{d}_j(\omega) \sigma_j(\omega) \widehat{\mathbf{u}}_j(\omega) \widehat{\mathbf{u}}_j^T(\omega). \tag{3.24}$$

The question is how to choose the filter coefficients? We distinguish two trivial cases:

(1) For uniform weights in the bandwidth

$$\widehat{d}_j(\omega) = \frac{1}{Bn^\star(\omega_o)}, \quad j = 1, \ldots, n^\star(\omega_o), \quad |\omega - \omega_o| \leq \frac{B}{2}, \tag{3.25}$$

$D(\omega, \widehat{d})$ is basically the identity operator, up to a scaling factor

$$D(\omega, \widehat{d})\widehat{\Pi}(\omega) = \frac{1}{Bn^\star(\omega_o)} \sum_{j=1}^{n^\star(\omega_o)} \sigma_j(\omega) \widehat{\mathbf{u}}_j(\omega) \widehat{\mathbf{u}}_j^T(\omega) \approx \frac{1}{Bn^\star(\omega_o)} \widehat{\Pi}(\omega), \tag{3.26}$$

(2) The operators $D(\omega, \cdot) : \Delta_p \to \mathbb{C}^{N \times N}$ defined on the subsets Δ_p of Δ,

$$\Delta_p = \left\{ \widehat{d} \in \Delta; \quad \widehat{d}_j(\omega) = 0 \text{ for } j \neq p, \quad j = 1, \ldots, n^\star(\omega_o), \quad \widehat{d}_p(\omega) = \frac{1}{B}, \quad |\omega - \omega_o| \leq \frac{B}{2} \right\},$$

for $p = 1, \ldots, n^\star(\omega_o)$, filter out the contribution of all singular vectors, except the p−th one, uniformly across the bandwidth. The imaging function given by such filtered data is

$$\mathcal{I}_p^{\text{DORT}}(\vec{\mathbf{y}}^S) = \int_{|\omega - \omega_o| \leq \frac{B}{2}} d\omega \, \sigma_p(\omega) \sum_{s=1}^{N} \sum_{r=1}^{N} \widehat{u}_p(\vec{\mathbf{x}}_s, \omega) \widehat{u}_p(\vec{\mathbf{x}}_r, \omega) \overline{\widehat{G}_o(\vec{\mathbf{x}}_s, \vec{\mathbf{y}}^S, \omega)} \widehat{G}_o(\vec{\mathbf{x}}_r, \vec{\mathbf{y}}^S, \omega). \tag{3.27}$$

We call it the DORT image because it uses one singular vector at a time.

In our selective imaging approach we calculate the filter coefficients $\widehat{d} = \left\{\widehat{d}_j(\omega)\right\}$ using an optimization algorithm that minimizes the spatial support of the image that we form with the filtered data

$$\mathcal{I}(\vec{\mathbf{y}}^S; \widehat{d}) = \int_{|\omega-\omega_o|\leq\frac{B}{2}} d\omega \sum_{s=1}^{N}\sum_{r=1}^{N}\left[D(\omega,\widehat{d})\widehat{\Pi}\right](\vec{\mathbf{x}}_r,\vec{\mathbf{x}}_s,\omega)\overline{\widehat{G}_o(\vec{\mathbf{x}}_s,\vec{\mathbf{y}}^S,\omega)}\widehat{G}_o(\vec{\mathbf{x}}_r,\vec{\mathbf{y}}^S,\omega). \tag{3.28}$$

The optimization is done over the set Δ or subsets of Δ, as we explain next.

• **Step 1 of the selective imaging algorithm:** We begin by finding the optimal filter $D(\omega,\cdot)$ of the data which minimizes over the weights $\widehat{d} = \left\{\widehat{d}_j(\omega)\right\}$ in Δ the objective function

$$\mathcal{O}(\widehat{d}) = \left\|\mathcal{J}(\cdot;\widehat{d})\right\|_{L^2(\mathcal{D})}^2, \quad \mathcal{J}(\vec{\mathbf{y}}^S;\widehat{d}) = \frac{\mathcal{I}(\vec{\mathbf{y}}^S;\widehat{d})}{\max_{\vec{\mathbf{y}}\in\mathcal{D}}|\mathcal{I}(\vec{\mathbf{y}};\widehat{d})|}. \tag{3.29}$$

Here $\mathcal{D}$ is the image domain that contains the cluster of scatterers. The optimization is intended to minimize the spatial support of $\mathcal{I}(\vec{\mathbf{y}}^S;\widehat{d})$ in $\mathcal{D}$, in order to focus the image on a single scatterer in the cluster. We denote the optimal filter weights by

$$\widehat{d}^{(1)} = \left\{\widehat{d}_j^{(1)}(\omega)\right\}, \quad 1\leq j\leq n^\star(\omega_o), \quad |\omega-\omega_o|\leq\frac{B}{2}. \tag{3.30}$$

• **Masking the identified scatterer:** In order to image the remaining scatterers in the cluster, we mask the one that we have identified, as follows. Denote by $J(\omega,1)$ the index of the largest subspace weight at frequency ω,

$$\widehat{d}_{J(\omega,1)}^{(1)} = \max_{1\leq j\leq n^\star(\omega_o)}\widehat{d}_j^{(1)}(\omega), \quad |\omega-\omega_o|\leq\frac{B}{2}. \tag{3.31}$$

We define the map $\delta^{(1)} : \left[\omega_o-\frac{B}{2},\omega_o+\frac{B}{2}\right]\to\mathbb{N}$ which takes a frequency ω in the bandwidth and returns

$$\delta^{(1)}(\omega) = \begin{cases} J(\omega,1) & \text{if } \widehat{d}_{J(\omega,1)}^{(1)}(\omega) > 0, \\ 0 & \text{otherwise.} \end{cases} \tag{3.32}$$

We mask the scatterer found at step 1 by seeking filters $D(\omega,\cdot) : \Delta^{(1)}\to C^{N\times N}$, where $\Delta^{(1)}$ is the subset of Δ given by

$$\Delta^{(1)} = \left\{\widehat{d}_j(\omega)\in\Delta, \ \ \widehat{d}_j(\omega)=0 \ \text{if } j=\delta^{(1)}(\omega) \text{ for } |\omega-\omega_o|\leq\frac{B}{2}, \ \ j=1,\ldots,n^\star(\omega_o)\right\}.$$

• **The iterative selective imaging algorithm:** At step $p>1$ of the selective imaging algorithm, we compute the optimal filter $D(\omega,\widehat{d}^{(p)})$ by minimizing the objective function (3.29) over the subset $\Delta^{(p)}$ of Δ given by

$$\Delta^{(p)} = \left\{\widehat{d}_j(\omega)\in\Delta^{(p-1)}, \ \ \widehat{d}_j(\omega)=0 \ \text{if } j=\delta^{(p)}(\omega) \text{ for } |\omega-\omega_o|\leq\frac{B}{2}, \ \ j=1,\ldots,n^\star(\omega_o)\right\}.$$

14

Here we use the masking maps $\delta^{(p)} : \left[\omega_o - \frac{B}{2}, \omega_o + \frac{B}{2}\right] \to \mathbb{N}$ defined for $p > 1$ by

$$\delta^{(p)}(\omega) = \begin{cases} J(\omega, p) & \text{if } \widehat{d}_{J(\omega,p)}^{(p)}(\omega) > 0, \\ 0 & \text{otherwise,} \end{cases} \qquad \widehat{d}_{J(\omega,p)}^{(p)} = \max_{1 \leq j \leq n^\star(\omega_o)} \widehat{d}_j^{(p-1)}(\omega). \tag{3.33}$$

We also set $\Delta^{(0)} \equiv \Delta$ and note that the selective imaging algorithm is an iterative optimization over the nested sets

$$\Delta^{(n^\star(\omega_o)-1)} \subset \ldots \subset \Delta^{(p)} \subset \Delta^{(p-1)} \subset \ldots \subset \Delta.$$

This iteration terminates at the $n^\star(\omega_o)$ step, when we have used all the degrees of freedom.

We illustrate how the algorithm works with numerical simulations in section 4.

3.4.2 Optimal illumination

The images obtained with the selective imaging algorithm introduced in section 3.4.1 can be improved further by assigning optimal intensities to each source in the array, as we now describe.

Let $\mathcal{F}$ be the set of source intensities in the bandwidth

$$\mathcal{F} = \left\{ \widehat{f}(\vec{\mathbf{x}}_s, \omega) \geq 0, \quad \sum_{s=1}^N \int_{|\omega - \omega_o| \leq \frac{B}{2}} d\omega \widehat{f}(\vec{\mathbf{x}}_s, \omega) = 1 \right\}$$

and define for any $\widehat{d} \in \Delta$ and $\widehat{f} = \left\{ \widehat{f}(\vec{\mathbf{x}}_s, \omega) \right\}$ in $\mathcal{F}$ the imaging function

$$\mathcal{I}_{\mathcal{F}}(\vec{\mathbf{y}}^S; \widehat{d}, \widehat{f}) = \int_{|\omega - \omega_o| \leq \frac{B}{2}} d\omega \sum_{s=1}^N \widehat{f}(\vec{\mathbf{x}}_s, \omega) \sum_{r=1}^N \left[D(\omega, \widehat{d}) \widehat{\Pi} \right](\vec{\mathbf{x}}_r, \vec{\mathbf{x}}_s, \omega) \overline{\widehat{G}_o(\vec{\mathbf{x}}_s, \vec{\mathbf{y}}^S, \omega) \widehat{G}_o(\vec{\mathbf{x}}_r, \vec{\mathbf{y}}^S, \omega)}. \tag{3.34}$$

For a given data filter $D(\omega, \widehat{d})$ with $|\omega - \omega_o| \leq B/2$, the optimal illumination $\widehat{f}$ is the minimizer over the set $\mathcal{F}$ of the objective function

$$\mathcal{O}_{\mathcal{F}}(\widehat{f}) = \left\| \mathcal{J}_{\mathcal{F}}(\cdot; \widehat{f}) \right\|_{L^2(\mathcal{D})}^2, \quad \mathcal{J}_{\mathcal{F}}(\vec{\mathbf{y}}^S; \widehat{f}) = \frac{\mathcal{I}_{\mathcal{F}}(\vec{\mathbf{y}}^S; \widehat{d}, \widehat{f})}{\max_{\vec{\mathbf{y}} \in \mathcal{D}} |\mathcal{I}_{\mathcal{F}}(\vec{\mathbf{y}}; \widehat{d}, \widehat{f})|}, \tag{3.35}$$

This can be done in conjunction with the optimal selective illumination algorithm as follows.

• **The optimal illumination algorithm:** For $p = 1, \ldots, n^\star(\omega_o)$ determine the optimal filters $D(\omega, \widehat{d}^{(p)})$ for $|\omega - \omega_o| \leq B/2$ as described in section 3.4.1. Then compute for any given p the optimal illumination $\widehat{f}^{(p)}$, which minimizes over the set $\mathcal{F}$ the objective function (3.35) computed with $\widehat{d} = \widehat{d}^{(p)}$.

This would be very expensive to do in practice, but the problem can be relaxed to a suboptimal one, with separable illuminations

$$\widehat{f}(\vec{\mathbf{x}}_s, \omega) = w_s \widehat{\varphi}(\omega),$$

where

$$w_s \geq 0, \quad \sum_{s=1}^{N} w_s = 1, \quad \widehat{\varphi}(\omega) \geq 0, \quad \int_{|\omega - \omega_o| \leq B/2} \widehat{\varphi}(\omega) d\omega = 1.$$

We show in section 4 numerical results obtained with such separable illuminations.

Remark: The selective imaging and optimal illumination algorithms can be used together, as we described here, or separately. For example, if we were to skip the selective imaging part, we would work with the unfiltered data and obtain from (3.34) the Kirchhoff migration image

$$\mathcal{I}^{\mathrm{KM}}(\vec{\mathbf{y}}^S; \widehat{f}) = \int_{|\omega - \omega_o| \leq \frac{B}{2}} d\omega \sum_{s=1}^{N} \widehat{f}(\vec{\mathbf{x}}_s, \omega) \sum_{r=1}^{N} \widehat{\Pi}(\vec{\mathbf{x}}_r, \vec{\mathbf{x}}_s, \omega) \overline{\widehat{G}_o(\vec{\mathbf{x}}_s, \vec{\mathbf{y}}^S, \omega) \widehat{G}_o(\vec{\mathbf{x}}_r, \vec{\mathbf{y}}^S, \omega)}, \qquad (3.36)$$

for weights $\widehat{f} \in \mathcal{F}$ to be determined by the minimization of the spatial support of $\mathcal{I}^{\mathrm{KM}}(\vec{\mathbf{y}}^S; \widehat{f})$.

3.5 Extensions to coherent interferometric imaging in clutter

While in this paper we consider imaging in high SNR regimes in known and homogeneous media, we have extended the selective imaging algorithm described in section 3.4 to low SNR regimes due to clutter in [11]. Imaging in such regimes is difficult, because the time traces of the echoes recorded at the array have significant delay spread (coda) due to wave scattering in clutter. This makes the Kirchhoff migration images speckled and difficult to interpret [12, 8]. They are also statistically unstable, in the sense that they change unpredictably with the realization of the clutter. We showed in [8, 9] that the imaging process can be stabilized if we remove the delay spread by computing cross-correlations of the echoes over appropriately chosen space-time windows. These cross-correlations are called coherent interferograms and their fictitious backpropagation in the smooth part of the medium (without the clutter) produces the coherent interferometric (CINT) imaging function [8, 9].

In CINT imaging there are two clutter dependent parameters that affect the quality of the image, in addition to the array illumination and data filtering that we study in this paper. They are the decoherence frequency Ω_d and the uncertainty in the direction of arrival κ_d. The latter determines the decoherence length at frequency ω as $X_d(\omega) = \frac{c_o}{\omega \kappa_d}$ [9, 10]. The decoherence frequency measures the frequency separation over which the Fourier coefficients of the measured echoes become statistically uncorrelated. In CINT we compute cross-correlations of the echoes over time windows of length $\sim \Omega_d^{-1}$, to obtain a significant delay spread reduction and emphasis of the coherent arrivals [9, 8]. This happens if we take receivers that are not more than X_d apart. It is only for such spatial separations that the echoes are statistically correlated.

The CINT imaging function is

$$\mathcal{I}^{\mathrm{CINT}}(\vec{\mathbf{y}}^S; \Omega_d, X_d, \widehat{f}, \widehat{d}) = \int_{|\omega - \omega_o| \leq B/2} d\omega \int_{\substack{|\omega' - \omega_o| \leq B/2 \\ |\omega - \omega'| \leq \Omega_d}} d\omega' \sum_{r=1}^{N} \sum_{\substack{r' = 1 \\ |\vec{\mathbf{x}}_r - \vec{\mathbf{x}}_{r'}| \leq X_d\left(\frac{\omega + \omega'}{2}\right)}}^{N}$$

$$\sum_{\substack{s=1 \\ |\vec{\mathbf{x}}_s - \vec{\mathbf{x}}_{s'}| \leq X_d\left(\frac{\omega + \omega'}{2}\right)}}^{N} \sum_{s'=1}^{N} \widehat{f}(\vec{\mathbf{x}}_s, \omega) \widehat{f}(\vec{\mathbf{x}}_{s'}, \omega') \widehat{Q}(\vec{\mathbf{x}}_r, \vec{\mathbf{x}}_s, \omega; \vec{\mathbf{y}}^S; \widehat{d}) \overline{\widehat{Q}(\vec{\mathbf{x}}_{r'}, \vec{\mathbf{x}}_{s'}, \omega'; \vec{\mathbf{y}}^S; \widehat{d})}, \qquad (3.37)$$

where $\widehat{Q}(\vec{\mathbf{x}}_r, \vec{\mathbf{x}}_s, \omega; \vec{\mathbf{y}}^S; \widehat{d})$ is the filtered data backpropagated fictitiously to the image point $\vec{\mathbf{y}}^S$

$$\widehat{Q}(\vec{\mathbf{x}}_r, \vec{\mathbf{x}}_s, \omega; \vec{\mathbf{y}}^S; \widehat{d}) = \left[D(\omega, \widehat{d}) \widehat{\Pi} \right] (\vec{\mathbf{x}}_r, \vec{\mathbf{x}}_s, \omega) \overline{\widehat{G}_o(\vec{\mathbf{x}}_s, \vec{\mathbf{y}}^S, \omega)} \widehat{G}_o(\vec{\mathbf{x}}_r, \vec{\mathbf{y}}^S, \omega). \qquad (3.38)$$

Note that in weak clutter there may be no loss of coherence, in which case we can replace Ω_d by B and X_d by the array aperture a. Then we get

$$\mathcal{I}^{\mathrm{CINT}}(\vec{\mathbf{y}}^S; B, a, \widehat{f}, \widehat{d}) = \left| \mathcal{I}_{\mathcal{F}}(\vec{\mathbf{y}}^S; \widehat{d}, \widehat{f}) \right|^2. \qquad (3.39)$$

When $\Omega_d < B$ and $X_d < a$, we use the thresholding of the frequency and spatial separation in the CINT function (3.37) to smooth statistically the image [10]. This smoothing is necessary to achieve statistical stability with respect to the realization of the clutter but it comes at the cost of loss of resolution, by blur [9].

The selective imaging algorithm described in section 3.4 has been extended in [11] to imaging in clutter, as follows: First, the imaging is done with the CINT imaging function $\mathcal{I}^{\mathrm{CINT}}(\vec{\mathbf{y}}^S; \Omega_d, X_d, \widehat{f}, \widehat{d})$ instead of $\mathcal{I}_{\mathcal{F}}(\vec{\mathbf{y}}^S; \widehat{d}, \widehat{f})$. The thresholding parameters Ω_d and X_d are estimated before the selective imaging process, with the adaptive estimation algorithm introduced in [9]. The selective imaging is then done with an iterative procedure, as in section 3.4, where at each step we minimize the support of the image, as measured by the objective function

$$\left\| \frac{\mathcal{I}^{\mathrm{CINT}}(\cdot; \Omega_d, X_d, \widehat{f}, \widehat{d})}{\max_{\vec{\mathbf{y}} \in \mathcal{D}} \mathcal{I}^{\mathrm{CINT}}(\vec{\mathbf{y}}; \Omega_d, X_d, \widehat{f}, \widehat{d})} \right\|_{L^1(\mathcal{D})}. \qquad (3.40)$$

We take the L^1 norm instead of L^2, because it is a better sparsity measure (i.e., gives tighter images) and because the CINT function is related to the square of the image $\mathcal{I}_{\mathcal{F}}$ (recall (3.39)).

4   Numerical results

In this section we present several numerical results that illustrate how the selective imaging and optimal illumination algorithms described in section 3 perform.

We use two sets of numerically simulated array data. The first set is for array imaging of a point scatterer in a homogeneous background. This is the simplest array imaging problem that can be considered. It allows us to test our algorithms and to visualize the results obtained in the analysis. The second set of array data is for four small, not well separated scatterers. The data is obtained by solving numerically the 2D acoustic wave equation, with the finite element method described in [1, 2].

4.1   Numerical simulations for a point scatterer
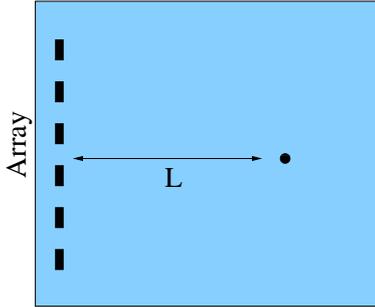
Figure 1: The one point scatterer configuration. The array is composed by 100 elements at distance $\lambda_o/2$ apart, at a range $L = 90\lambda_o$ from the scatterer.

We begin with the case of a single point scatterer, as in Figure 1. The array consists of $N = 100$ elements, at distance $\lambda_o/2$ apart, where λ_o is the central wavelength for the frequency band $1.5 - 4.5$ MHz. The bandwidth is $B = 3$MHz and the speed of propagation is $c_o = 1.5$ km/s. The range of the scatterer is $L = 90\lambda_o$. The response matrix in this case is

$$\widehat{\Pi}(\vec{\mathbf{x}}_r, \vec{\mathbf{x}}_s, \omega) = k^2 \widehat{G}_o(\vec{\mathbf{x}}_r, \vec{\mathbf{y}}^*, \omega) \widehat{G}_o(\vec{\mathbf{x}}_s, \vec{\mathbf{y}}^*, \omega),$$

where $\vec{\mathbf{y}}^*$ is the scatterer location.

4.1.1   Optimal illumination for detection

We consider first optimal illumination for detection and show the results obtained with the methods discussed in section 3.2. In Figure 2-(a) we show the Kirchhoff migration image obtained with the illumination $\widehat{g}^\delta_{\max}(\vec{\mathbf{x}}_s, \omega)$ defined by (3.11). Because in this example we have one scatterer with frequency independent reflectivity, there is only one nonzero singular value $\sigma_1(\omega)$, which attains its maximum at the largest frequency in the bandwidth. The width δ in (3.11) is at first $B/100 = 0.03$MHz. Then, we take a larger $\delta = B/10 = 0.3$MHz and compare the results in Figure 2-(a) and (b). In Figure 2-(c) we use the illumination (see (3.8))

$$\widehat{g}^{DORT}(\vec{\mathbf{x}}_s, \omega) = \frac{\widehat{v}_1(\vec{\mathbf{x}}_s, \omega)}{\sqrt{B}}.$$

18
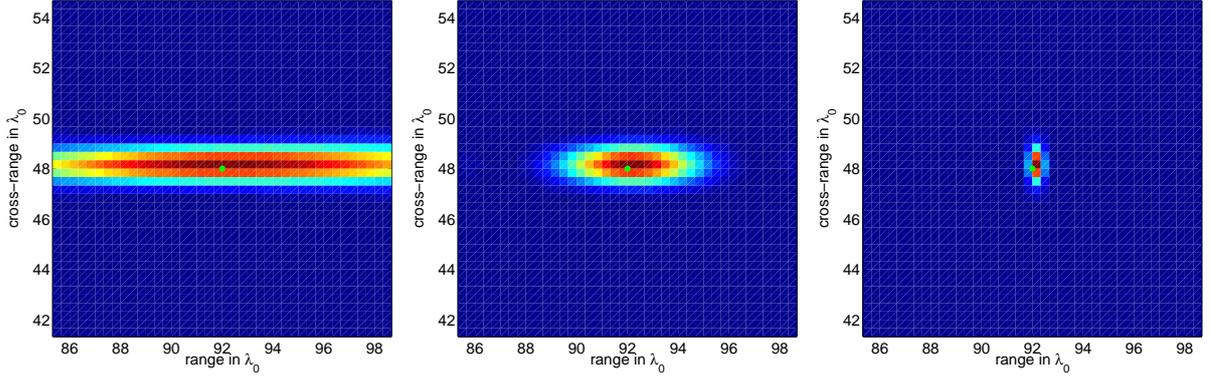
(a) $\widehat{g}_{\max}^{\delta}$ illumination, $\delta = 0.03$MHz. (b) $\widehat{g}_{\max}^{\delta}$ illumination, $\delta = 0.3$MHz.   (c) $\widehat{g}^{\mathrm{DORT}}$ illumination.

Figure 2: The one scatterer configuration. Optimal illumination for detection results. The scatterer is indicated with a green dot.

All the images are displayed in a square of 41×41 pixels, with pixel size $\lambda_0/3 \times \lambda_0/3$.

As expected, the power $\mathcal{P}(\widehat{g})$ received at the array is bigger for small δ and it decreases as δ increases. However, the quality of the image is better as δ increases because more bandwidth leads to better resolution. We show in Table 1 the values of the received power given by (3.5), for all the illuminations considered in this section.

Illumination	Power received $\mathcal{P}$	L^2 norm of the image
$g_{\max}^{\delta}$, $\delta = 0.03$MHz	5.1440e-09	3.7367
$g_{\max}^{\delta}$, $\delta = 0.3$MHz	4.9098e-10	1.4515
$\widehat{g}^{\mathrm{DORT}}$	3.8884e-11	0.1813
KM - optimal	2.3663e-11	0.1344

Table 1: The received power on the array and the L_2 norm of the image (normalized by its maximum) for the one scatterer configuration

4.1.2 Optimal illumination for Kirchhoff migration imaging

We consider the variational problem for optimal illumination in Kirchhoff migration imaging (3.36), where we minimize the objective function

$$\mathcal{O}^{\mathrm{KM}}(\widehat{f}) = \|\mathcal{J}^{\mathrm{KM}}(\cdot; \widehat{f})\|_{L^2(\mathcal{D})}^2, \quad \mathcal{J}^{\mathrm{KM}}(\vec{\mathbf{y}}^S; \widehat{f}) = \frac{\mathcal{I}^{\mathrm{KM}}(\vec{\mathbf{y}}^S; \widehat{f})}{\max_{\vec{\mathbf{y}} \in \mathcal{D}} \left| \mathcal{I}^{\mathrm{KM}}(\vec{\mathbf{y}}; \widehat{f}) \right|}, \tag{4.1}$$

over the set of separable illuminations defined by

$$\left\{ \widehat{f}(\vec{\mathbf{x}}_s, \omega) = \widehat{\varphi}(\omega) w_s, \quad \widehat{\phi}(\omega) \geq 0, \int d\omega \, \widehat{\varphi}(\omega) = 1, \quad w_s \geq 0, \sum_{s=1}^{N} w_s = 1 \right\}. \tag{4.2}$$

19

(a) Optimal weights w_s (b) Optimal pulse $\omega\widehat{\varphi}(\omega)$ (c) Optimal image
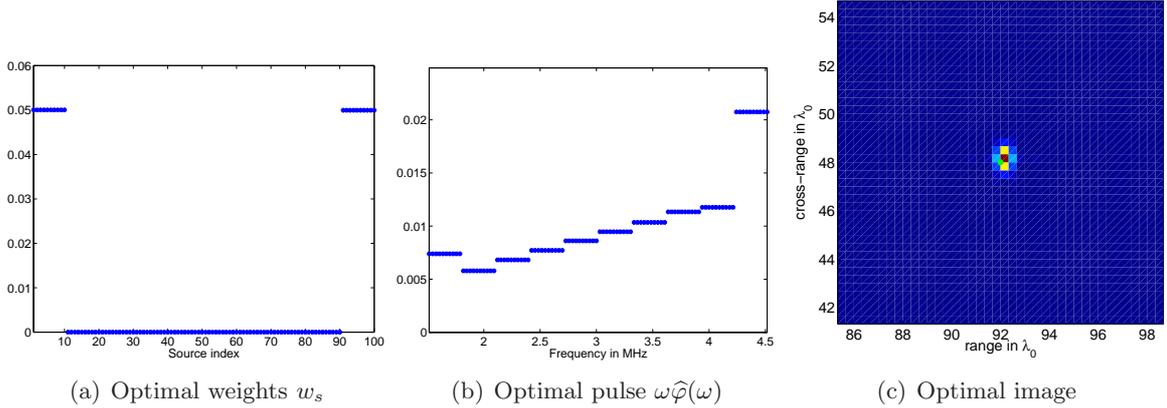
Figure 3: The one scatterer configuration. Optimal illumination for KM imaging.

For convenience, we choose a slightly different normalization of $\widehat{\varphi}(\omega)$,

$$\int_{|\omega-\omega_o|\leq B/2} \omega\widehat{\varphi}(\omega)d\omega = 1,$$

which corresponds to keeping a constant value of the peak of the image, as we we will see in section 6.2.1. This makes the division by the maximum of the image in (4.1) unnecessary in the simple case of a point scatterer.

To solve the optimization problem numerically, we discretize the bandwidth B in 10 sub-bands of width 0.3MHz and we look for a constant $\omega\varphi(\omega)$ in each sub-band. We also group the sources in blocks of 10 elements and take the weights w_s to be constant in each block. The number of variables in the optimization problem is 20.

The results of the optimization are shown in Figure 3. In Figure 3-(a) we show the optimal weights w_s, in Figure 3-(b) the optimal pulse $\omega\widehat{\varphi}(\omega)$ and in Figure 3-(c) the resulting image. By comparing Figure 3-(c) with 2-(c) we can clearly see that by using the optimal illumination for imaging we obtain a tighter image of the scatterer. On the other hand, the received power is lower, as can be seen in Table 1.

The results in Figure 3 are in very good agreement with the theoretical analysis of optimal illumination for a point scatterer (section 6.2.1). The weights w_s are large only at the edges of the array and the pulse increases linearly with the frequency. The deviations from linearity in Figure 3-(b) are due to the discretization and they diminish when we consider a finer frequency grid.

Remark: The results in Figure 3 correspond to a high SNR regime. We studied in [9] the case of low SNR due to instrument noise. This was done by introducing in the variational problem lower bound inequality constraints on the power generated by the illumination. As we decreased the signal to noise ratio (i.e. we increased the bound on the received power), we found in [9] that the illumination became closer and closer to that for optimal detection. This is to be expected.

The case of low SNR due to clutter is studied in [11]. We found there that the optimal pulses favor the lower frequencies in the bandwidth, because they are affected less by the scattering, and there is an overall blurring of the image. The source weights are also distributed in a more complicated manner in a cluttered medium.

4.2 Numerical results for four small not well-resolved scatterers

Now we consider four scatterers that are not well separated, in the sense explained in section 3.3. This means that they cannot be imaged one by one with DORT, because each singular vector is not associated to only one scatterer uniformly in the frequency band. The array-scatterer configuration is shown in Figure 4. The array and the bandwidth are as given in section 4.1. The range of the scatterers is $L = 90\lambda_o$ and they are separated by the distance $d = 3\lambda_0$. Each one is a disk of diameter λ_0, modeled as a soft acoustic scatterer, by setting the pressure to zero on its boundary. The response matrix is computed numerically in the time domain by solving the acoustic wave equation in two dimensions with the method described in [1, 2]. We model the infinite medium by surrounding the computational domain with a perfectly matched absorbing layer [3]. All the images in this section are displayed in a square of 31×31 pixels, with pixel size $\lambda_0/3 \times \lambda_0/3$.
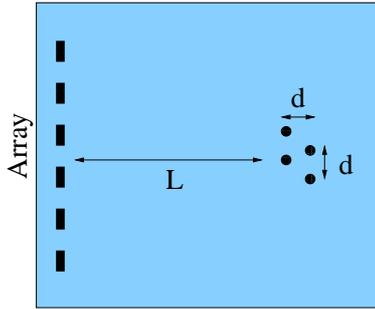
Figure 4: The four point scatterer configuration. The array has 100 elements at distance $\lambda_o/2$ apart and the range of the scatterers is $L = 90\lambda_o$.

4.2.1 Optimal illumination for detection

We begin with the optimal illumination for detection. We show in Figure 5 the first five singular values of the response matrix as a function of frequency. We observe four significant singular values, as expected, but they are not well separated over the bandwidth.
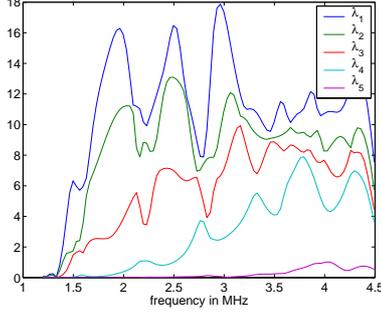
Figure 5: The first five singular values of the response matrix as a function of frequency.

In Figure 6-(a) we show the Kirchhoff migration image obtained with the illumination $\widehat{g}^\delta_{\max}(\vec{\mathbf{x}}_s, \omega)$ defined by (3.11). This maximizes the power of the echoes by selecting the singular vector at the resonant frequency of 2.9MHz, where $\sigma_1(\omega)$ attains its global maximum. Here the width δ is $B/100 = 0.03$MHz. To see the effect of this parameter on the received power and on the image we also show in Figure 6-(b) the results with a bigger $\delta = B/10 = 0.3$MHz. As expected, these illuminations do not give good images although they are very good for detection.
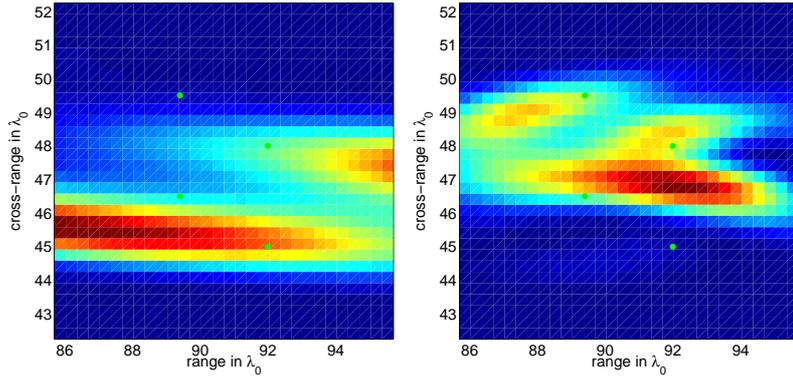
(a) $\widehat{g}^\delta_{\max}$ illumination, $\delta = 0.03$MHz. (b) $\widehat{g}^\delta_{\max}$ illumination, $\delta = 0.3$MHz.

Figure 6: The configuration of four scatterers. Optimal illumination for detection results. The scatterers are indicated with green dots.

In the top row of Figure 8, we show the DORT images given by illuminations

$$\widehat{g}(\vec{\mathbf{x}}_s, \omega) = \widehat{g}^{\mathrm{DORT}}_j(\vec{\mathbf{x}}_s, \omega) = \widehat{v}_j(\vec{\mathbf{x}}_s, \omega)/\sqrt{B},$$

with $j = 1, 2, 3$ and 4 from left to right, respectively. We see from these results that the scatterers are not well separated and they cannot be imaged selectively with one singular vector at a time.

4.2.2 Optimal illumination for Kirchhoff migration imaging

(a) Optimal weights w_s (b) Optimal pulse $\widehat{\varphi}(\omega)$ (c) Optimal image
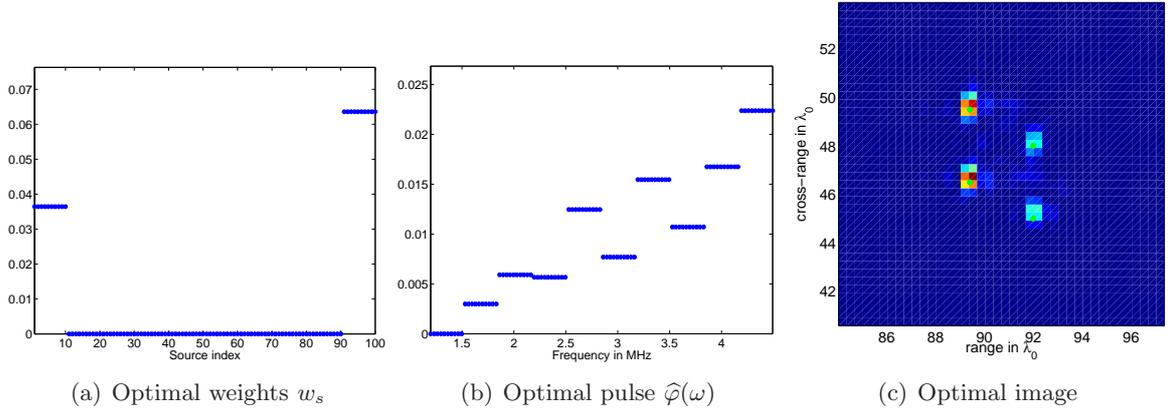
Figure 7: The four scatterers configuration. Optimal illumination for KM imaging.

We consider here the problem of optimal illumination for Kirchhoff migration imaging. As in the case of one scatterer, we seek the illumination in the separable set defined by (4.2), and we use the same discretization of $\widehat{\varphi}(\omega)$ and $w(\vec{\mathbf{x}}_s)$ as in section 4.1.2. The results are shown in Figure 7. The optimal weights correspond again to illumination from the edges of the array (cf. section 6.2) and the optimal pulse is increasing with frequency. We see in Figure 7-(c) that all the scatterers can be seen in the reconstructed image. The scatterers in the back appear weaker in the image because they are further from the array. This could be corrected using an amplitude factor in the backpropagation with the Green's function.

4.2.3 Optimal illumination and selective imaging

We show in Figure 8 two sets of results. First, we image as if the scatterers were well separated, with one singular vector at a time. These are the DORT images shown in the top row of Figure 8. In the bottom row, we show the results obtained with the selective imaging algorithm described in section 3.4.1. The subspace weights are shown in Figure 9.

To save computational time, we divide the bandwidth in 10 sub-bands of size 0.3MHz and set the subspace weights $\widehat{d}_j(\omega)$ constant in each sub-band. This means that we have 40 unknowns in the optimization. Finally, we show in Figure 10 how to improve the bottom right image in Figure 8, by optimizing over the source weights $\mathbf{w} = \{w_s\}$, as explained in section 3.4.2.
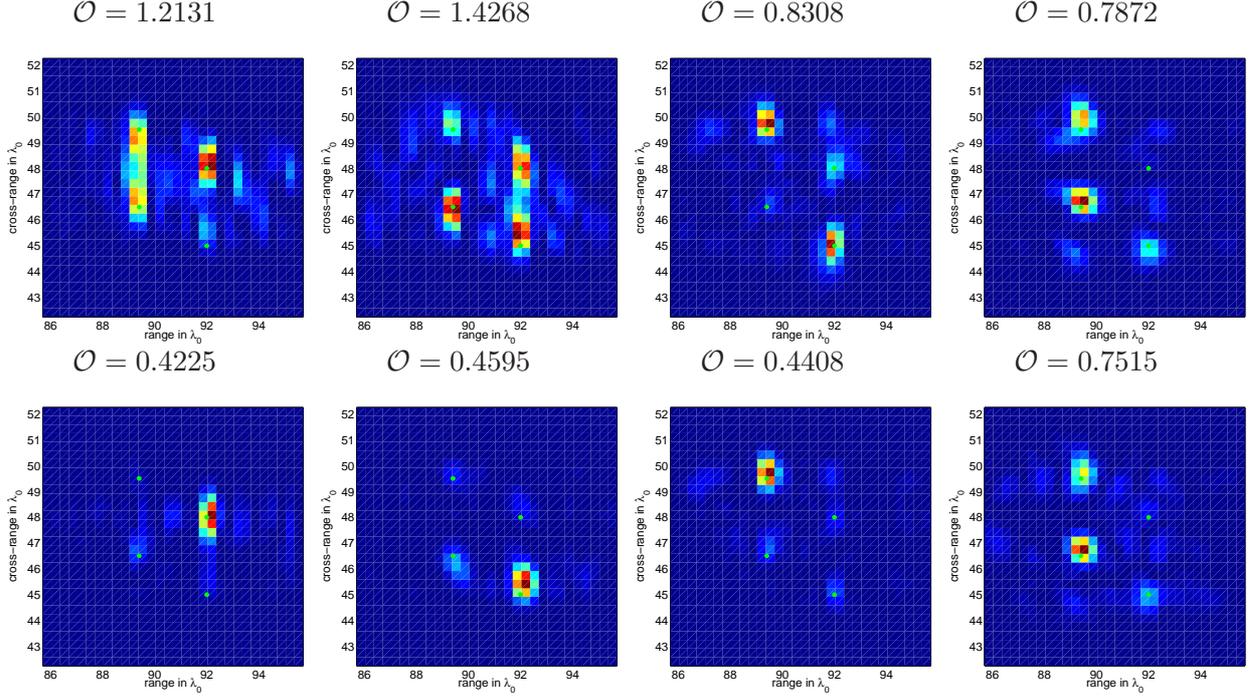
Figure 8: Top row: DORT images using the first, second, third and fourth singular vector accross the bandwidth. Bottom row: Images obtained with the selective imaging algorithm. We show from left to right the first four iterations. On top of each image we give the value of the objective function $\mathcal{O}$, i.e., the L^2 norm of the image normalized by its maximum.
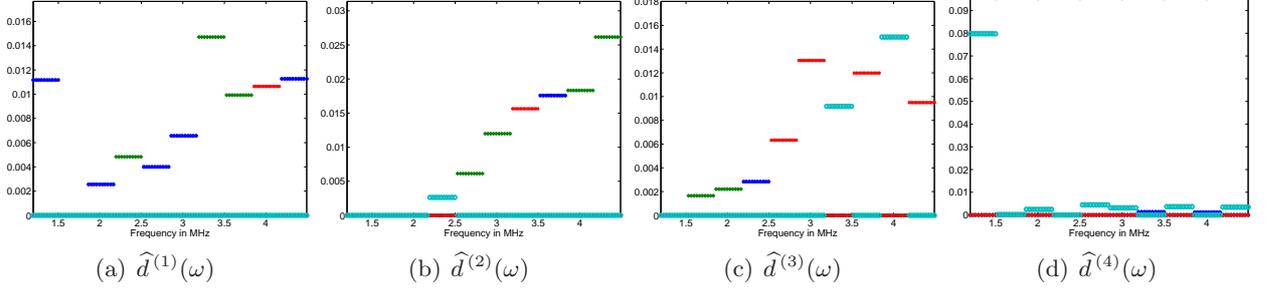
Figure 9: The four scatterer configuration. Optimal subspace weights. We show the first 4 iterations, from left to right. For each frequency sub-band we plot the largest weights. We use blue for $\widehat{d}_1^{(p)}(\omega)$, green for $\widehat{d}_2^{(p)}(\omega)$, red for $\widehat{d}_3^{(p)}(\omega)$ and cyan for $\widehat{d}_4^{(p)}(\omega)$, for $p = 1, \ldots, 4$.

5 Imaging in the Fraunhofer diffraction regime

We will analyze the effect of the illuminations on Kirchhoff migration and time reversal images in the Fraunhofer diffraction regime described in section 5.2. We rewrite the imaging functions (2.2)

(a) Optimal weights **w**
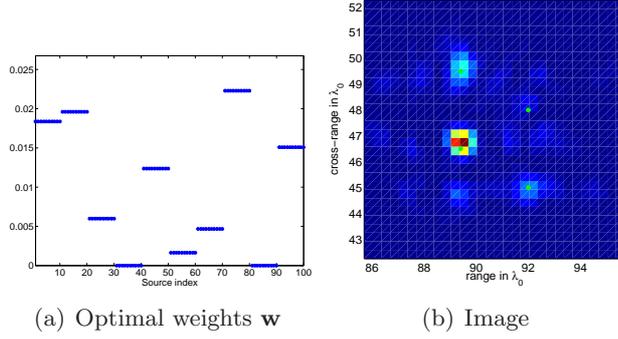
(b) Image

Figure 10: Improved bottom right image in Figure 8 with optimal array weight selection.

and (2.5) in this regime, in sections 5.4 and 5.5, respectively. The optimal illumination problem for these imaging functions is studied in section 6.

5.1 The array scatterer configuration

Let us begin with the imaging setup shown in Figure 11. The array is a square, of side a in 3-D and an interval of length a in 2-D. The reflector is at distance L from the array. We distinguish a center point $\vec{\mathbf{y}}^{\star}$ in the reflector and we define a system of coordinates with the origin at the center of the array and with range axis passing through $\vec{\mathbf{y}}^{\star}$. The support of the reflector is a domain of size h in the range direction and b in the cross-range. The planar (or linear) array is chosen for simplicity to be orthogonal to the range axis.

In our system of coordinates and in 3-D, the sources and receivers are located at

$$\vec{\mathbf{x}}_s = (0, \mathbf{x}_s), \quad \vec{\mathbf{x}}_r = (0, \mathbf{x}_r), \quad \mathbf{x}_s, \mathbf{x}_r \in \left[-\frac{a}{2}, \frac{a}{2}\right] \times \left[-\frac{a}{2}, \frac{a}{2}\right],$$

for $s, r = 1, \ldots, N$. In 2-D

$$\vec{\mathbf{x}}_s = (0, x_s), \quad \vec{\mathbf{x}}_r = (0, x_r), \quad x_s, x_r \in \left[-\frac{a}{2}, \frac{a}{2}\right].$$

The sources and receivers are closely spaced so that the array can be approximated by an aperture.

The reflector is centered at $\vec{\mathbf{y}}^{\star} = (L, \mathbf{0})$ and $\vec{\mathbf{y}}$ denotes an arbitrary point in its support. In 3-D we write $\vec{\mathbf{y}} = (L + \eta, \boldsymbol{\xi})$, with $\eta \in [-h/2, h/2]$ and $|\boldsymbol{\xi}| \leq b/2$, for $\boldsymbol{\xi} \in \mathbb{R}^2$. In 2-D we have $\vec{\mathbf{y}} = (L + \eta, \xi)$, with $\xi \in [-b/2, b/2]$. The same notation convention applies to search points $\vec{\mathbf{y}}^S$ where we image. In 3-D $\vec{\mathbf{y}}^S = (L + \eta^S, \boldsymbol{\xi}^S)$ for $\boldsymbol{\xi}^S \in \mathbb{R}^2$, and in 2-D $\vec{\mathbf{y}}^S = (L + \eta^S, \xi^S)$, for $\xi^S \in \mathbb{R}$.

5.2 Scaling and the Fraunhofer diffraction regime

The important length scales in the problem are the range L, the array aperture a, the thickness h and diameter b of the reflector and the carrier wavelength λ_o. For an arbitrary point $\vec{\mathbf{x}} = (0, \mathbf{x})$

25
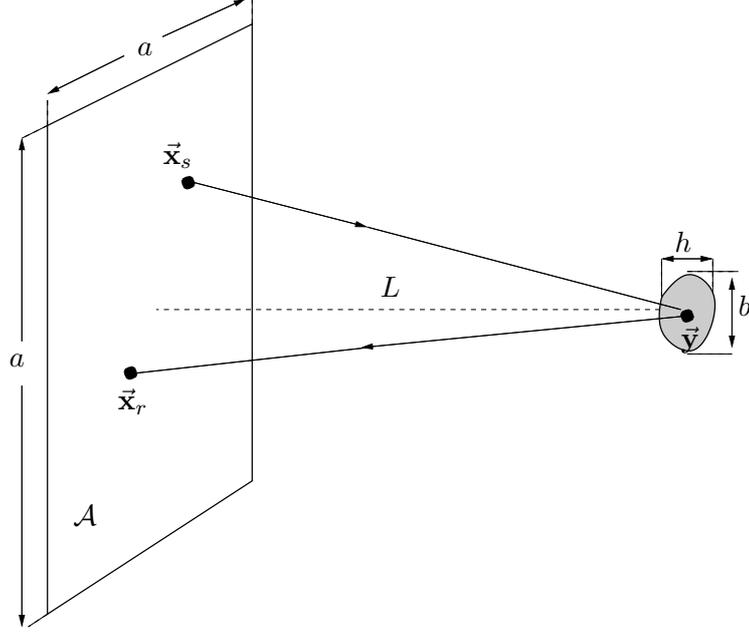
Figure 11: Setup for array imaging of an extended reflector. The illustration is in three dimensions, with a square array of aperture a.

in the array we have $|\mathbf{x}| = O(a)$ and for a point $\vec{\mathbf{y}} = (L + \eta, \boldsymbol{\xi})$ in the reflector we take $\eta = O(h)$ and $|\boldsymbol{\xi}| = O(b)$. We scale the same way the range and cross-range offsets of the search point $\vec{\mathbf{y}}^S = (L + \eta^S, \boldsymbol{\xi}^S)$, because we expect the image function to peak at the reflector. The frequencies are assumed to be $O(\omega_o)$ throughout the bandwidth.

In the scaling analysis of the imaging functions we encounter four dimensionless parameters

$$\theta_a = \frac{k_o a^2}{L}, \quad \theta_b = \frac{k_o b^2}{L}, \quad \theta_h = \frac{k_o h^2}{L}, \quad \theta_{ab} = \frac{k_o ab}{L}, \tag{5.1}$$

where $k_o = \omega_o/c_o$ is the central wave number. The first parameter in (5.1) is the Fresnel number and it is proportional to the ratio of the aperture a and the time reversal spot size $\lambda_o L/a$

$$\theta_a = \frac{2\pi a}{\lambda_o L/a}. \tag{5.2}$$

The remaining parameters in (5.1) are called Fresnel numbers by analogy.

We consider a high frequency regime with a small spot size

$$\theta_a \gg 1 \implies a \gg \frac{\lambda_o L}{a}, \tag{5.3}$$

and we suppose that the reflector is far enough from the array, so that

$$\frac{a}{L} \ll \frac{1}{\sqrt{\theta_a}} \ll 1. \tag{5.4}$$

The diameter b of the reflector is small, when compared with the aperture

$$\theta_b \ \ll \ 1 \Longrightarrow b \ll a, \tag{5.5}$$

but not with respect to the spot size

$$\theta_{ab} \sim 1 \Longrightarrow b \sim \frac{\lambda_o L}{a}. \tag{5.6}$$

The thickness h of the reflector satisfies

$$\theta_h \ll 1 \tag{5.7}$$

and therefore, by (5.3) and (5.4),

$$h \ll a \ll L. \tag{5.8}$$

We let further

$$\frac{h\theta_a}{L} \ll 1 \tag{5.9}$$

or, equivalently,

$$h \ll \frac{L^2}{k_o a^2}, \tag{5.10}$$

where $L^2/(k_o a^2)$ is the range resolution of images obtained with time harmonic signals, oscillating at frequency ω_o [14]. Thus, we ask that h be small with respect to the narrow-band resolution limit, but we can also have h comparable to the broadband resolution

$$h \sim \frac{c_o}{B}. \tag{5.11}$$

It is because of (5.6) and (5.11) that we call the reflector extended.

We wish to study the time reversal and Kirchhoff migration imaging functions (2.2) and (2.5) in the asymptotic regime defined by (5.3)-(5.11). We call it a Fraunhofer diffraction regime [14] because it allows us to set the analysis in the framework of Fourier transforms, as explained in detail in the following sections. Here we note that although most of the analysis applies to imaging generic extended reflectors, we shall consider point-like reflectors with $b \ll \lambda_o L/a$ and $h \ll c_o/\omega_o$ as well. We shall also look at imaging with very large arrays ($\lambda_o L/a \ll b$).

5.3 The response matrix in the Fraunhofer regime

In the Fraunhofer diffraction regime defined by (5.3)-(5.11), the Green's function is given by

$$\widehat{G}_o(\vec{\mathbf{x}}, \vec{\mathbf{y}}, \omega) \approx \frac{\alpha(L)}{k^{(3-d)/2}} e^{ik|\vec{\mathbf{x}} - \vec{\mathbf{y}}|},$$

with amplitude

$$\alpha(L) = \begin{cases} \frac{1}{4\pi L} & \text{in 3-D,} \\[2ex] \frac{1}{2}\sqrt{\frac{i}{2\pi L}} & \text{in 2-D.} \end{cases} \tag{5.12}$$

Here $d = 3$ in 3-D and $d = 2$ in 2-D. This is because for $\vec{\mathbf{x}} = (0, \mathbf{x})$ and $\vec{\mathbf{y}} = (L + \eta, \boldsymbol{\xi})$, we can write

$$|\vec{\mathbf{x}} - \vec{\mathbf{y}}| = [(L+\eta)^2 + |\mathbf{x} - \boldsymbol{\xi}|^2]^{\frac{1}{2}} = L\left[1 + O\left(\frac{h}{L}\right) + O\left(\frac{a^2}{L^2}\right)\right] \approx L.$$

The phase of $\widehat{G}_o$ can also be approximated as

$$k|\vec{\mathbf{x}} - \vec{\mathbf{y}}| = k\left(L + \eta + \frac{|\mathbf{x}|^2}{2L} - \frac{\mathbf{x} \cdot \boldsymbol{\xi}}{L}\right) + O\left(\theta_b + \theta_h + \theta_a \frac{h}{L} + \theta_a \frac{a^2}{L^2}\right) \approx k\left(L + \eta + \frac{|\mathbf{x}|^2}{2L} - \frac{\mathbf{x} \cdot \boldsymbol{\xi}}{L}\right),$$

and we obtain

$$\widehat{G}_o(\vec{\mathbf{x}}, \vec{\mathbf{y}}, \omega) \approx \widehat{\mathcal{G}}_o(\vec{\mathbf{x}}, \vec{\mathbf{y}}, \omega) = \frac{\alpha(L)}{k^{(3-d)/2}} e^{ik\left(L + \eta + \frac{|\mathbf{x}|^2}{2L} - \frac{\mathbf{x} \cdot \boldsymbol{\xi}}{L}\right)}. \tag{5.13}$$

In the Born approximation, the response matrix is given by

$$\begin{aligned}
\widehat{\Pi}(\vec{\mathbf{x}}_r, \vec{\mathbf{x}}_s, \omega) &\approx k^2 \int d\vec{\mathbf{y}} \rho(\vec{\mathbf{y}}) \widehat{\mathcal{G}}_o(\vec{\mathbf{x}}_r, \vec{\mathbf{y}}, \omega) \widehat{\mathcal{G}}_o(\vec{\mathbf{x}}_s, \vec{\mathbf{y}}, \omega) \\
&= k^2 \widehat{\mathcal{G}}_o(\vec{\mathbf{x}}_r, \vec{\mathbf{y}}^\star, \omega) \widehat{\mathcal{G}}_o(\vec{\mathbf{x}}_s, \vec{\mathbf{y}}^\star, \omega) \int d\eta \int d\boldsymbol{\xi}\, \rho(L + \eta, \boldsymbol{\xi}) e^{2ik\eta - \frac{ik(\mathbf{x}_r + \mathbf{x}_s)}{L} \cdot \boldsymbol{\xi}}, \tag{5.14}
\end{aligned}$$

where we recall that $\vec{\mathbf{y}}^\star = (L, \mathbf{0})$. This equation involves the Fourier transform of the reflectivity function

$$\begin{aligned}
\widehat{\rho}(\zeta, \boldsymbol{\beta}) &= \int dz \int d\boldsymbol{\xi}\, \rho(z, \boldsymbol{\xi}) e^{-i\zeta z - i\boldsymbol{\beta} \cdot \boldsymbol{\xi}} \\
&= e^{-i\zeta L} \int d\eta \int d\boldsymbol{\xi}\, \rho(L + \eta, \boldsymbol{\xi}) e^{-i\zeta\eta - i\boldsymbol{\beta} \cdot \boldsymbol{\xi}} = e^{-i\zeta L} \widehat{\rho}_L(\zeta, \beta), \tag{5.15}
\end{aligned}$$

so we can rewrite it as

$$\widehat{\Pi}(\vec{\mathbf{x}}_r, \vec{\mathbf{x}}_s, \omega) \approx \widehat{\Pi}_F(\vec{\mathbf{x}}_r, \vec{\mathbf{x}}_s, \omega) = k^2 \widehat{\mathcal{G}}_o(\vec{\mathbf{x}}_r, \vec{\mathbf{y}}^\star, \omega) \widehat{\mathcal{G}}_o(\vec{\mathbf{x}}_s, \vec{\mathbf{y}}^\star, \omega) \widehat{\rho}_L\left(-2k, \frac{k(\mathbf{x}_r + \mathbf{x}_s)}{L}\right), \tag{5.16}$$

where $\widehat{\Pi}_F(\omega)$ stands for the response matrix in the Fraunhofer regime. We use this formula next to analyse time reversal and Kirchhoff migration imaging in the Fraunhofer regime.

5.4 Time reversal in the Fraunhofer regime

The time reversal imaging function is given by

$$\mathcal{I}^{\mathrm{TR}}(\vec{\mathbf{y}}^S; \widehat{g}) \approx \int_{|\omega - \omega_o| \leq B/2} d\omega \sum_{r=1}^{N} \widehat{\mathcal{G}}_o(\vec{\mathbf{x}}_r, \vec{\mathbf{y}}^S, \omega) \sum_{s=1}^{N} \overline{\widehat{\Pi}_F(\vec{\mathbf{x}}_r, \vec{\mathbf{x}}_s, \omega) \widehat{g}(\vec{\mathbf{x}}_s, \omega)}, \tag{5.17}$$

for some illumination waveform $\widehat{g}(\vec{\mathbf{x}}_s, \omega)$ that we wish to optimize. Now the illumination vector

$$\widehat{\mathbf{g}}(\omega) = \{\widehat{g}(\vec{\mathbf{x}}_s, \omega)\}_{1 \leq s \leq N}$$

is in $\mathbb{C}^N$, so we can write it as

$$\widehat{\mathbf{g}}(\omega) = \sum_{n=1}^{N} \widehat{d}_n(\omega)\widehat{\mathbf{v}}_n(\omega), \qquad \widehat{\mathbf{v}}_n(\omega) = (\widehat{v}_n(\vec{\mathbf{x}}_1, \omega), \dots, \widehat{v}_n(\vec{\mathbf{x}}_N, \omega))^T, \tag{5.18}$$

using the basis $\{\widehat{\mathbf{v}}_n(\omega)\}_{n \geq 1}$ of the right singular vectors of $\widehat{\Pi}_F(\omega)$.

Assume a decreasing ordering of the singular values $\sigma_n(\omega)$ and note that, for sufficiently large N, there is a threshold $n^\star(\omega)$ above which

$$\sigma_n(\omega) \approx 0 \ \text{ for } n > n^\star(\omega).$$

This threshold depends on the diameter b of the reflector. It is $O\left(\frac{b}{\lambda L/a}\right)$ in 2-D and $O\left(\frac{b}{\lambda L/a}\right)^2$ in 3-D, as noted in [28] and as follows from the analysis of section 7. We can truncate then the sum in (5.18) to the first $n^\star(\omega)$ terms

$$\widehat{g}(\vec{\mathbf{x}}_s, \omega) = \sum_{n=1}^{n^\star(\omega)} \widehat{d}_n(\omega)\widehat{v}_n(\vec{\mathbf{x}}_s, \omega), \tag{5.19}$$

to stay outside the null space of $\widehat{\Pi}_F(\omega)$. This way, we receive echoes at the array for any non-trivial choice of the coefficients $\widehat{d}_n(\omega)$ that we wish to determine optimally.

5.4.1 The singular value decomposition in the Fraunhofer regime

Now let us write the SVD of the complex symmetric response matrix $\widehat{\Pi}_F(\omega)$

$$\sum_{s=1}^{N} \widehat{\Pi}_F(\vec{\mathbf{x}}_r, \vec{\mathbf{x}}_s, \omega)\widehat{v}_n(\vec{\mathbf{x}}_s, \omega) = \sigma_n(\omega)\overline{\widehat{v}_n(\vec{\mathbf{x}}_r, \omega)}. \tag{5.20}$$

We use the expression (5.16) of $\widehat{\Pi}_F(\omega)$ and seek the singular vectors in the form

$$\widehat{v}_n(\vec{\mathbf{x}}_s, \omega) = \overline{\widehat{\mathcal{G}}_o(\vec{\mathbf{x}}_s, \vec{\mathbf{y}}^\star, \omega)}\widehat{V}_n(\vec{\mathbf{x}}_s, \omega). \tag{5.21}$$

The first factor corresponds to the singular vector for a point scatterer at $\vec{\mathbf{y}}^\star$. The second factor is determined by the reflectivity function, as follows below.

Substituting (5.21) in (5.20), we obtain

$$
\begin{aligned}
\sum_{s=1}^{N} \widehat{\Pi}_F(\vec{\mathbf{x}}_r, \vec{\mathbf{x}}_s, \omega)\widehat{v}_n(\vec{\mathbf{x}}_s, \omega) &= k^{d-1}|\alpha(L)|^2 \widehat{\mathcal{G}}_o(\vec{\mathbf{x}}_r, \vec{\mathbf{y}}^\star, \omega) \sum_{s=1}^{N} \widehat{\rho}_L\left(-2k, \frac{k(\mathbf{x}_r + \mathbf{x}_s)}{L}\right) \widehat{V}_n(\vec{\mathbf{x}}_s, \omega) \\
&= \sigma_n(\omega)\widehat{\mathcal{G}}_o(\vec{\mathbf{x}}_r, \vec{\mathbf{y}}^\star, \omega)\overline{\widehat{V}_n(\vec{\mathbf{x}}_r, \omega)},
\end{aligned}
\tag{5.22}
$$

because $|\widehat{\mathcal{G}}_o(\vec{\mathbf{x}}_s, \vec{\mathbf{y}}^\star, \omega)| = |\alpha(L)|/k^{(3-d)/2}$. This reduces to another SVD problem, for a complex symmetric matrix with entries given by the Fourier coefficients of the reflectivity,

$$\sum_{s=1}^{N} \widehat{\rho}_L\left(-2k, \frac{k(\mathbf{x}_r + \mathbf{x}_s)}{L}\right) \widehat{V}_n(\vec{\mathbf{x}}_s, \omega) = \frac{\sigma_n(\omega)}{k^{d-1}|\alpha(L)|^2}\overline{\widehat{V}_n(\vec{\mathbf{x}}_r, \omega)}, \tag{5.23}$$

$$\|\widehat{\mathbf{v}}_n\| = \frac{|\alpha(L)|}{k^{(3-d)/2}}\|\widehat{\mathbf{V}}_n\| = 1. \tag{5.24}$$

29

We derive later, in section 7.1, explicit formulas for $\widehat{\mathbf{V}}_n(\vec{\mathbf{x}}_s, \omega)$, in the special case of the reflectivity of a strip. Here we let ρ be a general reflectivity and we write next the imaging function $\mathcal{I}^{\mathrm{TR}}$ and its L^2 norm.

5.4.2 The time reversal imaging function

Let us also suppose from now on that we have a dense sampling of the array aperture by the sources and the receivers, so that we can write

$$\sum_{r=1}^{N} \sim \int_{\mathcal{A}} d\mathbf{x}_r, \quad \sum_{s=1}^{N} \sim \int_{\mathcal{A}} d\mathbf{x}_s. \tag{5.25}$$

Here $\mathbf{x}_r$ and $\mathbf{x}_s$ vary continuously in $\mathcal{A}$, but we keep the indices to distinguish between the sources and receivers. The symbol $\sim$ means approximate up to a multiplicative constant, as before. Using equation (5.21) in (5.17) and (5.19), we obtain the imaging function

$$\mathcal{I}^{\mathrm{TR}}(\vec{\mathbf{y}}^S; \widehat{g}) \quad \sim \quad \int_{|\omega - \omega_o| \leq B/2} d\omega \sum_{n=1}^{n^\star(\omega)} \overline{\widehat{d}_n(\omega)} \sigma_n(\omega) \int_{\mathcal{A}} d\mathbf{x}_r \, \widehat{\mathcal{G}}_o(\vec{\mathbf{x}}_r, \vec{\mathbf{y}}^S, \omega) \overline{\widehat{\mathcal{G}}_o(\vec{\mathbf{x}}_r, \vec{\mathbf{y}}^\star, \omega)} \widehat{V}_n(\vec{\mathbf{x}}_r, \omega)$$

$$\sim \quad \int_{|\omega - \omega_o| \leq B/2} d\omega \, \omega^{d-3} \sum_{n=1}^{n^\star(\omega)} \overline{\widehat{d}_n(\omega)} \sigma_n(\omega) e^{ik\eta^S} \int_{\mathcal{A}} d\mathbf{x}_r \, e^{\frac{ik\mathbf{x}_r}{L} \cdot \boldsymbol{\xi}^S} \widehat{V}_n(\vec{\mathbf{x}}_r, \omega). \tag{5.26}$$

Remark: We note from (5.26) that in the Fraunhofer diffraction regime, the cross-range $(\boldsymbol{\xi}^S)$ dependence in the time reversal imaging function is given by the Fourier transform of the singular vectors $\widehat{V}_n(\vec{\mathbf{x}}_r, \omega)$, with respect to the receiver coordinates $\mathbf{x}_r \in \mathcal{A}$.

The $L^2(\mathcal{D})$ norm of the image function is

$$\left\| \mathcal{I}^{\mathrm{TR}}(\cdot; \widehat{g}) \right\|^2 \sim \iint_{\substack{|\omega - \omega_o| \leq B/2 \\ |\omega' - \omega_o| \leq B/2}} d\omega \, d\omega' (\omega\omega')^{d-3} \sum_{n=1}^{n^\star(\omega)} \sum_{n'=1}^{n^\star(\omega)} \overline{\widehat{d}_n(\omega)} \widehat{d}_{n'}(\omega') \sigma_n(\omega) \sigma_{n'}(\omega') \int d\eta^S e^{i(k-k')\eta^S}$$

$$\int_{\mathcal{A}} d\mathbf{x}_r \, \widehat{V}_n(\vec{\mathbf{x}}_r, \omega) \int_{\mathcal{A}} d\mathbf{x}_{r'} \, \overline{\widehat{V}_{n'}(\vec{\mathbf{x}}_{r'}, \omega')} \int d\boldsymbol{\xi}^S e^{\frac{i(k\mathbf{x}_r - k'\mathbf{x}_{r'})}{L} \cdot \boldsymbol{\xi}^S} \tag{5.27}$$

where the integrals over η^S and ξ^S extend over the search domain $\mathcal{D}$. We know that any reasonable illumination gives an image that is large near the reflector and small elsewhere, so let us extend $\mathcal{D}$ to the entire space $\mathbb{R}^3$, for the purpose of our analysis. We get this way

$$\int_{-\infty}^{\infty} d\eta^S e^{i(k-k')\eta^S} = 2\pi\delta(k - k'),$$

$$\int_{\mathbb{R}^2} d\boldsymbol{\xi}^S e^{\frac{i(k\mathbf{x}_r - k'\mathbf{x}_{r'})}{L} \cdot \boldsymbol{\xi}^S} = (2\pi)^2 \delta\left(\frac{k\mathbf{x}_r - k'\mathbf{x}_{r'}}{L} \right).$$

Equation (5.27) becomes

$$\left\| \mathcal{I}^{\mathrm{TR}}(\cdot; \widehat{g}) \right\|^2 \sim \int_{|\omega - \omega_o| \leq B/2} \frac{d\omega}{\omega^2} \sum_{n=1}^{n^\star(\omega)} \sigma_n^2(\omega) |\widehat{d}_n(\omega)|^2, \tag{5.28}$$

due to the ortogonality of the singular vectors

$$\frac{k^{3-d}}{|\alpha(L)|^2}\delta_{n,n'} = \sum_{r=1}^{N} \widehat{V}_n(\vec{\mathbf{x}}_r,\omega)\overline{\widehat{V}_{n'}(\vec{\mathbf{x}}_r,\omega)} \sim \int_{\mathcal{A}} d\mathbf{x}_r \widehat{V}_n(\vec{\mathbf{x}}_r,\omega)\overline{\widehat{V}_{n'}(\vec{\mathbf{x}}_r,\omega)}, \quad \vec{\mathbf{x}}_r = (0,\mathbf{x}_r),$$

and the property

$$\delta\left(\frac{k(\mathbf{x}_r - \mathbf{x}_{r'})}{L}\right) = \left(\frac{L}{k}\right)^{d-1}\delta(\mathbf{x}_r - \mathbf{x}_{r'})$$

of the $\delta(\cdot)$ function.

5.5 Kirchhoff migration in the Fraunhofer regime

The expression (2.5) of the Kirchhoff migration imaging function in the Fraunhofer regime is,

$$\mathcal{I}^{\mathrm{KM}}(\vec{\mathbf{y}}^S;\widehat{f}) \sim \int_{|\omega-\omega_o|\leq B/2} d\omega \int_{\mathcal{A}} d\mathbf{x}_r \, \overline{\widehat{\mathcal{G}}_o(\vec{\mathbf{x}}_r,\vec{\mathbf{y}}^S,\omega)}\widehat{\mathcal{G}}_o(\vec{\mathbf{x}}_r,\vec{\mathbf{y}}^\star,\omega) \int_{\mathcal{A}} d\mathbf{x}_s \, \omega^2 \widehat{f}(\vec{\mathbf{x}}_s,\omega)\overline{\widehat{\mathcal{G}}_o(\vec{\mathbf{x}}_s,\vec{\mathbf{y}}^S,\omega)}$$

$$\widehat{\mathcal{G}}_o(\vec{\mathbf{x}}_s,\vec{\mathbf{y}}^\star,\omega)\widehat{\rho}_L\left(-2k,\frac{k(\mathbf{x}_r+\mathbf{x}_s)}{L}\right),$$

where we used approximation (5.16) of $\widehat{\Pi}(\vec{\mathbf{x}}_r,\vec{\mathbf{x}}_s,\omega)$. Now using the identity

$$\overline{\widehat{\mathcal{G}}_o(\vec{\mathbf{x}}_r,\vec{\mathbf{y}}^S,\omega)}\widehat{\mathcal{G}}_o(\vec{\mathbf{x}}_r,\vec{\mathbf{y}}^\star,\omega) = |\widehat{\mathcal{G}}_o(\vec{\mathbf{x}}_r,\vec{\mathbf{y}}^\star,\omega)|^2 e^{-ik\eta^S + \frac{ik\mathbf{x}_r\cdot\boldsymbol{\xi}^S}{L}} = \frac{|\alpha(L)|^2}{k^{3-d}}e^{-ik\eta^S + \frac{ik\mathbf{x}_r\cdot\boldsymbol{\xi}^S}{L}},$$

we can write

$$\mathcal{I}^{\mathrm{KM}}(\vec{\mathbf{y}}^S;\widehat{f}) \sim \int_{|\omega-\omega_o|\leq B/2} d\omega \int_{\mathcal{A}} d\mathbf{x}_r \int_{\mathcal{A}} d\mathbf{x}_s \, \widehat{f}(\vec{\mathbf{x}}_s,\omega)k^{d-1}\widehat{\rho}_L\left(-2k,\frac{k(\mathbf{x}_s+\mathbf{x}_r)}{L}\right)$$

$$\exp\left[-2ik\eta^S + \frac{ik(\mathbf{x}_r+\mathbf{x}_s)\cdot\boldsymbol{\xi}^S}{L}\right]. \qquad (5.29)$$

5.5.1 Imaging with large arrays

Let us suppose for a moment that we have a very large array, so that the spot size $\lambda_o L/a \ll b$. The imaging function is given by (5.29), in terms of the integral over the receivers

$$I(\mathbf{x}_s,\boldsymbol{\xi}^S,\omega) = \int_{\mathcal{A}} d\mathbf{x}_r \, \widehat{\rho}_L\left(-2k,\frac{k\mathbf{x}_s}{L}+\frac{k\mathbf{x}_r}{L}\right)\exp\left[\frac{ik(\mathbf{x}_r+\mathbf{x}_s)\cdot\boldsymbol{\xi}^S}{L}\right]. \qquad (5.30)$$

Now, since $\rho(\vec{\mathbf{y}})$ has cross-range support of order b, its Fourier transform $\widehat{\rho}(\zeta,\boldsymbol{\beta})$ is supported on $|\boldsymbol{\beta}| \leq O(b^{-1})$ and, as $\mathbf{x}_r$ varies in $\mathcal{A}$, $k\mathbf{x}_r/L$ covers a domain of diameter $O\left(\frac{a}{\lambda_o L}\right) \gg O(b^{-1})$. This allows us to approximate the integral in (5.30) by

$$I(\mathbf{x}_s,\boldsymbol{\xi}^S,\omega) \approx \int_{\mathbb{R}^2} d\mathbf{x}_r \, \widehat{\rho}_L\left(-2k,\frac{k\mathbf{x}_s}{L}+\frac{k\mathbf{x}_r}{L}\right)\exp\left[\frac{ik(\mathbf{x}_r+\mathbf{x}_s)\cdot\boldsymbol{\xi}^S}{L}\right] \sim k^{-2}\widetilde{\rho}_L(-2k,\boldsymbol{\xi}^S), \quad (5.31)$$

31

where $\tilde{\rho}_L$ is the phase shifted partial Fourier transform of ρ, with respect to the range coordinate

$$\int dz\, \rho(z, \boldsymbol{\xi}) e^{-i\zeta z} = e^{-i\zeta L} \int d\eta\, \rho(L + \eta, \boldsymbol{\xi}) e^{-i\zeta\eta} = e^{-i\zeta L} \tilde{\rho}_L(\zeta, \boldsymbol{\xi}). \tag{5.32}$$

We obtain the imaging function

$$\mathcal{I}^{\mathrm{KM}}(\vec{\mathbf{y}}^S; \hat{f}) \sim \int_{|\omega - \omega_o| \leq B/2} d\omega \left[\int_{\mathcal{A}} d\mathbf{x}_s\, \hat{f}(\vec{\mathbf{x}}_s, \omega) \right] \tilde{\rho}_L \left(-2k, \boldsymbol{\xi}^S \right) e^{-2ik\eta^S} \tag{5.33}$$

in 3-D, which has perfect cross-range resolution, due to the very large (essentially infinite) array. This is well known [4] and it means that the optimization of $\hat{f}(\vec{\mathbf{x}}_s, \omega)$ over $\vec{\mathbf{x}}_s$ becomes unnecessary for infinite arrays. It is only for finite apertures that the optimal illumination question becomes interesting. The range resolution in (5.33) is dependent on the bandwidth and it can be improved by optimizing the pulse shape over frequencies.

5.5.2 The L^2 norm of the Kirchhoff migration image

It remains to compute the $L^2(\mathcal{D})$ norm of the image which we wish to minimize over the illumination intensities $\hat{f}(\vec{\mathbf{x}}_s, \omega)$. We have in 3-D

$$\left\| \mathcal{I}^{\mathrm{KM}}(\cdot; \hat{f}) \right\|^2 \sim \int_{|\omega - \omega_o| \leq B/2} d\omega\, k^2 \int_{|\omega - \omega_o| \leq B/2} d\omega'\, (k')^2 \int_{\mathcal{A}} d\mathbf{x}_r \int_{\mathcal{A}} d\mathbf{x}'_r \int_{\mathcal{A}} d\mathbf{x}_s \int_{\mathcal{A}} d\mathbf{x}'_s\, \hat{f}(\vec{\mathbf{x}}_s, \omega) \hat{f}(\vec{\mathbf{x}}'_s, \omega')$$

$$\hat{\rho}_L \left(-2k, \frac{k(\mathbf{x}_s + \mathbf{x}_r)}{L} \right) \overline{\hat{\rho}_L \left(-2k', \frac{k'(\mathbf{x}'_s + \mathbf{x}'_r)}{L} \right)} \int_{-\infty}^{\infty} d\eta^S\, e^{2i(k'-k)\eta^S}$$

$$\int_{\mathbb{R}^2} d\boldsymbol{\xi}^S \exp \left\{ \frac{i\left[k(\mathbf{x}_s + \mathbf{x}_r) - k'(\mathbf{x}'_s + \mathbf{x}'_r) \right] \cdot \boldsymbol{\xi}^S}{L} \right\}, \tag{5.34}$$

where we extend the search domain to the whole $\mathbb{R}^3$, as in the previous section. Integrating over η^S, $\boldsymbol{\xi}^S$ and ω' we have

$$\left\| \mathcal{I}^{\mathrm{KM}}(\cdot; \hat{f}) \right\|^2 \sim \int_{|\omega - \omega_o| \leq B/2} d\omega \int_{\mathcal{A}} d\mathbf{x}_s \int_{\mathcal{A}} d\mathbf{x}'_s\, \hat{f}(\vec{\mathbf{x}}_s, \omega) \hat{f}(\vec{\mathbf{x}}'_s, \omega) \int_{\mathcal{A}} d\mathbf{x}_r \left| k^2 \hat{\rho}_L \left(-2k, \frac{k(\mathbf{x}_s + \mathbf{x}_r)}{L} \right) \right|^2$$

$$\int_{\mathcal{A}} d\mathbf{x}'_r \left(\frac{L}{k} \right)^2 \delta(\mathbf{x}_s + \mathbf{x}_r - \mathbf{x}'_s - \mathbf{x}'_r). \tag{5.35}$$

Next, we make the change of variables

$$\overline{\mathbf{x}} = \frac{\mathbf{x}_r + \mathbf{x}'_r}{2}, \quad \tilde{\mathbf{x}} = \mathbf{x}_r - \mathbf{x}'_r, \tag{5.36}$$

which gives

$$\int_{-a/2}^{a/2} d(x_r)_j \int_{-a/2}^{a/2} d(x'_r)_j = \int_{-a}^{a} d\tilde{x}_j \int_{-\frac{a}{2} + \frac{|\tilde{x}_j|}{2}}^{\frac{a}{2} - \frac{|\tilde{x}_j|}{2}} d\overline{x}_j, \quad j = 1, 2. \tag{5.37}$$

32

Integrating over $\tilde{\mathbf{x}}$, we obtain

$$\left\|\mathcal{I}^{\text{KM}}(\cdot;\widehat{f})\right\|^2 \sim \int_{|\omega-\omega_o|\le B/2} d\omega \int_{\mathcal{A}} d\mathbf{x}_s \int_{\mathcal{A}} d\mathbf{x}'_s \frac{\widehat{f}(\vec{\mathbf{x}}_s,\omega)\widehat{f}(\vec{\mathbf{x}}'_s,\omega)}{\omega^2}$$

$$\prod_{j=1}^{2} \int_{-\frac{a}{2}+\frac{|(\mathbf{x}'_s-\mathbf{x}_s)_j|}{2}}^{\frac{a}{2}-\frac{|(\mathbf{x}'_s-\mathbf{x}_s)_j|}{2}} d\bar{x}_j \left| k^2 \widehat{\rho}_L \left(-2k, \frac{k}{L}\left(\overline{\mathbf{x}}+\frac{\mathbf{x}_s+\mathbf{x}'_s}{2}\right)\right)\right|^2. \tag{5.38}$$

This is in 3-D and for $\vec{\mathbf{x}}_s = (0, \mathbf{x}_s)$. In 2-D, $\vec{\mathbf{x}}_s = (0, x_s)$, for $x_s \in [-a/2, a/2]$ and the result is

$$\left\|\mathcal{I}^{\text{KM}}(\cdot;\widehat{f})\right\|^2 \sim \int_{|\omega-\omega_o|\le B/2} d\omega \int_{-a/2}^{a/2} dx_s \int_{-a/2}^{a/2} dx'_s \frac{\widehat{f}(\vec{\mathbf{x}}_s,\omega)\widehat{f}(\vec{\mathbf{x}}'_s,\omega)}{\omega}$$

$$\int_{-\frac{a}{2}+\frac{|x'_s-x_s|}{2}}^{\frac{a}{2}-\frac{|x'_s-x_s|}{2}} d\bar{x} \left| k\widehat{\rho}_L \left(-2k, \frac{k}{L}\left(\bar{x}+\frac{x_s+x'_s}{2}\right)\right)\right|^2 \quad \text{in 2-D.} \tag{5.39}$$

6 Variational analysis in the Fraunhofer regime

We consider here the optimal illuminations $\widehat{g}(\vec{\mathbf{x}}_s,\omega)$ and $\widehat{f}(\vec{\mathbf{x}}_s,\omega)$ that minimize the support of the time reversal and Kirchhoff migration images in the L^2 sense.

6.1 Optimal illumination for time reversal imaging

The L^2 norm of the time reversal image, with illumination

$$\widehat{g}(\vec{\mathbf{x}}_s,\omega) = \sum_{n=1}^{n^\star(\omega)} \widehat{d}_n(\omega)\widehat{v}_n(\vec{\mathbf{x}}_s,\omega), \quad \widehat{v}_n(\vec{\mathbf{x}}_s,\omega) = \overline{\mathcal{G}_o(\vec{\mathbf{x}}_s,\vec{\mathbf{y}}^\star,\omega)}\widehat{V}_n(\vec{\mathbf{x}}_s,\omega), \tag{6.1}$$

is given by (5.28). Recall (5.23) and the continuum approximation of the array. We have that the singular functions $\widehat{V}_n$ satisfy the integral equation

$$\int_{\mathcal{A}} d\mathbf{x}_s\, \widehat{\rho}_L \left(-2k, \frac{k(\mathbf{x}_r+\mathbf{x}_s)}{L}\right)\widehat{V}_n(\vec{\mathbf{x}}_s,\omega) = \frac{\sigma_n(\omega)}{k^{d-1}|\alpha(L)|^2}\overline{\widehat{V}_n(\vec{\mathbf{x}}_r,\omega)} \tag{6.2}$$

and we normalize them as

$$\|\widehat{v}_n(\cdot,\omega)\|^2 = \frac{|\alpha(L)|^2}{k^{3-d}}\int_{\mathcal{A}} d\mathbf{x}_s\, |\widehat{V}_n(\vec{\mathbf{x}}_s,\omega)|^2 = 1. \tag{6.3}$$

Moreover, using the orthogonality of $\widehat{v}_n(\vec{\mathbf{x}}_s,\omega)$, we get

$$\int_{\mathcal{A}} d\mathbf{x}_s\, |\widehat{g}(\vec{\mathbf{x}}_s,\omega)|^2 = \sum_{n=1}^{n^\star(\omega)} |\widehat{d}_n(\omega)|^2 = |\widehat{\varphi}(\omega)|^2, \tag{6.4}$$

where $\widehat{\varphi}(\omega)$ could be known apriori or we can select it with some optimization criterion.

33

The question is how to choose the coefficients $\widehat{d}_n(\omega)$ in order to minimize the L^2 norm of the image? The result follows easily from (5.28),

$$\widehat{d}_n(\omega) = \widehat{\varphi}(\omega)\delta_{nn^\star(\omega)}, \quad |\omega - \omega_o| \leq \frac{B}{2}, \tag{6.5}$$

because the singular functions are smallest at the threshold $n^\star(\omega)$. In general, it is difficult to characterize precisely the geometrical features of the time reversal image given by the illumination (6.1), with coefficients (6.5). We can do it however in at least two special cases, that of well separated point reflectors (section 6.1.1), and that of strips (section 7.2).

Because the singular value decomposition is done frequency by frequency, it does not address the resolution in range. This can be improved by a separate optimization over $\widehat{\varphi}(\omega)$, of the L^2 norm of the image normalized by its maximal value. We illustrate this optimization in the next section, for a small, point-like reflector.

6.1.1 Time reversal imaging of a point reflector

For a small reflector with thickness $h \ll c_o/\omega_o$ and diameter $b \ll \lambda_o L/a$, we can approximate

$$\begin{aligned}
\widehat{\rho}_L\left(-2k, \frac{k(\mathbf{x}_s + \mathbf{x}_r)}{L}\right) &= \int_{-h/2}^{h/2} d\eta \int_{|\boldsymbol{\xi}| \leq b/2} d\boldsymbol{\xi}\, \rho(L+\eta, \boldsymbol{\xi}) \exp\left[2ik\eta - \frac{ik(\mathbf{x}_s + \mathbf{x}_r) \cdot \boldsymbol{\xi}}{L}\right] \\
&\approx \int_{-h/2}^{h/2} d\eta \int_{|\boldsymbol{\xi}| \leq b/2} d\boldsymbol{\xi}\, \rho(L+\eta, \boldsymbol{\xi}) = \widehat{\rho}_L(\vec{\mathbf{0}}).
\end{aligned} \tag{6.6}$$

We obtain that $\widehat{V}_n(\vec{\mathbf{x}}_s, \omega)$ are the singular functions of an integral operator with constant kernel $\widehat{\rho}_L(\mathbf{0})$, which we can assume is positive. This gives a single non-zero singular value

$$\sigma_1(\omega) = k^{d-1}|\mathcal{A}|\,|\alpha(L)|^2 |\widehat{\rho}_L(\mathbf{0})|, \quad n^\star(\omega) = 1, \tag{6.7}$$

for the constant singular function

$$\widehat{V}_1(\vec{\mathbf{x}}_s, \omega) = \frac{k^{(3-d)/2}}{|\alpha(L)|\,|\mathcal{A}|^{1/2}},$$

where $|A| = a^2$ in 3-D and a in 2-D. Equivalently, we have in agreement with (3.17),

$$\widehat{v}_1(\vec{\mathbf{x}}_r, \omega) = \frac{k^{(3-d)/2}}{|\alpha(L)|\,|\mathcal{A}|^{1/2}} \overline{\widehat{\mathcal{G}}_o(\vec{\mathbf{x}}_r, \vec{\mathbf{y}}^\star, \omega)}. \tag{6.8}$$

The time reversal image is

$$\begin{aligned}
\mathcal{I}^{\mathrm{TR}}(\vec{\mathbf{y}}^S; \widehat{g}) &\sim \int_{|\omega - \omega_o| \leq B/2} d\omega\, \omega^{\frac{d-3}{2}} \overline{\widehat{d}_1(\omega)} \sigma_1(\omega) e^{ik\eta^S} \int_{\mathcal{A}} d\boldsymbol{\xi}^S e^{\frac{ik\mathbf{x}_r}{L} \cdot \boldsymbol{\xi}^S} \\
&\sim \int_{|\omega - \omega_o| \leq B/2} d\omega\, \omega^{\frac{d-3}{2}} \overline{\widehat{d}_1(\omega)} \sigma_1(\omega) e^{ik\eta^S} \prod_{j=1}^{d-1} \frac{\sin\left(\frac{ka\xi_j^S}{2L}\right)}{k\xi_j^S}.
\end{aligned} \tag{6.9}$$

Moreover, recalling (6.4), we can set $\widehat{d}_1(\omega) = \widehat{\varphi}(\omega)$, i.e.,

$$\widehat{g}(\vec{\mathbf{x}}_s, \omega) = \widehat{\varphi}(\omega)\widehat{v}_1(\vec{\mathbf{x}}_s, \omega), \tag{6.10}$$

for a $\widehat{\varphi}(\omega)$ that we wish to determine.

Clearly, the peak of the image function occurs at $\vec{\mathbf{y}}^S = \vec{\mathbf{y}}^\star$, where $\eta^S = 0$ and $\boldsymbol{\xi}^S = \mathbf{0}$ and

$$\mathcal{I}^{\mathrm{TR}}(\vec{\mathbf{y}}^\star; \widehat{g}) \sim \int_{|\omega - \omega_o| \leq B/2} d\omega \, \omega^{\frac{d-3}{2}} \overline{\widehat{\varphi}(\omega)} \sigma_1(\omega). \tag{6.11}$$

Furthermore, we get from (5.28) that

$$\mathcal{O}^{\mathrm{TR}}(\widehat{\varphi}) = \frac{\displaystyle\int_{|\omega - \omega_o| \leq B/2} d\omega \, \frac{|\widehat{\varphi}(\omega)|^2 \sigma_1^2(\omega)}{\omega^2}}{\left| \displaystyle\int_{|\omega - \omega_o| \leq B/2} d\omega \, \omega^{\frac{d-3}{2}} \overline{\widehat{\varphi}(\omega)} \sigma_1(\omega) \right|^2} = \|\mathcal{J}^{\mathrm{TR}}(\cdot, \widehat{\varphi})\|^2, \quad \mathcal{J}^{\mathrm{TR}}(\vec{\mathbf{y}}^S, \widehat{\varphi}) = \frac{\mathcal{I}^{\mathrm{TR}}(\vec{\mathbf{y}}^S, \widehat{g})}{\displaystyle\max_{\vec{\mathbf{y}}^S \in \mathcal{D}} |\mathcal{I}^{\mathrm{TR}}(\vec{\mathbf{y}}^S, \widehat{g})|}. \tag{6.12}$$

We wish to minimize $\mathcal{O}^{\mathrm{TR}}(\widehat{\varphi})$ over $\widehat{\varphi}(\omega)$ normalized by

$$\int_{|\omega - \omega_o| \leq B/2} d\omega \, |\widehat{\varphi}(\omega)|^2 = 1, \quad \text{such that} \quad \int_{|\omega - \omega_o| \leq B/2} d\omega \int_{\mathcal{A}} d\mathbf{x}_s \, |\widehat{g}(\vec{\mathbf{x}}_s, \omega)|^2 = 1. \tag{6.13}$$

The result is given by the following theorem.

Theorem 1 *The minimizer of $\mathcal{O}^{TR}(\widehat{\varphi})$ over $\widehat{\varphi}(\omega) \in \mathbb{C}$, with support in the interval $[\omega_o - B/2, \omega_o + B/2]$ and with normalization (6.13) is given by*

$$\widehat{\varphi}(\omega) = \frac{C\omega^{\frac{d+1}{2}}}{\sigma_1(\omega)}, \quad \text{where} \quad C = \left[\int_{|\omega - \omega_o| \leq B/2} d\omega \, \frac{\omega^{d+1}}{\sigma_1^2(\omega)} \right]^{-1/2}, \tag{6.14}$$

up to an arbitrary phase. This gives in light of (6.7) and (6.10) the optimal illumination

$$\widehat{g}(\vec{\mathbf{x}}_s, \omega) \sim \omega^{3-d} \overline{\widehat{\mathcal{G}}_o(\vec{\mathbf{x}}_s, \vec{\mathbf{y}}^\star, \omega)}.$$

The proof follows immediately from the Euler-Lagrange equations. The phase ambiguity can be removed by restricting $\widehat{\varphi}(\omega)$ to the class of non-negative functions.

6.2 Optimal illumination for Kirchhoff migration imaging

The L^2 norm of the Kirchhoff migration image is given by (5.38) in 3-D and by (5.39) in 2-D. We seek optimal illuminations $\widehat{f}(\vec{\mathbf{x}}_s, \omega)$ in the functional space,

$$\mathcal{F} = \left\{ \widehat{f}(\vec{\mathbf{x}}_s, \omega) \geq 0, \quad \int_{|\omega - \omega_o| \leq B/2} d\omega \int_{\mathcal{A}} d\mathbf{x}_s \, \widehat{f}(\vec{\mathbf{x}}_s, \omega) = 1 \right\}, \quad \vec{\mathbf{x}}_s = (0, \mathbf{x}_s), \tag{6.15}$$

that minimize the spatial support of the image, as measured by the objective function

$$\mathcal{O}^{\mathrm{KM}}(\widehat{f}) = \|\mathcal{J}^{\mathrm{KM}}(\cdot, \widehat{f})\|^2, \quad \mathcal{J}^{\mathrm{KM}}(\vec{\mathbf{y}}^S, \widehat{f}) = \frac{\mathcal{I}^{\mathrm{KM}}(\vec{\mathbf{y}}^S, \widehat{f})}{\max\limits_{\vec{\mathbf{y}} \in \mathcal{D}} \left| \mathcal{I}^{\mathrm{KM}}(\vec{\mathbf{y}}, \widehat{f}) \right|}. \tag{6.16}$$

The location $\vec{\mathbf{y}}^M = (L + \eta^M, \boldsymbol{\xi}^M)$ of the maximum of $\mathcal{I}^{\mathrm{KM}}(\vec{\mathbf{y}}^S; \widehat{f})$ depends on the reflectivity. For example, if we let the reflectivity be the indicator function of a parallelepiped

$$\rho(L + \eta, \boldsymbol{\xi}) = \chi\left(\frac{\eta}{h}\right) \prod_{j=1}^{2} \chi\left(\frac{\xi_j}{b}\right), \quad \text{with} \ \ \chi(t) = \begin{cases} 1 & \text{if } |t| \leq 1/2, \\ 0 & \text{otherwise}, \end{cases}$$

then $\mathcal{I}^{\mathrm{KM}}(\vec{\mathbf{y}}^S; \widehat{f})$ peaks at the corners $\left(L \pm \frac{h}{2}, \pm\frac{b}{2}, \pm\frac{b}{2}\right)$. We can therefore normalize the image by its value at any corner. On the other hand, if we have a small, point-like reflector at $\vec{\mathbf{y}}^\star = (L, \mathbf{0})$, the peak of $\mathcal{I}^{\mathrm{KM}}(\vec{\mathbf{y}}^S; \widehat{f})$ is at $\vec{\mathbf{y}}^M = \vec{\mathbf{y}}^\star$. Because of the strong dependence of the peak of the image on the reflectivity $\rho(\vec{\mathbf{y}})$, we cannot write explicitly the optimal illumination $\widehat{f}(\vec{\mathbf{x}}_s, \omega)$ in the general case. But we can draw some interesting conclusions, by looking first at the case of a point reflector.

6.2.1 Kirchhoff migration imaging of a point reflector

Using the approximation (6.6) of $\widehat{\rho}_L$ in the imaging function (5.29), we obtain

$$\mathcal{I}^{\mathrm{KM}}(\vec{\mathbf{y}}^S; \widehat{f}) \sim \int_{|\omega - \omega_o| \leq B/2} d\omega \int_{\mathcal{A}} d\mathbf{x}_r \int_{\mathcal{A}} d\mathbf{x}_s \, \omega^{d-1} \, \widehat{f}(\vec{\mathbf{x}}_s, \omega) \exp\left[-2ik\eta^S + \frac{ik(\mathbf{x}_r + \mathbf{x}_s) \cdot \boldsymbol{\xi}^S}{L}\right], \tag{6.17}$$

The image peaks at $\vec{\mathbf{y}}^M = \vec{\mathbf{y}}^\star = (L, \mathbf{0})$ and its L^2 norm is given by

$$\left\|\mathcal{I}^{\mathrm{KM}}(\cdot; \widehat{f})\right\|^2 \sim \int_{|\omega - \omega_o| \leq B/2} d\omega \int_{\mathcal{A}} d\mathbf{x}_s \int_{\mathcal{A}} d\mathbf{x}'_s \, \omega^{d-1} \widehat{f}(\vec{\mathbf{x}}_s, \omega) \widehat{f}(\vec{\mathbf{x}}'_s, \omega) \prod_{j=1}^{d-1} \left(a - |(\mathbf{x}'_s - \mathbf{x}_s)_j|\right). \tag{6.18}$$

The minimizer of $\mathcal{O}^{\mathrm{KM}}(\widehat{f})$ in the functional space $\mathcal{F}$ is given by the following theorem.

Theorem 2 *The optimal illumination for Kirchhoff migration imaging of a point reflector is*

$$\widehat{f}(\vec{\mathbf{x}}_s, \omega) = \frac{1}{B} \prod_{j=1}^{2} \frac{2}{a} \left[\delta\left(\frac{a}{2} + (\mathbf{x}_s)_j\right) + \delta\left(\frac{a}{2} - (\mathbf{x}_s)_j\right)\right], \quad \vec{\mathbf{x}}_s = (0, \mathbf{x}_s), \tag{6.19}$$

in 3-D. It corresponds to illuminating the reflector with the sources at the corners of the square array and taking a flat distribution of the frequency in the bandwidth. In 2-D we have

$$\widehat{f}(\vec{\mathbf{x}}_s, \omega) = \frac{2}{aB} \left[\delta\left(\frac{a}{2} + x_s\right) + \delta\left(\frac{a}{2} - x_s\right)\right] \quad \text{for } \vec{\mathbf{x}}_s = (0, x_s) \text{ in 2-D}. \tag{6.20}$$

Proof: We begin with the Euler-Lagrange equations for the optimization,

$$\int_{\mathcal{A}} d\mathbf{x}'_s \, \widehat{f}(\vec{\mathbf{x}}'_s, \omega) \prod_{j=1}^{d-1} \left(a - |(\mathbf{x}'_s - \mathbf{x}_s)_j| \right) = C_1 + \frac{C_2}{\omega^{d-1}}, \qquad \vec{\mathbf{x}}'_s = (0, \mathbf{x}'_s), \tag{6.21}$$

where C_1 and C_2 are constants with respect to $\mathbf{x}_s$

$$C_1 = \frac{\int_{|\omega-\omega_o|\le B/2} d\omega \int_{\mathcal{A}} d\mathbf{x}_s \int_{\mathcal{A}} d\mathbf{x}'_s \omega^{d-1} \widehat{f}(\vec{\mathbf{x}}_s, \omega) \widehat{f}(\vec{\mathbf{x}}'_s, \omega)] \prod_{j=1}^{d-1} \left(a - |(\mathbf{x}'_s - \mathbf{x}_s)_j| \right)}{\int_{|\omega-\omega_o|\le B/2} d\omega \int_{\mathcal{A}} d\mathbf{x}_s \, \omega^{d-1} \widehat{f}(\mathbf{x}_s, \omega)}$$

$$C_2 = \gamma \left\{ \int_{|\omega-\omega_o|\le B/2} d\omega \int_{\mathcal{A}} d\mathbf{x}_s \, \omega^{d-1} \widehat{f}(\vec{\mathbf{x}}_s, \omega) \right\}^2$$

and γ is the Lagrange multiplier for the normalization constraint on $\widehat{f}$.

Now we note that in order to find the spatial distribution of the sources in the optimal illumination, we must solve equations of the form

$$\int_{-a/2}^{a/2} dx'_s \, (a - |x_s - x'_s|) w(x'_s) = C, \tag{6.22}$$

for an arbitrary constant C and for $w(x)$ supported in $[-a/2, a/2]$.

Lemma 1 *Equation (6.22) has the unique solution*

$$w(x_s) = \frac{2C}{a} \left[\delta \left(\frac{a}{2} + x_s \right) + \delta \left(\frac{a}{2} - x_s \right) \right]. \tag{6.23}$$

Once we prove Lemma 1, the proof of Theorem 2 follows immediately from the Euler-Lagrange equations (6.21) and the normalization condition on $\widehat{f}(\vec{\mathbf{x}}_s, \omega)$. Note in particular that due to the homogeneity of degree zero of the objective function $\mathcal{O}^{\mathrm{KM}}(\widehat{f})$, and the diagonal form of the kernels of the integral operators in ω, the Lagrange multiplier γ vanishes. This is why $\widehat{f}$ is constant in the bandwidth.

Proof of Lemma 1: First, it is easy to check that (6.23) satisfies equation (6.22). Thus, all we have to do is to show that the integral operator in (6.22) has a trivial null space. Suppose that there exists a function $\vartheta(x_s)$ supported in $[-a/2, a/2]$, such that

$$\int_{-a/2}^{a/2} dx'_s (a - |x_s - x'_s|) \vartheta(x'_s) = 0. \tag{6.24}$$

This equation is the convolution of ϑ with function

$$F(x) = \begin{cases} a - |x| & \text{if } |x| \le a, \\ 0 & \text{otherwise.} \end{cases} \tag{6.25}$$

Take then the Fourier transform in (6.24) and obtain that $\widehat{F}(\beta)\widehat{\vartheta}(\beta) = 0$. Now,

$$\widehat{F}(\beta) = \int_{-a}^{a} dx\,(a - |x|)e^{-i\beta x} = \frac{4\sin^2\left(\frac{\beta a}{2}\right)}{\beta^2}, \tag{6.26}$$

so $\widehat{\vartheta}(\beta)$ must vanish almost everywhere on the real line, except for the discrete locations $\beta_n = 2n\pi/a$, for $n = 0, \pm 1, \dots$. However, $\widehat{\vartheta}(\beta)$ is an analytic function (since $\vartheta(x)$ has compact support), which means that it must be identically zero. $\square$

Remark: In the numerical simulations of section 4 we optimize the 2-D objective function over

$$\widehat{\varphi}(\vec{\mathbf{x}}_s, \omega) = \omega\widehat{f}(\vec{\mathbf{x}}_s, \omega), \tag{6.27}$$

instead of $\widehat{f}(\vec{\mathbf{x}}_s, \omega)$ and we consider the normalization

$$\int_{|\omega-\omega_o|\leq B/2} d\omega \int_{-a/2}^{a/2} dx_s\,\widehat{\varphi}(x_s, \omega) = 1,$$

which keeps the peak of the image at a constant value (see (6.17)). With this choice we have

$$\widehat{\varphi}(\vec{\mathbf{x}}_s, \omega) = \frac{2\omega}{a\omega_o B}\left[\delta\left(\frac{a}{2} + x_s\right) + \delta\left(\frac{a}{2} - x_s\right)\right], \quad \vec{\mathbf{x}}_s = (0, x_s).$$

This coincides with (6.20), except for the normalization constant. Moreover, it agrees with the numerical results obtained in section 4.

Remark: Theorem 2 shows that in the case of a point scatterer and at high SNR, the optimal illumination $\widehat{f}(\vec{\mathbf{x}}_s, \omega)$ is of separable form and that it favors edge illumination from the array. This is due to the form of the kernel in (5.39),

$$\int_{-\frac{a}{2}+\frac{|x'_s-x_s|}{2}}^{\frac{a}{2}-\frac{|x'_s-x_s|}{2}} d\bar{x}\,\left|k^2\widehat{\rho}_L\left(-2k, \frac{k}{L}\left(\bar{x} + \frac{x_s + x'_s}{2}\right)\right)\right|^2 \approx \widehat{\rho}_L(\vec{\mathbf{0}})\left(a - |x_s - x'_s|\right),$$

which is smallest when x_s and x'_s are at the opposite ends of the array. The kernel has a similar behavior for general reflectivity functions and this is why we observe that optimal illuminations are from the edge of the array. We illustrate this in section 8 for the case of strip-like reflectors.

7 Time reversal imaging of strips

We already discussed in section 5.4.1 the SVD of the response matrix $\widehat{\Pi}_F(\omega)$ in the Fraunhofer diffraction regime and for a general reflectivity ρ. We also wrote in section 5.4.2 the mathematical expression of the time reversal imaging function, using the SVD. We formulated the variational principle for optimal illumination in section 6.1, and we obtained an explicit solution for isolated point reflectors, in section 6.1.1. Now we analyze the 2-D problem of imaging a strip, with reflectivity

$$\rho(L + \eta, \xi) = \rho_L(\eta)\chi(\xi). \tag{7.1}$$

Here $\chi(\xi)$ is the indicator function of the interval $[-b/2, b/2]$, and $\rho_L(\eta)$ is some bounded function in $L^1(\mathbb{R})$, with support in $[-h/2, h/2]$ (as in section 5.2). The analysis extends easily to 3-D, for reflectivities of the form

$$\rho(L + \eta, \boldsymbol{\xi}) = \rho_L(\eta)\chi_{\mathcal{B}}(\boldsymbol{\xi}),$$

with $\chi_{\mathcal{B}}$ being the indicator function of the square $\mathcal{B} = [-b/2, b/2] \times [-b/2, b/2]$. The case of arbitrarily shaped cross-sections $\mathcal{B}$ of the reflectors is left for future studies.

7.1 Spectral analysis of the response matrix for a strip

Let us recall from section 6.1 that the singular functions are of the form

$$\widehat{v}(\vec{\mathbf{x}}_s, \omega) = \overline{\widehat{\mathcal{G}}_o(\vec{\mathbf{x}}_s, \vec{\mathbf{y}}^\star, \omega)}\widehat{V}(x_s, \omega). \tag{7.2}$$

Here $\widehat{V}(x_s, \omega)$ are singular functions of the integral operator with kernel $\widehat{\rho}_L\left(-2k, \frac{k(x_r+x_s)}{L}\right)$, and $\vec{\mathbf{x}}_s = (0, x_s)$ are points in the array, with x_s varying continuously in $[-a/2, a/2]$. We droped the vector notation in the argument of $\widehat{V}$ and neglect temporarily the index of the singular functions.

We note that

$$\widehat{\chi}\left[\frac{k(x_r + x_s)}{L}\right] = \int_{-b/2}^{b/2} d\xi\, e^{-i\frac{k(x_r+x_s)\xi}{L}} = \frac{2\pi L}{k}\frac{\sin\left(\frac{kb(x_r+x_s)}{2L}\right)}{\pi(x_r + x_s)}, \tag{7.3}$$

and we suppose for simplicity that

$$\widehat{\rho}_L(-2k) = \int d\eta\, \rho_L(\eta)e^{2ik\eta} = |\widehat{\rho}_L(-2k_o)| \tag{7.4}$$

is constant and positive in the bandwidth. We obtain

$$\int_{-a/2}^{a/2} dx_s\, \frac{\sin\left[C(\omega)\left(\frac{2x_r}{a} + \frac{2x_s}{a}\right)\right]}{\pi(x_r + x_s)}\widehat{V}(x_s, \omega) = \mu(\omega)\overline{\widehat{V}(x_r, \omega)}, \tag{7.5}$$

$$\|\widehat{V}(\cdot, \omega)\| = |\alpha(L)|^{-1},$$

with

$$\mu(\omega) = \frac{\sigma(\omega)}{2\pi L|\alpha(L)|^2|\widehat{\rho}_L(-2k_o)|}, \tag{7.6}$$

and with

$$C(\omega) = \frac{kab}{4L}, \tag{7.7}$$

assumed positive in the bandwidth.

7.1.1 A canonical problem for the prolate spheroidal wave functions

To solve (7.5), we recall the integral equation analyzed by Landau, Pollack and Slepian [26, 21, 25],

$$\int_{-1}^{1} d\zeta' \frac{\sin\left[C\left(\zeta - \zeta'\right)\right]}{\pi(\zeta - \zeta')} \psi(\zeta, C) = \nu(C)\, \psi(\zeta, C)\,, \quad \zeta \in [-1, 1]\,, \quad C > 0. \tag{7.8}$$

Note that the integral operator in (7.8) has a symmetric and positive definite kernel. Therefore, it has a discrete spectrum with non-negative eigenvalues [17] $\nu_0(C) \geq \nu_1(C) \geq \ldots \geq 0$, that accumulate at zero ($\lim_{n\to\infty} \nu_n(C) = 0$). The eigenfunctions are the prolate spheroidal wave functions $\psi_n(\zeta, C)$. They have many interesting properties [26, 21, 25], including the following.

Property 1 *The prolate spheroidal wave functions form a complete set in $L^2[-1, 1]$. They are normalized to have unit energy on the the real line and they satisfy the orthogonality relations*

$$\int_{-1}^{1} d\zeta\, \psi_n(\zeta; C)\, \psi_m(\zeta; C) = \nu_n(C)\, \delta_{n,m}, \tag{7.9}$$

$$\int_{-\infty}^{\infty} d\zeta\, \psi_n(\zeta; C)\, \psi_m(\zeta; C) = \delta_{n,m}, \quad for\ n, m = 0, 1, \ldots \tag{7.10}$$

Property 2 *The prolate spheroidal wave functions $\psi_n(\zeta, C)$ are even functions of ζ for even n and odd otherwise,*

$$\psi_n(-\zeta, C) = (-1)^n \psi_n(\zeta, C)\,, \quad n = 0, 1, \ldots. \tag{7.11}$$

Property 3 *The eigenvalues $\nu_n(C)$ stay close to 1 for small n and then, they plunge to 0 near the threshold value $n^\star = \left\lfloor \frac{2C}{\pi} \right\rfloor$, where $\lfloor \cdot \rfloor$ denotes the integer part.*

Property 4 *The functions ψ_n are preserved by the Fourier transform, up to a coordinate change*

$$\psi_n(\zeta; C) = \frac{1}{\gamma_n(C)} \int_{-\frac{C}{2\pi}}^{\frac{C}{2\pi}} dt\, \psi_n\left(\frac{2\pi t}{C}; C\right) e^{2\pi i \zeta t}, \quad \gamma_n^2(C) = \frac{(-1)^n}{2\pi} C \nu_n(C)\,. \tag{7.12}$$

7.1.2 The singular value decomposition with the prolate spheroidal wave functions

Now let us change the variable of integration in (7.5) from x_s to $-x_s$ to obtain

$$\int_{-a/2}^{a/2} dx_s \frac{\sin\left[C(\omega)\left(\frac{2x_r}{a} - \frac{2x_s}{a}\right)\right]}{\pi(x_r - x_s)} \widehat{V}(-x_s, \omega) = \mu(\omega) \overline{\widehat{V}(x_r, \omega)}. \tag{7.13}$$

Using Properties 1 and 2 we find that this equation is solvable for the discrete eigenvalues

$$\mu_n(\omega) = \nu_n(C(\omega))\,, \quad n = 0, 1, \ldots \tag{7.14}$$

The singular functions in (7.13) are

$$\widehat{V}_n(x_s, \omega) = \sqrt{(-1)^n}\, K_n \psi_n\left(\frac{2x_s}{a}, C(\omega)\right)\,, \quad n = 0, 1, \ldots$$

40

with normalization constants $K_n > 0$ determined by

$$\|\widehat{V}_n(\cdot, \omega)\|^2 = \frac{aK_n^2}{2}\nu_n(C(\omega)) = \frac{1}{|\alpha(L)|^2}.$$

Note that $\widehat{V}_n(x_s, \omega)$ satisfy the identity

$$\widehat{V}_n(-x_s, \omega) = (-1)^n \widehat{V}_n(x_s, \omega) = \overline{\widehat{V}_n(x_s, \omega)},$$

for all indices $n \geq 0$. We now gather all the results and state the SVD for the strip:

Theorem 3 *The singular value decomposition of the integral operator with kernel* $\widehat{\Pi}_F(\vec{\mathbf{x}}_r, \vec{\mathbf{x}}_s, \omega)$ *is*

$$\int_{-a/2}^{a/2} dx_s\, \widehat{\Pi}_F(\vec{\mathbf{x}}_r, \vec{\mathbf{x}}_s, \omega)\widehat{v}_n(\vec{\mathbf{x}}_s, \omega) = \sigma_n(\omega)\overline{\widehat{v}(\vec{\mathbf{x}}_r, \omega)}, \tag{7.15}$$

with singular values

$$\sigma_n(\omega) = 2\pi L|\alpha(L)|^2|\widehat{\rho}_L(-2k_o)|\nu_n(C(\omega)), \tag{7.16}$$

for $n = 0, 1, \ldots$. The singular functions are

$$\widehat{v}_n(\vec{\mathbf{x}}_s, \omega) = \frac{k^{1/2}}{|\alpha(L)|}\sqrt{\frac{2(-1)^n}{a\nu_n(C(\omega))}}\overline{\widehat{\mathcal{G}}_o(\vec{\mathbf{x}}_s, \vec{\mathbf{y}}^\star, \omega)}\,\psi_n\left(\frac{2x_s}{a}; C(\omega)\right), \tag{7.17}$$

for $\vec{\mathbf{x}}_s = (0, x_s)$. They form a complete, orthonormal set in $L^2[-a/2, a/2]$. The singular values $\sigma_n(\omega)$ are negligible for indices n above the threshold value

$$n^\star(\omega) = \left\lfloor\frac{2C(\omega)}{\pi}\right\rfloor = \left\lfloor\frac{b}{\lambda L/a}\right\rfloor, \tag{7.18}$$

given by the ratio of the size b of the strip and the spot size $\lambda L/a$. This means that any illumination in the null space

$$\mathcal{N}(\widehat{\Pi}_F) = span\left\{\widehat{v}_n(\vec{\mathbf{x}}_s, \omega)\right\}_{n > n^\star(\omega)} \tag{7.19}$$

returns no echoes at the array.

7.1.3   The support of the singular functions and their Fourier transform

The canonical problem (7.8) was solved by Landau, Pollack and Slepian [26, 21, 25] in their study of simultaneous concentration in finite intervals of signals and their Fourier transforms.

Consider the restriction operator $\mathcal{R}_a : L^2(\mathbb{R}) \to L^2(\mathbb{R})$ to the interval $[-a/2, a/2]$,

$$\mathcal{R}_a u(x) = \begin{cases} u(x) & \text{if } x \in [-a/2, a/2], \\ 0 & \text{otherwise.} \end{cases}$$

Let also $\widehat{\mathcal{R}}_{b,\omega}$ be the operator that restricts the support of the Fourier transform of a function

$$\widehat{\mathcal{R}}_{b,\omega} u(x) = \frac{k}{2\pi L}\int_{-b/2}^{b/2} d\xi\, \widehat{u}\left(\frac{k\xi}{L}\right)e^{\frac{ikx\xi}{L}},$$

for a given frequency ω. We have

$$
\begin{aligned}
\mathcal{R}_a \widehat{\mathcal{R}}_{b,\omega} \mathcal{R}_a u(x_r) &= \frac{k}{2\pi L} \int_{-b/2}^{b/2} d\xi \, e^{\frac{ikx_r\xi}{L}} \int_{-a/2}^{a/2} dx_s \, u(x_s) e^{-\frac{ikx_s\xi}{L}} \\
&= \int_{-a/2}^{a/2} dx_s \, \frac{\sin\left[C(\omega)\left(\frac{2x_r}{a} - \frac{2x_s}{a}\right) \right]}{\pi(x_r - x_s)} u(x_s), \quad x_r \in [-a/2, a/2]. \quad (7.20)
\end{aligned}
$$

Now, observe by comparison with (7.8) that ν_n and ψ_n are the eigenvalues and eigenfunctions of the symmetric operator $\mathcal{R}_a \widehat{\mathcal{R}}_{b,\omega} \mathcal{R}_a$. This means that for $n \leq n^\star(\omega)$, $\widehat{V}_n(x,\omega)$ are concentrated in the interval $|x| \leq a/2$ while their Fourier transforms

$$
\int_{-a/2}^{a/2} dx \, \widehat{V}_n(x,\omega) e^{-\frac{ikx\xi}{L}}
$$

are concentrated in the interval $|\xi| \leq b/2$. This plays a key role in our imaging study.

7.2 Time reversal imaging of strips

We consider as in section 6.1 illuminations

$$
\widehat{g}(\vec{\mathbf{x}}_s, \omega) = \sum_{n=0}^{n^\star(\omega)} \widehat{d}_n(\omega) \widehat{v}_n(x_s, \omega), \quad (7.21)
$$

for coefficients $\widehat{d}_n(\omega)$ to be determined, subject to the normalization condition

$$
|\widehat{\varphi}(\omega)|^2 = \int_{-a/2}^{a/2} dx_s \, |\widehat{g}(x_s, \omega)|^2 = \sum_{n=0}^{n^\star(\omega)} |\widehat{d}_n(\omega)|^2. \quad (7.22)
$$

Here $\widehat{\varphi}(\omega)$ may be given in advance or we can select it optimally, as explained in section 6. The time reversal imaging function is given by (recall (5.26))

$$
\mathcal{I}^{\mathrm{TR}}(\vec{\mathbf{y}}^S; \widehat{g}) \sim \int_{|\omega - \omega_o| \leq B/2} d\omega \sum_{n=0}^{n^\star(\omega)} \overline{\widehat{d}_n(\omega)} \sigma_n(\omega) \, \omega^{-\frac{1}{2}} \int_{-a/2}^{a/2} dx_r \, \widehat{\mathcal{G}}_o(\vec{\mathbf{x}}_r, \vec{\mathbf{y}}^S, \omega) \widehat{v}_n(\vec{\mathbf{x}}_r, \omega). \quad (7.23)
$$

Theorem 3 and definition (5.13) of $\widehat{\mathcal{G}}_o$ allow us to rewrite (7.23) as

$$
\begin{aligned}
\mathcal{I}^{\mathrm{TR}}(\vec{\mathbf{y}}^S; \widehat{g}) &\sim \int_{|\omega - \omega_o| \leq B/2} d\omega \, e^{ik\eta^S} \sum_{n=0}^{n^\star(\omega)} \frac{\overline{\widehat{d}_n(\omega)}}{\omega} \sqrt{(-1)^n \nu_n(C(\omega))} \int_{-a/2}^{a/2} dx_r \, \psi_n\left(\frac{2x_r}{a}, C(\omega)\right) e^{-\frac{ikx_r\xi^S}{L}} \\
&\sim \int_{|\omega - \omega_o| \leq B/2} d\omega \, e^{ik\eta^S} \sum_{n=0}^{n^\star(\omega)} \frac{\overline{\widehat{d}_n(\omega)}}{\omega^{3/2}} \nu_n(C(\omega)) \, \psi_n\left(\frac{2\xi^S}{b}, C(\omega)\right). \quad (7.24)
\end{aligned}
$$

Here we used Property 4

$$
\begin{aligned}
\int_{-a/2}^{a/2} dx_r \, \psi_n\left(\frac{2x_r}{a}, C(\omega)\right) e^{-\frac{ikx_r\xi^S}{L}} &= \frac{\pi a}{C(\omega)} \int_{-\frac{C(\omega)}{2\pi}}^{\frac{C(\omega)}{2\pi}} dt \, \psi_n\left(\frac{2\pi t}{C(\omega)}; C(\omega)\right) e^{-2\pi it \frac{2\xi^S}{b}} \\
&= \frac{\pi a \overline{\gamma_n(C(\omega))}}{C(\omega)} \psi_n\left(\frac{2\xi^S}{b}, C(\omega)\right), \quad (7.25)
\end{aligned}
$$

42

and

$$\sqrt{(-1)^n \nu_n(C(\omega))} \, \frac{\overline{\gamma_n(C(\omega))}}{C(\omega)} = \frac{\nu_n(C(\omega))}{\sqrt{2\pi C(\omega)}} \sim \frac{\nu_n(C(\omega))}{\omega^{1/2}}.$$

We study next how different choices of the coefficients $\widehat{d}_n(\omega)$ affect the time reversal image.

7.3   Selective illumination and imaging of the strip

The time reversal image (7.24) is a linear superposition of the prolate spheroidal wave functions, adapted to the support $[-b/2, b/2]$ of the reflector. Since $\left\{\psi_n\left(2\xi^S/b; C(\omega)\right)\right\}_{n \geq 0}$ are complete in $L^2[-b/2, b/2]$, we can get a good approximation (in the L^2 sense) of the reflectivity by $\mathcal{I}^{\mathrm{TR}}(\mathbf{y}^S; \widehat{g})$, for an appropriate choice of the coefficients $\widehat{d}_n(\omega)$ (i.e. of the illumination $\widehat{g}(\mathbf{x}_s, \omega)$). A more interesting question is how to choose the coefficients to focus selectively the illumination on various parts of the strip? To answer it, we look next at the behavior of the prolate spheroidal functions, for various frequencies and indices below the threshold $n^\star(\omega)$.
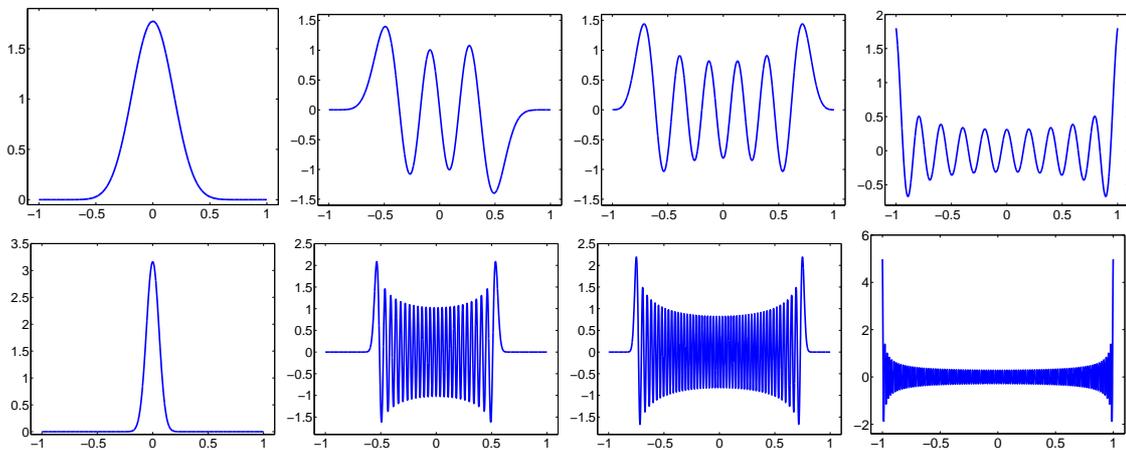
Figure 12: The prolate spheroidal wave functions $\psi_n(\zeta, C(\omega))$ plotted for $\zeta \in [-1, 1]$. Top: $C(\omega) = 10\pi$. Bottom: $C(\omega) = 100\pi$. From left to right: $n = 0$, $\left\lfloor \frac{n^\star(\omega)}{4} \right\rfloor$, $\left\lfloor \frac{n^\star(\omega)}{2} \right\rfloor$, and $n^\star(\omega)$.

We plot in Figure 12 the functions $\psi_n\left(\zeta, C(\omega)\right)$ for $C(\omega)$ equal to 10π and 100π. This corresponds to $b = 20\lambda L/a$ and $b = 200\lambda L/a$, respectively. We observe that for the index $n = 0$, the prolate spheroidal wave functions are non-negative and concentrated near the origin. The higher the frequency is the better the spatial concentration, but the L^2 norm remains the same

$$\int_{-1}^{1} d\zeta \, \psi_0^2(\zeta, C(\omega)) = \nu_0(\omega) = 1. \tag{7.26}$$

As the index n increases, $\psi_n\left(\zeta, C(\omega)\right)$ becomes oscillatory and its peaks move toward the ends of the interval $[-1, 1]$. This is evident from the plots in Figure 12, for n equal to a quarter, a half

and the entire threshold $n^\star(\omega)$, respectively. For index $n > n^\star(\omega)$, the support of ψ_n is essentially outside the interval $[-1, 1]$, so that

$$\int_{-1}^{1} d\zeta\, \psi_n^2(\zeta, C(\omega)) = \nu_n(\omega) \approx 0 \quad \text{for } n > n^\star(\omega). \tag{7.27}$$

Now we can conclude from (7.24) and Figure 12 that we can manipulate the coefficients $\widehat{d}_n(\omega)$ in order to focus selectively on different parts of the strip. For example, if we set $\widehat{d}_n(\omega) \sim \delta_{n0}$, we illuminate the center of the strip. To illuminate toward the ends of the strip, we set $\widehat{d}_n(\omega) \sim \delta_{nm}$, for m near or at the threshold. At a fixed frequency the image is oscillatory, as in Figure 12. However, the oscillations disappear when we integrate over the bandwidth and we get a nice focus on the desired part of the strip. This is shown in Figure 13, where we integrate over the frequencies corresponding to $C(\omega) \in [50\pi, 100\pi]$. Recall from Property 2 that the prolate spheroidal wave functions $\psi_n(\zeta, C(\omega))$ are even for even indices n and odd otherwise. We obtain symmetric results in Figure 13 by considering only the even indices n in the integral. When we include the odd indices as well, we can focus selectively on one end of the interval or the other, as we show in Figure 14. This is done by simply changing the sign of the coefficients $\widehat{d}_n(\omega)$ for odd and even indices.
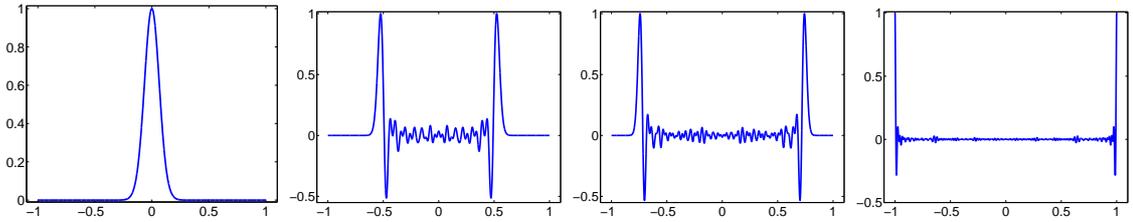
Figure 13: The integral of $\psi_n(\zeta, C(\omega))$ over $C(\omega) \in [50\pi, 100\pi]$ (i.e., $\lambda L/a \in [b/200, b/100]$). We normalize by the maximum value. From left to right: $n = 0$, $\left\lfloor \frac{n^\star(\omega)}{4} \right\rfloor$, $\left\lfloor \frac{n^\star(\omega)}{2} \right\rfloor$, and $n^\star(\omega)$.
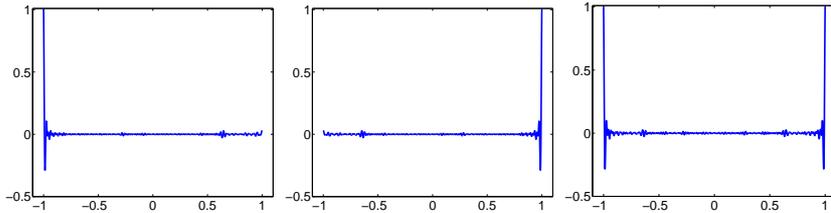
Figure 14: Selective edge illumination with $\psi_{n^\star}(\zeta, C(\omega))$ and $C(\omega) \in [50\pi, 100\pi]$.

7.4 Time reversal imaging with edge illumination

The optimal illumination criterion stated as the minimization of the L^2 norm of the time reversal image, for waveforms (7.21) and constraints (7.22), gives edge illuminations of the strip.

44

Indeed, from Theorem 3 and (5.28), the L^2 norm of the time reversal image given by

$$\|\mathcal{I}^{\mathrm{TR}}(\cdot,\widehat{g})\|^2 \quad \sim \quad \int_{|\omega-\omega_o|\leq B/2} d\omega \sum_{n=0}^{n^\star(\omega)} \nu_n^2\left(C(\omega)\right) \frac{|\widehat{d}_n(\omega)|^2}{\omega^3} \tag{7.28}$$

and we can minimize it by choosing $\widehat{d}_n(\omega) = \omega^{\frac{3}{2}}\widehat{\varphi}(\omega)\delta_{nn^\star(\omega)}$, because the eigenvalues $\nu_n\left(C(\omega)\right)$ are smallest near the threshold $n^\star(\omega)$.

The resulting illumination $\widehat{g}(x_s,\omega) = \omega^{\frac{3}{2}}\widehat{\varphi}(\omega)\widehat{v}_{n^\star(\omega)}$ is

$$\widehat{g}(x_s,\omega) \quad \sim \quad \widehat{\varphi}(\omega)\omega^2 \sqrt{\frac{(-1)^{n^\star(\omega)}}{\nu_n(C(\omega))}} \overline{\widehat{\mathcal{G}}_o(\vec{\mathbf{x}}_s,\vec{\mathbf{y}}^\star,\omega)} \, \psi_{n^\star(\omega)}\left(\frac{2x_s}{a};C(\omega)\right), \tag{7.29}$$

and it uses mostly the edges of the array, where $\psi_{n^\star(\omega)}\left(\frac{2x_s}{a};C(\omega)\right)$ is peaked. When we integrate over the frequencies, we get time domain profiles that are similar to the plots in Figure 14. These edge illuminations produce time reversal images

$$\mathcal{I}^{\mathrm{TR}}(\vec{\mathbf{y}}^S;\widehat{g}) \sim \int_{|\omega-\omega_o|\leq B/2} d\omega \, \widehat{\varphi}(\omega) e^{ik\eta^S} \nu_{n^\star(\omega)}(C(\omega)) \, \psi_{n^\star(\omega)}\left(\frac{2\xi^S}{b},C(\omega)\right), \tag{7.30}$$

that emphasize the edges of the strip (see Figure 12 and 14).

8 Kirchhoff migration imaging of strips

We begin the analysis of the Kirchhoff migration function for the strip by expanding the Fourier coefficients of the reflectivity in terms of the prolate spheroidal wave functions. We recall that

$$\widehat{\rho}_L\left(-2k,\frac{k(x_r+x_s)}{L}\right) \quad = \quad \frac{\pi b|\widehat{\rho}_L(-2k_o)|}{C(\omega)} \frac{\sin\left[C(\omega)\left(\frac{2x_r}{a}+\frac{2x_s}{a}\right)\right]}{\pi\left(\frac{2x_r}{a}+\frac{2x_s}{a}\right)} \tag{8.31}$$

and use the spectral representation of the kernel in (7.8),

$$\sum_{n=0}^{\infty} \nu_n(C(\omega))\,\psi_n(\zeta,C(\omega))\,\psi_n(\zeta',C(\omega)) = \begin{cases} \frac{\sin[C(\omega)(\zeta-\zeta')]}{\pi(\zeta-\zeta')} & \text{for } \zeta,\zeta'\in[-1,1], \\ 0 & \text{otherwise,} \end{cases} \tag{8.32}$$

to get

$$\frac{\sin\left[C(\omega)\left(\frac{2x_r}{a}+\frac{2x_s}{a}\right)\right]}{\pi\left(\frac{2x_r}{a}+\frac{2x_s}{a}\right)} \quad \approx \quad \sum_{n=0}^{n^\star(\omega)} (-1)^n \nu_n(C(\omega))\,\psi_n\left(\frac{2x_r}{a},C(\omega)\right)\psi_n\left(\frac{2x_s}{a},C(\omega)\right). \tag{8.33}$$

Here we used Property 2 and we truncated the sum to $n^\star(\omega)$, because $\nu_n(C(\omega))\approx 0$ for $n > n^\star(\omega)$. Substituting (8.33) in (5.29), we have

$$\mathcal{I}^{\mathrm{KM}}(\vec{\mathbf{y}}^S;\widehat{f}) \sim \int_{|\omega-\omega_o|\leq B/2} d\omega e^{-2ik\eta^S} \sum_{n=0}^{n^\star(\omega)} (-1)^n \nu_n(C(\omega)) \int_{-a/2}^{a/2} dx_s \widehat{f}(\vec{\mathbf{x}}_s;\omega)\psi_n\left(\frac{2x_s}{a};C(\omega)\right)$$

$$\exp\left(\frac{ikx_s\xi^S}{L}\right) \int_{-a/2}^{a/2} dx_r \psi_n\left(\frac{2x_r}{a};C(\omega)\right) e^{\frac{ikx_r\xi^S}{L}},$$

45

and with the Fourier transform formula (7.25), we get

$$\mathcal{I}^{\mathrm{KM}}(\vec{\mathbf{y}}^S; \widehat{f}) \sim \int_{|\omega-\omega_o|\le B/2} d\omega\, e^{-2ik\eta^S} \sum_{n=0}^{n^\star(\omega)} \frac{(-1)^n}{\omega} \nu_n(C(\omega))\, \gamma_n(C(\omega))\, \psi_n\!\left(\frac{2\xi^S}{b}; C(\omega)\right)$$

$$\int_{-a/2}^{a/2} dx_s \widehat{f}(\vec{\mathbf{x}}_s; \omega)\psi_n\!\left(\frac{2x_s}{a}; C(\omega)\right) e^{\frac{ikx_s\xi^S}{L}}. \qquad (8.34)$$

Remark: Equations (8.34) and (7.24) say that, at each frequency ω in the bandwidth, both the Kirchhoff migration and time reversal images are given by a superposition of the prolate spheroidal wave functions $\psi_n\!\left(\frac{2\xi^S}{b}; C(\omega)\right)$. The difference between the two imaging functions lies in the coefficients multiplying $\psi_n\!\left(\frac{2\xi^S}{b}; C(\omega)\right)$. In time reversal, these coefficients are constant with respect to $\vec{\mathbf{y}}^S$ and we can manipulate them easily (analytically) to focus the image selectively on different parts of the strip. In Kirchhoff migration, the coefficients are a multiple of

$$\int_{-a/2}^{a/2} dx_s \widehat{f}(\vec{\mathbf{x}}_s; \omega)\psi_n\!\left(\frac{2x_s}{a}; C(\omega)\right) e^{\frac{ikx_s\xi^S}{L}},$$

and they depend on ξ^S. This makes the Kirchhoff migration focusing properties quite different than those of time reversal.

We have seen in section 7.4 that we can use the variational principle that minimizes the L^2 norm of the time reversal image over the illuminations $\widehat{g}(\vec{\mathbf{x}}_s, \omega)$, to achieve focusing on the ends of the strip. The optimal waveforms favor edge illuminations from the array. We show next that this holds for the Kirchhoff migration imaging function as well.

8.1 Variational principle for edge illumination of strips

We begin our study of the variational problem of minimizing the L^2 norm of the image $\mathcal{I}^{\mathrm{KM}}(\vec{\mathbf{y}}^S; \widehat{f})$ over the illuminations $\widehat{f}$, with a few simplifying assumptions. First, we suppose that we know the range L of the strip and we concentrate on the cross-range resolution. This can be done with a single frequency ω in the bandwidth. Second, we look for real valued illuminations $\widehat{f}$ that are in the function space $L^2[-a/2, a/2]$, instead of the larger, more natural space $L^1[-a/2, a/2]$. This simplifies our computation because it allows us to write $\widehat{f}$ as the superposition

$$\widehat{f}(\vec{\mathbf{x}}_s, \omega) \approx \sum_{m=0}^{n^\star(\omega)} \widehat{d}_m(\omega)\psi_m\!\left(\frac{2x_s}{a}; C(\omega)\right), \qquad (8.35)$$

for coefficients $\left\{\widehat{d}_m(\omega)\right\}$ to be determined.
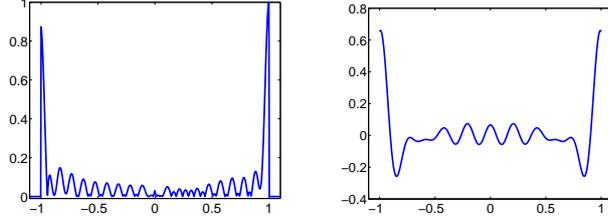
Figure 15: Left: the minimimum L^2 norm image normalized by its maximum, ploted at the correct range L, as a function of cross-range. Right: The illumination $\widehat{f}(\vec{\mathbf{x}}_s, \omega)$ that gives this image. Here $C(\omega) = 10\pi$, so that $n^\star(\omega) = 20$.

The image at search points $\vec{\mathbf{y}}^S = (L, \xi^S)$ and fixed frequency ω is (recall (8.34))

$$\mathcal{I}^{\mathrm{KM}}\left((L, \xi^S); \widehat{f}(\cdot, \omega)\right) \sim \sum_{n=0}^{n^\star(\omega)} \frac{(-1)^n}{\omega} \nu_n(C(\omega))\, \gamma_n(C(\omega))\, \psi_n\left(\frac{2\xi^S}{b}; C(\omega)\right) \sum_{m=1}^{n^\star(\omega)} \widehat{d}_m(\omega)$$

$$\int_{-a/2}^{a/2} dx_s \psi_m\left(\frac{2x_s}{a}; C(\omega)\right) \psi_n\left(\frac{2x_s}{a}; C(\omega)\right) e^{\frac{ikx_s\xi^S}{L}}. \qquad (8.36)$$

We find the optimal illumination $\widehat{f}$ by minimizing numerically the L^2 norm of the image (8.36) normalized by its maximum, over all possible choices of the coefficients $\widehat{d}_m(\omega)$, normalized by

$$\|\widehat{f}(\cdot, \omega)\|^2 \approx \sum_{m=0}^{n^\star(\omega)} |\widehat{d}_m(\omega)|^2 = 1. \qquad (8.37)$$

Note that $\widehat{d}_n(\omega) \in \mathbb{R}$ since we seek real valued illuminations $\widehat{f}(\vec{\mathbf{x}}_s, \omega)$. Ideally, we would also like $\widehat{f}(\vec{\mathbf{x}}_s, \omega)$ to be nonnegative, but we relax here this constraint in order to simplify the optimization.

We show in Figure 15 the optimal illumination $\widehat{f}(\vec{\mathbf{x}}_s, \omega)$ and the resulting image, for $C(\omega) = 10\pi$ or, equivalently, $n^\star(\omega) = 20$. We note that the result is an edge illumination from the array, that gives an image focused at the ends of the strip. The focusing becomes tighter at higher frequencies, but then $n^\star(\omega)$ is large and the optimization can be prohibitively expensive. In such cases, we could use a more efficient parametrization of $\widehat{f}(\vec{\mathbf{x}}_s, \omega)$, that takes flat illuminations over segments of the array, as we have done in the numerical simulations of section 4.

9   Linearized least squares imaging of strips

In this section we study the linearized least squares formulation of the inverse problem for a strip. We consider a fixed frequency ω illumination from a single source at x_s. However, we do more than Kirchhoff migration, because we compute the image as a regularized solution of the normal equations, that is we invert the normal operator. The solution is given explicitly in terms of the prolate spheroidal wave functions.

Since we fixed the frequency, let us suppose that we know the range L of the strip-like reflector. This could be determined with some other method, such as travel time estimation. Now let $\mathcal{M}_{\omega,x_s}$ be the forward operator given by the Born approximation (2.8), in the Fraunhofer diffraction regime. This operator takes the indicator function $\chi(\xi)$ of the strip and maps it to the data

$$\widehat{\Pi}(\vec{\mathbf{x}}_r, \vec{\mathbf{x}}_s, \omega) \approx [\mathcal{M}_{\omega,x_s}\chi](\vec{\mathbf{x}}_r) = k^2 \int_{-b/2}^{b/2} d\xi\, \widehat{\mathcal{G}}_o(\vec{\mathbf{x}}_r, \vec{\mathbf{y}}, \omega)\widehat{\mathcal{G}}_o(\vec{\mathbf{x}}_s, \vec{\mathbf{y}}, \omega), \tag{9.1}$$

where $\vec{\mathbf{y}} = (L, \xi)$ and $\vec{\mathbf{x}}_r = (0, x_r)$, $\vec{\mathbf{x}}_s = (0, x_s)$. We wish to solve the least squares problem: Minimize

$$\int_{-a/2}^{a/2} dx_r \left| [\mathcal{M}_{\omega,x_s}\chi^{LS}](\vec{\mathbf{x}}_r) - \widehat{\Pi}(\vec{\mathbf{x}}_r, \vec{\mathbf{x}}_s, \omega) \right|^2, \tag{9.2}$$

over "reflectivities" $\chi^{LS}(\xi)$.

The normal equations at search points ξ^S are

$$\left[\mathcal{M}_{\omega,x_s}^\star \mathcal{M}_{\omega,x_s}\chi^{LS}\right](\xi^S) = \left[\mathcal{M}_{\omega,x_s}^\star \widehat{\Pi}(\cdot, \vec{\mathbf{x}}_s, \omega)\right](\xi^S), \tag{9.3}$$

where $\mathcal{M}_{\omega,x_s}^\star$ is the adjoint of $\mathcal{M}_{\omega,x_s}$, defined formally by

$$\begin{aligned}
\left\langle \mathcal{M}_{\omega,x_s}\vartheta, \widehat{\Pi} \right\rangle &= \int_{-a/2}^{a/2} dx_r\, k^2 \int d\xi\, \vartheta(\xi)\widehat{\mathcal{G}}(\vec{\mathbf{x}}_r, \vec{\mathbf{y}}, \omega)\widehat{\mathcal{G}}_o(\vec{\mathbf{x}}_s, \vec{\mathbf{y}}, \omega)\overline{\widehat{\Pi}(\vec{\mathbf{x}}_r, \vec{\mathbf{x}}_s, \omega)} \\
&= \int d\xi\, \vartheta(\xi) \left[\int_{-a/2}^{a/2} dx_r\, k^2 \widehat{\mathcal{G}}_o(\vec{\mathbf{x}}_r, \vec{\mathbf{y}}, \omega)\widehat{\mathcal{G}}_o(\vec{\mathbf{x}}_s, \vec{\mathbf{y}}, \omega)\overline{\widehat{\Pi}(\vec{\mathbf{x}}_r, \vec{\mathbf{x}}_s, \omega)} \right] \\
&= \left(\vartheta, \mathcal{M}_{\omega,x_s}^\star \widehat{\Pi}(\cdot, \vec{\mathbf{x}}_s, \omega) \right),
\end{aligned} \tag{9.4}$$

for an arbitrary test function $\vartheta(\xi)$. We have explicitly,

$$\left[\mathcal{M}_{\omega,x_s}^\star \widehat{\Pi}(\cdot, \vec{\mathbf{x}}_s, \omega)\right](\xi^S) = k^2 \int_{-a/2}^{a/2} dx_r\, \overline{\widehat{\mathcal{G}}_o(\vec{\mathbf{x}}_r, \vec{\mathbf{y}}, \omega)\widehat{\mathcal{G}}_o(\vec{\mathbf{x}}_s, \vec{\mathbf{y}}, \omega)}\widehat{\Pi}(\vec{\mathbf{x}}_r, \vec{\mathbf{x}}_s, \omega). \tag{9.5}$$

To solve the normal equations, we use the spectral decomposition of the normal operator.

Lemma 2 *The normal operator $\mathcal{M}_{\omega,x_s}^\star \mathcal{M}_{\omega,x_s}$ has eigenfunctions*

$$U_n(\xi) = \exp\left(\frac{ikx_s\xi}{L}\right) \psi_n\left(\frac{2\xi}{b}; C(\omega)\right) \tag{9.6}$$

and eigenvalues

$$\mu_n(\omega) = \frac{k}{32\pi L}\nu_n(C(\omega)), \quad n = 0, 1, \ldots. \tag{9.7}$$

The eigenfunctions satisfy the orthogonality relation

$$\int_{-b/2}^{b/2} d\xi\, \overline{U_n(\xi)}\, U_m(\xi) = \int_{-b/2}^{b/2} d\xi\, \psi_n\left(\frac{2\xi}{b}; C(\omega)\right) \psi_m\left(\frac{2\xi}{b}; C(\omega)\right) = \frac{b}{2}\nu_n(C(\omega))\, \delta_{nm}. \tag{9.8}$$

The proof is given at the end of the section. Let us first use this lemma to solve (9.3).

Since the eigenvalues $\mu_n(\omega)$ are negligible for $n > n^\star(\omega)$, the normal operator $\mathcal{M}^\star_{\omega,x_s}\mathcal{M}_{\omega,x_s}$ is singular, with a null space $\mathcal{N} = \text{span}\{U_n(\xi)\}_{n>n^\star(\omega)}$. Thus, the normal equations (9.3) have infinitely many solutions and we seek the one with minimal L^2 norm in the form

$$\chi^{LS}_{\omega,x_s}(\xi^S) = \sum_{n=0}^{n^\star(\omega)} \widehat{d}_n(\omega; x_s) U_n(\xi^S). \tag{9.9}$$

Here we emphasize the dependence of the solution on the frequency and the source location with indices. We substitute (9.9) in (9.3) and get

$$\widehat{d}_n(\omega; x_s) = \frac{64\pi L}{kb\nu_n^2(C(\omega))} \left(U_n, \mathcal{M}^\star_{\omega,x_s}\widehat{\Pi}(\cdot, x_s, \omega) \right), \tag{9.10}$$

using the orthogonality relation (9.8). The inner product $\left(U_n, \mathcal{M}^\star_{\omega,x_s}\widehat{\Pi}(\cdot, x_s, \omega) \right)$ is given by:

Lemma 3 *Let $n \geq 0$ be an arbitrary index. We have*

$$\begin{aligned}
\left(U_n, \mathcal{M}^\star_{\omega,x_s}\widehat{\Pi} \right) &= \int_{-b/2}^{b/2} d\xi^S \overline{U_n(\xi^S)} \left[\mathcal{M}^\star_{\omega,x_s}\widehat{\Pi}(\cdot, x_s, \omega) \right](\xi^S) \\
&\approx \frac{(-1)^n}{8a} \gamma_n(C(\omega)) \, \nu_n(C(\omega)) \, \psi_n\left(\frac{2x_s}{a}; C(\omega) \right).
\end{aligned} \tag{9.11}$$

With this lemma and equation (9.10), we obtain

$$\chi^{LS}_{\omega,x_s}(\xi^S) \approx 2\pi \sum_{n=0}^{n^\star(\omega)} \frac{(-1)^n\gamma_n(C(\omega))}{C(\omega)\nu_n(C(\omega))} \exp\left(\frac{ikx_s\xi^S}{L} \right) \psi_n\left(\frac{2x_s}{a}; C(\omega) \right) \psi_n\left(\frac{2\xi^S}{b}; C(\omega) \right). \tag{9.12}$$

This is the least squares image with a single source at x_s and with a single frequency ω. The result is shown in Figure 16, for the central source location $x_s = 0$ and two frequencies, corresponding to $C(\omega) = 10\pi$ and 100π. We plot in blue $\chi^{LS}_{\omega,x_s}(\xi^S)$ normalized by its maximum. We also show in red the Kirchhoff migration images for the same single source and frequency. Note that these images are almost the same as $\chi^{LS}_{\omega,x_s}(\xi^S)$ for the sources near the center of the array, but the discrepancy increases for sources at the ends of the array. In particular, we get a better focusing of the least squares image at the ends of the strip.

If we use all the sources, we can superpose the estimates (9.12) to get a better result

$$\chi^{LS}_\omega(\xi^S) \approx \frac{1}{a} \int_{-a/2}^{a/2} dx_s \, \chi^{LS}_{\omega,x_s}(\xi^S) = \frac{\pi}{C(\omega)} \sum_{n=0}^{n^\star(\omega)} \psi_n^2\left(\frac{2\xi^S}{b}; C(\omega) \right). \tag{9.13}$$

Here we used Property 4 of the prolate spheroidal wave functions. We plot $\chi^{LS}_\omega(\xi^S)$ in Figure 17, with the blue line, for $C(\omega) = 10\pi$ and 100π. We note that it is close to the true reflectivity $\chi(\xi^S)$, the indicator function of the interval $[-b/2, b/2]$. This follows from Lemma 4. We also show in

49
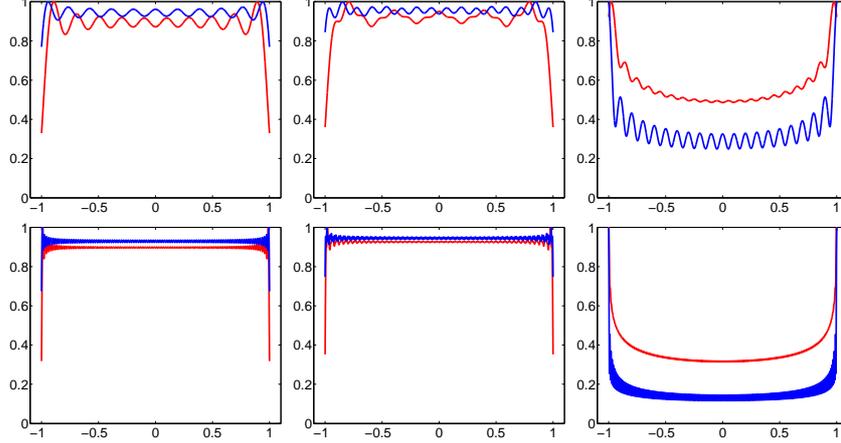
Figure 16: In blue, the linearized least squares solution for a single source at x_s and frequency ω. In red, the Kirchhoff migration image for a single source at x_s and frequency ω. Top: $C(\omega) = 10\pi$. Bottom: $C(\omega) = 100\pi$. Left: $x_s = 0$, middle: $x_s = a/4$ and right: $x_s = a/2$. The abscissa is $2\xi^S/b$. We plot the absolute value of the image normalized by its maximum.
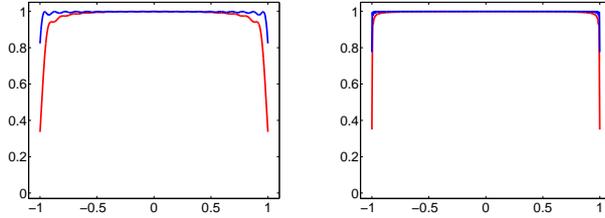
Figure 17: In blue, the linearized least squares solution (9.13) with all the sources in the array and a fixed frequency. In red, the Kirchhoff migration image (9.14) for uniform illumination. The range is assumed known and we take a fixed frequency. Left: $C(\omega) = 10\pi$. Right: $C(\omega) = 100\pi$. The abscissa is $2\xi^S/b$.

Figure 17, in red, the Kirchhoff migration image given by $\widehat{f}(\vec{\mathbf{x}}_s, \omega) = 1$, at fixed frequency and known range. Straightforward calculations give

$$\mathcal{I}^{\mathrm{KM}}\left((L, \xi^S); \widehat{f} = 1\right) \sim \sum_{n=0}^{n^\star(\omega)} \nu_n^2(C(\omega))\, \psi_n^2\!\left(\frac{2\xi^S}{b}; C(\omega)\right). \tag{9.14}$$

We note that by inverting the normal operator we improve a little the reconstruction at the edges of the strip. This is more visible at the lower frequencies. At the high frequencies, the images are basically the same.

Lemma 4 *The prolate spheroidal wave functions satisfy the identity*

$$\frac{\pi}{C(\omega)} \sum_{n=0}^{\infty} \nu_n(C(\omega))\, \psi_n^2(\zeta; C(\omega)) = \begin{cases} 1 & \text{if } |\zeta| \leq 1, \\ 0 & \text{otherwise.} \end{cases} \tag{9.15}$$

50

Since $\nu_n(C(\omega)) \approx 1$ for $n < n^\star(\omega)$ and 0 for $n > n^\star(\omega)$, we have

$$
\chi(\xi^S) \approx \chi_\omega^{LS}(\xi^S) = \frac{\pi}{C(\omega)} \sum_{n=0}^{n^\star(\omega)} \psi_n^2 \left(\frac{2\xi^S}{b}; C(\omega) \right)
$$

$$
\approx \frac{\pi}{C(\omega)} \sum_{n=0}^{n^\star(\omega)} \nu_n^2(C(\omega)) \, \psi_n^2 \left(\frac{2\xi^S}{b}; C(\omega) \right) \sim \mathcal{I}^{KM} \left((L, \xi^S); \widehat{f} = 1 \right). \tag{9.16}
$$

Proof: From the spectral representation (8.32) of the kernel and letting $\zeta' \to \zeta$ in (8.32), we get

$$
\frac{C(\omega)}{\pi} = \sum_{n=0}^{\infty} \nu_n(C(\omega)) \, \psi_n^2(\zeta; C(\omega)). \tag{9.17}
$$

The rest of the lemma follows from Property 3. □

9.1 Proofs of Lemmas 2 and 3

Proof of Lemma 2: We already know from section 7 that the prolate spheroidal wave functions are concentrated in $[-b/2, b/2]$ for indices below the threshold. The orthogonality relation (9.8) follows from Property 1. Thus, the only thing left to prove is that U_n are eigenfunctions of the normal operator. Write using the definition (9.5) of the adjoint $\mathcal{M}_{\omega, x_s}^\star$ that

$$
\left[\mathcal{M}_{\omega, x_s}^\star \mathcal{M}_{\omega, x_s} U_n \right] (\xi^S) = k^2 \int_{-a/2}^{a/2} dx_r \, \overline{\widehat{\mathcal{G}}_o(\vec{\mathbf{x}}_r, \vec{\mathbf{y}}^S, \omega)} \widehat{\mathcal{G}}_o(\vec{\mathbf{x}}_s, \vec{\mathbf{y}}^S, \omega) \left[\mathcal{M}_{\omega, x_s} U_n \right] (x_r), \tag{9.18}
$$

where $\vec{\mathbf{y}}^S = (L, \xi^S)$ is the search point. Use also the definition (9.1) of $\mathcal{M}_{\omega, x_s}$ to get

$$
\left[\mathcal{M}_{\omega, x_s}^\star \mathcal{M}_{\omega, x_s} U_n \right] (\xi^S) = k^4 \int_{-a/2}^{a/2} dx_r \, \overline{\widehat{\mathcal{G}}_o(\vec{\mathbf{x}}_r, \vec{\mathbf{y}}^S, \omega)} \widehat{\mathcal{G}}_o(\vec{\mathbf{x}}_s, \vec{\mathbf{y}}^S, \omega)
$$

$$
\int_{-b/2}^{b/2} d\xi \, U_n(\xi) \, \widehat{\mathcal{G}}_o(\vec{\mathbf{x}}_r, \vec{\mathbf{y}}, \omega) \overline{\widehat{\mathcal{G}}_o(\vec{\mathbf{x}}_s, \vec{\mathbf{y}}, \omega)}, \tag{9.19}
$$

for points $\vec{\mathbf{y}} = (L, \xi)$. Now the Green's function is given by (5.13) and so (9.19) becomes

$$
\left[\mathcal{M}_{\omega, x_s}^\star \mathcal{M}_{\omega, x_s} U_n \right] (\xi^S) = k^2 |\alpha(L)|^4 \exp\left(\frac{ikx_s \xi^S}{L} \right) \int_{-b/2}^{b/2} d\xi \, \psi_n \left(\frac{2\xi}{b}; C(\omega) \right)
$$

$$
\int_{-a/2}^{a/2} dx_r \, \exp\left(\frac{ikx_r(\xi^S - \xi)}{L} \right). \tag{9.20}
$$

Finally, we integrate over x_r and use definitions (5.12) and (7.7) to get

$$
\left[\mathcal{M}_{\omega, x_s}^\star \mathcal{M}_{\omega, x_s} U_n \right] (\xi^S) = 2\pi L k |\alpha(L)|^4 \exp\left(\frac{ikx_s \xi^S}{L} \right) \int_{-b/2}^{b/2} d\xi \frac{\sin\left[C(\omega) \frac{2(\xi^S - \xi)}{b} \right]}{\pi(\xi^S - \xi)} \psi_n \left(\frac{2\xi}{b}; C(\omega) \right)
$$

$$
= \frac{k}{32\pi L} \nu_n(C(\omega)) \, U_n(\xi^S). \quad \square \tag{9.21}
$$

51

Proof of Lemma 3: Using definition (9.5) of the adjoint operator and (9.6), we have

$$\int_{-b/2}^{b/2} d\xi^S \overline{U_n(\xi^S)} \left[\mathcal{M}_{\omega,x_s}^\star \widehat{\Pi}(\cdot, \vec{\mathbf{x}}_s, \omega) \right](\xi^S) = k^2 \overline{\widehat{\mathcal{G}}_o(\vec{\mathbf{x}}_s, \vec{\mathbf{y}}^\star, \omega)} \int_{-a/2}^{a/2} dx_r \, \widehat{\Pi}(\vec{\mathbf{x}}_r, \vec{\mathbf{x}}_s, \omega) \overline{\widehat{\mathcal{G}}_o(\vec{\mathbf{x}}_r, \vec{\mathbf{y}}^\star, \omega)}$$

$$\int_{-b/2}^{b/2} d\xi^S \psi_n\left(\frac{2\xi^S}{b}; C(\omega) \right) \exp\left(\frac{ik x_r \xi^S}{L} \right),$$

where

$$\int_{-b/2}^{b/2} d\xi^S \psi_n\left(\frac{2\xi^S}{b}; C(\omega) \right) \exp\left(\frac{ik x_r \xi^S}{L} \right) = \frac{\pi b \gamma_n(C(\omega))}{C(\omega)} \psi_n\left(\frac{2x_r}{a}; C(\omega) \right), \tag{9.22}$$

by identity (7.25). We obtain

$$\int_{-b/2}^{b/2} d\xi^S \, \overline{U_n(\xi^S)} \left[\mathcal{M}_{\omega,x_s}^\star \widehat{\Pi}(\cdot, \vec{\mathbf{x}}_s, \omega) \right](\xi^S) = \frac{\pi b k^2 \gamma_n(C(\omega))}{C(\omega)} \overline{\widehat{\mathcal{G}}_o(\vec{\mathbf{x}}_s, \vec{\mathbf{y}}^\star, \omega)}$$

$$\int_{-a/2}^{a/2} dx_r \, \widehat{\Pi}(x_r, x_s, \omega) \overline{\widehat{\mathcal{G}}_o(\vec{\mathbf{x}}_r, \vec{\mathbf{y}}^\star, \omega)} \psi_n\left(\frac{2x_r}{a}; C(\omega) \right). \tag{9.23}$$

Now, the Born approximation (9.1) of the data gives

$$\int_{-a/2}^{a/2} dx_r \, \widehat{\Pi}(\vec{\mathbf{x}}_r, \vec{\mathbf{x}}_s, \omega) \overline{\widehat{\mathcal{G}}_o(\vec{\mathbf{x}}_r, \vec{\mathbf{y}}^\star, \omega)} \psi_n\left(\frac{2x_r}{a}; C(\omega) \right) \approx k^2 \int_{-b/2}^{b/2} d\xi \int_{-a/2}^{a/2} dx_r \, \widehat{\mathcal{G}}_o(\vec{\mathbf{x}}_s, \vec{\mathbf{y}}, \omega)$$

$$\widehat{\mathcal{G}}_o(\vec{\mathbf{x}}_r, \vec{\mathbf{y}}, \omega) \overline{\widehat{\mathcal{G}}_o(\vec{\mathbf{x}}_r, \vec{\mathbf{y}}^\star, \omega)} \psi_n\left(\frac{2x_r}{a}; C(\omega) \right) \tag{9.24}$$

and, with definition (5.13) of the Green's function, we get

$$\int_{-a/2}^{a/2} dx_r \, \widehat{\Pi}(\vec{\mathbf{x}}_r, \vec{\mathbf{x}}_s, \omega) \overline{\widehat{\mathcal{G}}_o(\vec{\mathbf{x}}_r, \vec{\mathbf{y}}^\star, \omega)} \psi_n\left(\frac{2x_r}{a}; C(\omega) \right) \approx k |\alpha(L)|^2 \widehat{\mathcal{G}}_o(\vec{\mathbf{x}}_s, \vec{\mathbf{y}}^\star, \omega)$$

$$\int_{-b/2}^{b/2} d\xi \exp\left(-\frac{ik x_s \xi}{L} \right) \int_{-a/2}^{a/2} dx_r \psi_n\left(\frac{2x_r}{a}; C(\omega) \right) \exp\left(-\frac{ik x_r \xi}{L} \right). \tag{9.25}$$

The integral over x_r is similar to (9.22),

$$\int_{-a/2}^{a/2} dx_r \psi_n\left(\frac{2x_r}{a}; C(\omega) \right) \exp\left(-\frac{ik x_r \xi}{L} \right) = \frac{\pi a \overline{\gamma_n(C(\omega))}}{C(\omega)} \psi_n\left(\frac{2\xi}{b}; C(\omega) \right), \tag{9.26}$$

and so

$$\int_{-b/2}^{b/2} d\xi \exp\left(-\frac{ik x_s \xi}{L} \right) \int_{-a/2}^{a/2} dx_r \psi_n\left(\frac{2x_r}{a}; C(\omega) \right) \exp\left(-\frac{ik x_r \xi}{L} \right) = \frac{\pi a \overline{\gamma_n(C(\omega))}}{C(\omega)}$$

$$\int_{-b/2}^{b/2} d\xi \, \psi_n\left(\frac{2\xi}{b}; C(\omega) \right) \exp\left(-\frac{ik x_s \xi}{L} \right) = \frac{\pi^2 ab \overline{\gamma_n^2(C(\omega))}}{C^2(\omega)} \psi_n\left(\frac{2x_s}{a}; C(\omega) \right). \tag{9.27}$$

Equation (9.24) becomes

$$\int_{-a/2}^{a/2} dx_r \, \widehat{\Pi}(\vec{\mathbf{x}}_r, \vec{\mathbf{x}}_s, \omega) \overline{\widehat{\mathcal{G}}_o(\vec{\mathbf{x}}_r, \vec{\mathbf{y}}^\star, \omega)} \psi_n\left(\frac{2x_r}{a}; C(\omega)\right) \approx 2\pi L |\alpha(L)|^2 \widehat{\mathcal{G}}_o(\vec{\mathbf{x}}_r, \vec{\mathbf{y}}^\star, \omega)$$

$$(-1)^n \nu_n(C(\omega)) \, \psi_n\left(\frac{2x_s}{a}; C(\omega)\right), \qquad (9.28)$$

and using it in (9.23) we obtain

$$\int_{-b/2}^{b/2} d\xi^S \, \overline{U_n(\xi^S)} \left[\mathcal{M}_{\omega,x_s}^\star \widehat{\Pi}(\cdot, x_s, \omega)\right](\xi^S) = \frac{(-1)^n}{8a} \gamma_n(C(\omega)) \, \nu_n(C(\omega)) \, \psi_n\left(\frac{2x_s}{a}; C(\omega)\right), \qquad (9.29)$$

as stated in Lemma 3 □.

10 Summary

We have introduced new variational algorithms for optimal illumination and selective array imaging. Although we considered here imaging in homogeneous media, in high SNR regimes, the algorithms have been extended to imaging in clutter in [11]. Low SNR due to noise at the receivers is taken into account in [9], using lower bound constraints on the power of the received echoes.

We showed with numerical simulations and with analysis in the Fraunhofer diffraction regime that both time reversal and Kirchhoff migration images can improve significantly with optimal illumination. We found that, at high SNR, the optimal illuminations favor the edges of the array and the high end of the frequency band. These illuminations give the sharpest images of small scatterers and they emphasize the edges of extended scatterers.

We also introduced variational, selective subspace array imaging algorithms, based on the SVD of the array response matrix in the frequency domain. We illustrated with numerical simulations how the algorithms image selectively clusters of small scatterers.

We obtained analytical forms of the SVD of the array response matrix in the Fraunhofer diffraction regime and used them to analyze the optimal illumination and selective imaging problems for time reversal and Kirchhoff migration imaging of extended scatterers. In the case of strip-like scatterers, we derived an explicit form of the SVD using the prolate spheroidal wave functions. We proved in the process that the rank of the response matrix in the frequency domain is given by the ratio of the strip length and the time reversal spot size.

Using the explicit form of the SVD for strip scatterers we obtained a detailed description of optimal waveform design for time reversal and Kirchhoff migration imaging. In particular, we showed how the variational algorithms mask the strong specular reflections from the bulk of the scatterer and emphasize its edges.

Finally, we studied full linearized least squares imaging for strip scatterers. Kirchhoff migration is expected to be an approximation of the least squares method, where the normal operator is

replaced by the identity. We computed explicitly the normal operator and its pseudo-inverse for the strip and obtained a quantitative comparison between least squares and Kirchhoff migration.

Acknowledgments

References

[1] E. Bécache, P. Joly, and C. Tsogka. Etude d'un nouvel élément fini mixte permettant la condensation de masse. *C. R. Acad. Sci. Paris Sér. I Math.*, 324:1281–1286, 1997.

[2] E. Bécache, P. Joly, and C. Tsogka. An analysis of new mixed finite elements for the approximation of wave propagation problems. *SIAM J. Numer. Anal.*, 37:1053–1084, 2000.

[3] J.P. Bérenger. A perfectly matched layer for the absorption of electromagnetic waves. *Journal of Comp. Physics.*, 114:185–200, 1994.

[4] G. Beylkin. Imaging of discontinuities in the inverse scattering problem by inversion of a causal generalized Radon transform. *J. Math. Phys.*, 26(1):99–108, 1985.

[5] N. Bleistein, J.K. Cohen, and J.W. Stockwell Jr. *Mathematics of multidimensional seismic imaging, migration, and inversion.* Springer, New York, 2001.

[6] P. Blomgren, G. Papanicolaou, and H. Zhao. Super-resolution in time-reversal acoustics. *Journal of the Acoustical Society of America*, 111:238–248, 2002.

[7] L. Borcea, G. Papanicolaou, and C. Tsogka. Theory and applications of time reversal and interferometric imaging. *Inverse Problems*, 19:S134–164, 2003.

[8] L. Borcea, G. Papanicolaou, and C. Tsogka. Interferometric array imaging in clutter. *Inverse Problems*, 21(4):1419–1460, 2005.

[9] L. Borcea, G. Papanicolaou, and C. Tsogka. Adaptive interferometric imaging in clutter and optimal illumination. *Inverse Problems*, 22(4):1405–1436, 2006.

[10] L. Borcea, G. Papanicolaou, and C. Tsogka. Asymptotics for the space-time Wigner transform with applications to imaging. *Stochastic Differential Equations: Theory and Applications. Volume in Honor of Professor Boris L Rozovskii, P. H. Baxendale and S. V. Lototsky editors.*, Interdisciplinary Mathematical Sciences, vol. 2, 2007.

[11] L. Borcea, G. Papanicolaou, and C. Tsogka. Optimal illumination and waveform design for imaging in random media. Submitted to JASA. Available at http://georgep.stanford.edu/ papanico/pubs.html, 2007.

[12] L. Borcea, G. Papanicolaou, C. Tsogka, and J. Berryman. Imaging and time reversal in random media. *Inverse Problems*, 18:1247–1279, 2002.

[13] L. Borcea, G. Papanicolaou, C. Tsogka, and J. Berryman. Statistically stable ultrasonic imaging in random media. *J. Acoust. Soc. Am.*, 112:1509–1522, 2002.

[14] M. Born and E. Wolf. *Principles of optics.* Academic Press, New York, 1970.

[15] M. Cheney, D. Isaacson, and M. Lassas. Optimal acoustic measurements. *SIAM J. Appl. Math.*, 61(5):1628–1647, 2001.

[16] J. F. Claerbout and S. M. Doherty. Downward continuation of moveout-corrected seismograms. *Geophysics*, 37(5):741–768, 1972.

[17] R. Courant and D. Hilbert. *Methods of Mathematical Physics*, volume 1. Wiley Classic Library, New York, 1953.

[18] M. Fink. Time reversal mirrors. *J. Phys. D*, 26:1330–1350, 1993.

[19] S. Hou, K. Solna, and H. Zhao. A direct imaging algorithm for extended targets. *Inverse Problem*, 22:1151–1178, 2006.

[20] S. Komilikis, C. Prada, and M. Fink. Characterization of extended objects withe DORT method. *IEEE Ultrasonics Symposium*, pages 1401–1404, 1996.

[21] H. J. Landau and H. O. Pollak. Prolate spheroidal wave functions, Fourier analysis and uncertainty, II. *Bell Systems Tech. J.*, 40:65–84, 1961.

[22] G. Montaldo, M. Tanter, and M. Fink. Revisting iterative time reversal processing: Application to detection of multiple targets. *J. Acoust. Soc. Am.*, 115(2):776–784, 2004.

[23] C. Prada and M. Fink. Eigenmodes of the time reversal operator: A solution to selective focusing in multiple-target media. *Wave Motion*, 20:151–163, 1994.

[24] C. Prada, J. L. Thomas, and M. Fink. The iterative time-reversal process: analysis of the convergence. *J. Acoust. Soc. Am.*, 97:62–71, 1995.

[25] D. Slepian. Some comments on Fourier analysis, uncertainty and modeling. *SIAM Review*, 25(3):379–393, 1983.

[26] D. Slepian and H. O. Pollak. Prolate spheroidal wave functions, Fourier analysis and uncertainty, I. *Bell Systems Tech. J.*, 40:43–64, 1961.

[27] W. Symes. Lecture notes in seismic imaging. Mathematical Geophysics Summer School, Stanford, available at www.trip.caam.rice.edu, 1998.

[28] M. Tanter, J. F. Aubry, J. Gerber, J. L. Thomas, and M. Fink. Optimal focusing by spatio-temporal inverse filter. I. Basic principles. *J. Acoust. Soc. Am.*, 110(1):37–47, 2001.

[29] M. Tanter, J. L. Thomas, and M. Fink. Time reversal and the inverse filter. *J. Acoust. Soc. Am.*, 108(1):223–234, 2000.